

STRUCTURE AND RHEOLOGY OF MACROMOLECULAR SYSTEMS AT INTERFACES

A THESIS

submitted by

ANTIGONI THEODORATOU

for the award of the degree

of

DOCTOR OF PHILOSOPHY



**DEPARTMENT OF MATERIAL SCIENCE AND TECHNOLOGY
UNIVERSITY OF CRETE**

SEPTEMBER 2015

THESIS CERTIFICATE

This is to certify that the thesis titled **STRUCTURE AND RHEOLOGY OF MACROMOLECULAR SYSTEMS AT INTERFACES**, submitted by **Antigoni Theodoratou**, to the department of Material Science and Technology of University of Crete, for the award of the degree of **Doctor of Philosophy**, is a bona fide record of the research work done by her under our supervision. The contents of this thesis, in full or in parts, have not been submitted to any other Institute or University for the award of any degree or diploma.

Committee:

Prof. George Fytas

Prof. Jeffrey Giacomini

Prof. Moshe Gottlieb

Prof. Ulrich Jonas

Dr. Benoit Loppinet

Prof. Maria Vamvakaki

Prof. Dimitris Vlassopoulos (supervisor)

Place: Heraklion

Date: 11th September 2015

ACKNOWLEDGEMENTS

I would like to express my gratitude to my supervisor Dimitris Vlassopoulos for his guidance and support during my PhD studies and for giving me the opportunity to travel and attend schools, conferences and perform experiments in many renowned laboratories all around Europe. I feel sincerely grateful to him especially for having expressed his full confidence in me and for having allowed me to work with independence. Also I would like to express my deep appreciation and respect to my co-supervisor, Ulrich Jonas, I am thankful to him because of the great help with the neutron reflectivity experiments in Paul Scherrer Institute, his tremendous patience with me and his systematic guidance especially with our project of the photo-responsive SFAs. Also, I would like to acknowledge appreciation to Benoit Loppinet for his brilliant ideas while I was facing problems with the Langmuir trough experiments, the magnetic rod ISR and the neutron reflectivity experiments.

I would like to thank Prof. Jan Vermant for the hospitality in K.U. Leuven and E.T.H., and his students Tom Verwijlen and Eline Hermans for the nice discussions and tips about interfacial rheology. My thanks to Thomas Geue for his hospitality (3 times) at Paul Scherrer Institute in Zurich and help for the neutron reflectivity experiments. Also, I would like to thank the group of Prof. Klaus Müllen and Dr. Rüdiger Berger for the synthesis of the materials and the AFM experiments, respectively. I would like to thank Prof. Moshe Gottlieb for the collaboration concerning the PEO-PDMS project at the air-water and oil-water interface and his student Mor Armon who performed most of the surface/pressure area isotherms in FORTH. Also, many thanks to Rossana Pasquino for the help with the extraction of dynamic moduli from the creep data. Also, I would like to thank Patrick Ruehs from the group of Prof. Pieter Fisher in E.T.H. for having performed the DSS experiments of PMMA layers with the bi-conical device. Many thanks to Christopher Klein for the help about the technical problems I was facing often with the ISR and the helpful discussions about FT rheology. I would like to thank all the members of the committee for the helpful comments that surely contributed to the development and the improvement of my thesis and, more in general, to my level of

understanding.

I would also like to thank my laboratory colleagues of the polymer group at FORTH with who I shared most of the time here in Crete throughout the years and for their support and friendship. Especially, I need to express my deep and thankful appreciation to Alan Jacob for teaching me LATEX and for his great help, support and friendship during the last years. Also, I would like to express my special acknowledgment to Domenico Truzzolillo for the training in interfacial rheology and his psychological support during the last years. I want to thank my best friend, Maria Kaliva for the help with the synthesis of my grafted needles, but especially for her support and encouragement during the difficult periods of the last four years, without her I could not have survived. Last, but certainly not least, huge thanks and gratitude to my family, Rena, Artemis, Stavros and Artemisia for their support and love over the years.

Acknowledgment of financial support:

- Heraclitos II program (Greek General Secretariat for Research and Technology (NSRF 2007-2013))
- Thales program (NSRF 2007-2013)
- EU (FP7 Infrastructure ESMI GA-262348)



ABSTRACT

KEYWORDS: interfacial rheology; magnetic rod interfacial stress rheometer; double wall ring; semifluorinated alkanes; air-water interface, neutron reflectivity, interfacial structure.

This thesis focuses on the structural and rheological properties of viscoelastic films at the air-water interface. Our aim is to tailor the rheological properties of fluid interfaces and link them with their structure at the molecular scale. Langmuir quasi-monolayers were built by employing three different types of molecular systems, a series of semifluorinated alkanes that consist of two hydrophobic segments, a homopolymer, Poly(methyl methacrylate) (PMMA), and block copolymers of PEO-PDMS with different molecular architectures. The techniques employed in this thesis include Langmuir-Pockels trough, to measure surface pressure/ area isotherms, and the magnetic rod interfacial stress rheometer, double wall ring fixture and bi-conical device in commercial rheometers for interfacial rheology studies. For structural studies of the films at the air-water interface we performed neutron reflectivity measurements and scanning force microscopy.

We observed great tunability of the structural and rheological properties of the semifluorinated alkanes moving from simple linear molecules to more complex and branched architectures, showing that molecular modification can change dramatically the viscoelastic response of the layers. Regardless of the molecular architecture effect, the external light stimulus effect was investigated for photo-sensitive semifluorinated alkanes that could change their conformation reversibly from trans to cis. One of the main findings of this study was the transition from ordered to mixed (disordered) structures whose onset is signaled by the drop of the interfacial storage modulus of about one order of magnitude.

The predominantly elastic layers of PMMA were used to investigate the presence of even harmonics among different rheometry techniques. By analysing the strain signal in the Fourier space, it was found that the bi-conical and the double wall ring fixture

do not generate even harmonics while the magnetic rod showed the presence of 2^{nd} harmonics that are connected with asymmetry in the stress-strain profile, apparently stemming from ununiformity in flow and the subphase contribution.

Finally, the diblock and triblock copolymers of PEO-PDMS exhibit perfectly reversible layers at the air-water interface showing a reproducible PDMS phase transition for all the different molecular weights. Moreover, the average Flory radius of the polymers scale as $R_F \sim N^\nu$, with $\nu=0.56 \pm 0.01$. Such result are in agreement with predicted scaling for 2D-polymers in bad solvent conditions.

TABLE OF CONTENTS

ACKNOWLEDGEMENTS	i
ABSTRACT	iii
LIST OF FIGURES	xvi
1 INTRODUCTION	1
2 MATERIALS AND METHODS	5
2.1 The technique of "Langmuir Trough"	5
2.2 Interfacial Rheometry Techniques	7
2.2.1 Magnetic Rod Interfacial Stress Rheometer (ISR)	7
2.2.2 Double Wall Ring	13
2.2.3 Bi-conal Fixture	14
2.3 Neutron Reflectivity	15
2.4 Scanning force microscopy	16
2.5 Materials	17
3 SEMIFLUORINATED ALKANES AT THE WATER-AIR INTERFACE: EFFECTS OF MOLECULAR ARCHITECTURE ON STRUCTURE AND RHEOLOGY	24
3.1 State of the art	24
3.2 Perfluoro(dodecyl)dodecane (F12H12) and bis(3-(1- perfluoroundecyl- methoxy) -5-dodecyloxyphenyl)ethyne (bis(F11H1-core-H12)) . . .	28
3.2.1 Surface Pressure Area Isotherms	28
3.2.2 Interfacial Rheology	30
3.2.3 Neutron Reflectivity	34
3.2.4 Scanning Force Microscopy	37
3.3 1-Dodecyl-4-(perfluorododecyl)benzol (F12-phenyl-H12) and 1-(Dodecyloxy)- 4-((perfluorododecyl)oxy)benzol (F12-O-phenyl-O-H12)	38
3.3.1 Surface Pressure Area Isotherms	38

3.3.2	Interfacial Rheology	40
3.3.3	Neutron Reflectivity	43
3.3.4	Scanning Force Microscopy	44
3.4	Didodecyl-2,7-bis(perfluorododecyl)-9H-fluoren (2F12-core-2H12) and 9,9-Didodecyl-9H-fluoren (2H-core-2H12)	46
3.4.1	Surface Pressure Area Isotherms	46
3.4.2	Interfacial Rheology	48
3.4.3	Neutron Reflectivity	50
3.4.4	Scanning Force Microscopy	53
3.5	Concluding remarks	54
4	RESPONSIVE FLUID INTERFACES: PROPERTIES OF PHOTO-SENSITIVE FILMS OF SEMIFLUORINATED ALKYL-AZOBENZENES AT THE WATER-AIR INTERFACE	56
4.1	State of the art	56
4.2	Surface Pressure Area Isotherms	60
4.3	Interfacial Rheology	63
4.4	Neutron Reflectivity	66
4.5	Concluding Remarks	70
5	FOURIER TRANSFORM RHEOLOGY OF PMMA INTERFACES	72
5.1	State of the art	72
5.2	Results and discussion	76
5.2.1	Surface pressure/area isotherms	76
5.2.2	Nonlinear-FT analysis procedure	78
5.2.3	Magnetic rod interfacial stress rheometer: The effect of channel size	79
5.2.4	Magnetic rod interfacial stress rheometer using a PMMA-grafted glassy needle	86
5.2.5	Magnetic rod interfacial stress rheometer using a PMMA-grafted channel	90
5.2.6	Bi-conical fixture	94
5.2.7	Double wall ring fixture	96
5.3	Concluding remarks	99
6	BLOCK COPOLYMERS AT THE WATER-AIR INTERFACE	101

6.1	State of the art	101
6.2	Surface Pressure Area Isotherms	104
6.3	Interfacial Rheology	109
6.4	Concluding remarks	111
7	CONCLUSIONS AND PERSPECTIVES	113
A	NEEDLE CHARACTERIZATION	117
B	MINI TROUGH:WATER-OIL INTERFACE	120
C	NON-CONVERGENT MODELS IN NEUTRON REFLECTIVITY	123
D	Fourier Transform magnitude spectra	125

LIST OF FIGURES

2.1	a) Langmuir films and b) Gibbs films.	5
2.2	KSV NIMA Langmuir-Blodgett Trough. This image is taken from the official webpage of KSV Instruments (www.biolinscientific.com/ksvnima/products/).	6
2.3	A generalized isotherm curve of Langmuir monolayer. The image is taken from Kaganer <i>et al.</i> (1999).	7
2.4	Schematic representation of the magnetic rod interfacial stress rheometer. This image has been taken from Brooks <i>et al.</i> (1999).	8
2.5	Sketch of the wiring diagram for the interafcial stress rheometer. . .	9
2.6	The flow cell with the magnetic needle.	10
2.7	Sinusoidal signals of the applied force and the displacement taken from the magnetic rod ISR.	10
2.8	(a) Amplitude ratio and (b) phase angle as a function of forcing frequency for a monolayer-free interface.	11
2.9	Right: A DWR and Left: Cross section of the DWR set up. This image is taken from Vandebril <i>et al.</i> (2010).	13
2.10	Schematic of the rotational bi-conical rheometer.	14
2.11	Sketch of the overall instrumental layout of the PSI reflectometer. .	15
2.12	Transferring procedure of the layers onto silicon wafers. This image has been taken from Vogel <i>et al.</i> (2011)	17
2.13	Perfluoro(dodecyl)dodecane (F12H12). The cartoon illustration is taken from Clark <i>et al.</i> (2009).	19
2.14	Biphasic DPA, bis(3-(1-perfluoroundecylmethoxy)-5-dodecyloxyphenyl)ethyne (bis(F11H1-core-H12). The cartoon illustration is taken from Clark <i>et al.</i> (2009).	20
2.15	1-Dodecyl-4-(perfluorododecyl)benzol (F12-phenyl-H12). This cartoon illustration has been taken from Stangenberg (2013).	20
2.16	1-(Dodecyloxy)-4-((perfluorododecyl)oxy)benzol (F12-O-phenyl-O-H12). This cartoon illustration has been taken from Stangenberg (2013). .	20
2.17	Didodecyl-2,7-bis(perfluorododecyl)-9H-fluoren (2F12-core-H12). This cartoon illustration has been taken from Stangenberg (2013).	21
2.18	9,9-Didodecyl-9H-fluoren (2H-core-2H12). This cartoon illustration has been taken from Stangenberg (2013).	21

2.19	Azobenzene derivatives (E)-1-(4-octylphenyl)- 2-(4-(perfluorooctyl)phenyl) diazene (F8-azo-H8) and (E)-1,2-bis(4-octylphenyl)diazene (H8-azo-H8). This cartoon illustration has been taken from Stangenberg (2013).	21
2.20	Diblocks of Polyethyleneoxide (PEO)- Polydimethylsiloxane (PDMS).	22
2.21	Poly(methyl methacrylate) (PMMA).	23
3.1	Linear F_nH_m diblocks are (a) Amphisteric, (b) Amphiphilic, and (c) Amphidynamic. The image has been taken from Krafft and Riess (2009).	25
3.2	Model proposed for the hierarchical formation of the surface micelles. (A) Self-assembly of the amphiphobic F12H12 molecules in parallel orientation with the F-block pointing up to the air into curved primary aggregates with ca. 10 nm diameter. (B) Secondary assembly (side view) of the primary aggregates into clusters of the surface micelles driven by capillary forces. (C) Surface micelle aggregation (top view) with slight deformation of the primary aggregates and comparison to the SFM image details. The image has been taken from de Viguerie <i>et al.</i> (2011).	27
3.3	Surface pressure/area isotherms of F12H12 and bis(F11H1-core-H12) monolayers at the water-air interface at 20°C. The arrow shows a change in the packing order of the monolayer.	29
3.4	Compression- expansion cycles of a) F12H12 and b) bis(F11H1-core-H12) at 20°C.	30
3.5	The role of preshear at $\omega=10$ rad/s for 2 min for a) F12H12 and b) bis(F11H1-core-H12) at $\Pi=2$ mNm ⁻¹ . G' (closed symbols) G'' (open symbols).	31
3.6	Nonlinear viscoelasticity of F12H12 at $\omega=0.65$ rad/s. a) Dynamic Strain Sweep measurement at five different surface pressures, 2 mNm ⁻¹ (circles), 4 mNm ⁻¹ (triangles), 6 mNm ⁻¹ (stars), 8 mNm ⁻¹ (diamonds) and 10 mNm ⁻¹ (squares). The red arrow indicates the crossover. b) Interfacial stress as a function of strain. The red arrow indicates the onset of a nonlinear stress-strain relation. G' (closed symbols) and G'' (open symbols).	31
3.7	a) Interfacial frequency sweep data of bis(F11H1-core-H12) at $\gamma=0.1$ % and 20°C. The surface moduli are depicted as functions of frequency at 4 mNm ⁻¹ (circles), 8 mNm ⁻¹ (triangles), 10 mNm ⁻¹ (squares), 20 mNm ⁻¹ (inverted triangles) and 22 mNm ⁻¹ (diamonds) measured on Double Wall Ring (DWR). G' (closed symbols) G'' (open symbols).	32
3.8	Nonlinear viscoelasticity of bis(F11H1-core-H12) at $\omega=0.65$ rad/s. a) Dynamic Strain Sweep measurement at five different surface pressures, 4 mNm ⁻¹ (circles), 8 mNm ⁻¹ (triangles), 10 mNm ⁻¹ (squares), 20 mNm ⁻¹ (inverted triangles) and 22 mNm ⁻¹ (diamonds). b) Interfacial Stress as a function of strain. G' (closed symbols) and G'' (open symbols).	33

3.9	Comparison of storage modulus vs surface pressure of bis(F11H1-core-H12) (square symbols) and F12H12 (stars). The error bars are included in the size of the symbols.	33
3.10	Maximum linear strain amplitude (spherical symbols) and stress (star symbols) versus surface pressure for a) F12H12 and b) bis(F11H1-core-H12).	34
3.11	Neutron reflectivity study of bis(F11H1-core-H12). Neutron Reflectivity curve and Scattering Length Density profile (inset) at air/D ₂ O interface. Surface pressures: 2 mNm ⁻¹ (blue color), 5 mNm ⁻¹ (red color) and 12.8 mNm ⁻¹ (green color). In the figures, the normalized intensity is denoted as I (a.u.).	36
3.12	Neutron Reflectivity curve and Scattering Length Density profile (inset) of bis(F11H1-core-H12) at air/si-wafer interface. Surface pressures: 2 mNm ⁻¹ (blue color) and 5 mNm ⁻¹ (green color) and bare wafer (red color). In the figures, the normalized intensity is denoted as I (a.u.).	37
3.13	Height image (A) and phase image (B) of bis(F11H1-core-H12) transferred at $\Pi=2\text{mN/m}$	37
3.14	SFM topographic image of an F12H12 monolayer transferred at $\Pi=2\text{mN/m}$. (B) Zoom-in of the topographic image. This image has been taken from de Viguerie <i>et al.</i> (2011)	38
3.15	Surface pressure/area isotherms of F12-phenyl-H12 and F12-O-phenyl-O-H12 monolayers at the water-air interface at 20°C.	39
3.16	Compression- expansion cycles of a) F12-phenyl-H12 and b) F12-O-phenyl-O-H12 at 20°C.	39
3.17	a) Whole surface pressure/area isotherm of F12-O-phenyl-O-H12 at 20°C and b) surface pressure/area isotherms of F12-O-phenyl-O-H12 at different temperatures.	40
3.18	a) Interfacial frequency sweep data of F12-phenyl-H12 (red symbols) at 2 mN/m and water (black symbols). b) Interfacial frequency sweep data of F12-O-phenyl-O-H12 as functions of frequency at 2 mN/m (red symbols), 4 mN/m (green symbols), 8 mN/m (magenta symbols), 15 mN/m (cyan symbols) and water (black symbols). G' (closed symbols), G'' (open symbols)	41
3.19	Interfacial viscosity of F12-phenyl-H12, F12-O-phenyl-O-H12 and water as a functions of frequency at 20°C.	41
3.20	Interfacial rheology of F12-O-phenyl-O-H12. a) Creep test using the Double Wall Ring (DWR) fixture. The shear stress applied was 10^{-4}Pa m. b) Dynamic moduli, i.e. G' (open circles) and G'' (closed circles), extracted from creep data with their linear fits (solid lines).	42
3.21	Neutron reflectivity curve and Scattering Length Density profile (inset) of F12-phenyl-H12 at the air/D ₂ O interface. Surface pressures: 2 mNm ⁻¹ (blue color) and the fit (black line). The normalized intensity is denoted as I (a.u.).	43

3.22	Neutron reflectivity curve and Scattering Length Density profile (inset) of F12-O-phenyl-O-H12 at the air/D ₂ O interface. Surface pressures: 2 mNm ⁻¹ (red color) and 20 mNm ⁻¹ (green color). The fits are presented with the black lines. The normalized intensity is denoted as I (a.u.).	44
3.23	Height images (A, C) and phase images (B, D) of F12-phenyl-H12 film transferred at 2 mNm ⁻¹ . Images C and D are recorded at higher magnification.	45
3.24	Height images (A, C) and phase images (B, D) of F12-O-phenyl-O-H12 film transferred at 2 mNm ⁻¹ . Images C and D are recorded at higher magnification.	45
3.25	Height images (A, C) and phase images (B, D) of F12-O-phenyl-O-H12 film transferred at 13 mNm ⁻¹ . Images C and D are recorded at higher magnification.	46
3.26	Compression- expansion cycles of 2F12-core-2H12 at 20°C.	47
3.27	Compression- expansion cycles of 2H-core-2H12 at 20°C.	48
3.28	The role of preshear at $\omega=10$ rad/s for 2 min for 2F12-core-2H12. G' (closed symbols) G'' (open symbols).	49
3.29	a) Interfacial frequency sweep data of 2F12-core-2H12 at 20°C. The surface moduli are depicted as functions of frequency at 0 mNm ⁻¹ (black colour), 1 mNm ⁻¹ (red colour), 2 mNm ⁻¹ (magenta colour), 3 mNm ⁻¹ (blue colour) measured on Double Wall Ring (DWR). b) Dynamic Strain Sweep measurement of 2F12-core-2H12 at four different surface pressures, 0 mNm ⁻¹ (black colour), 1 mNm ⁻¹ (red colour), 2 mNm ⁻¹ (magenta colour), 3 mNm ⁻¹ (blue colour) measured on Double Wall Ring (DWR). G' (closed symbols) G'' (open symbols).	49
3.30	a) Interfacial rheology of 2H-core-2H12 measured on the bi-conical fixture at surface pressure 12 mNm ⁻¹ . a) Dynamic Frequency Sweep measurement at strain amplitude $\gamma=0.01$ % and $\gamma=0.1$ % and b) Dynamic Strain Sweep measurement at $\omega=0.65$ rad/s . G' (closed symbols) G'' (open symbols).	50
3.31	Neutron reflectivity curve and Scattering Length Density profile (inset) of 2F12-core-2H12 at the air/D ₂ O interface. Surface pressures: 2 mNm ⁻¹ (green color), the fit (black line) and D ₂ O reflectivity data (blue colour). The normalized intensity is denoted as I (a.u.).	52
3.32	Neutron reflectivity curve and Scattering Length Density profile (inset) of 2H-core-2H12 at the air/silicon wafer interface. Surface pressures: 2 mNm ⁻¹ (red color) and the fit (red line), silicon wafer reflectivity data (blue color) and its fit (blue line). The normalized intensity is denoted as I (a.u.).	52
3.33	Height images (A, C) and phase images (B, D) of 2F12-core-2H12 film transferred at 2 mNm ⁻¹ . Images C and D are recorded at higher magnification.	53

4.1	Chemical structures of (a) bis(4-octylphenyl)diazene (abbreviated H8-azo-H8), (b) [4 (heptadecafluorooctyl)phenyl](4-octylphenyl)diazene (abbreviated F8-azo-H8) and (c) light-induced change of conformation from trans to cis.	59
4.2	Surface pressure (Π) versus molecular area (A) isotherms of F8-azo-H8 monolayers at the air-water interface at 20°C, under different irradiation conditions: UV light inducing predominantly cis configuration (right curve in purple, labelled "UV"), visible light with cis and trans configurations (middle curve, orange, "VISIBLE") and in the dark with trans configurations (left curve, green, "DARK"). The arrows indicate compression and expansion directions with very little hysteresis. . .	61
4.3	Surface pressure (Π) versus molecular area (A) isotherms of H8-azo-H8 monolayers at the air-water interface at 20°C. Under UV light with cis configurations (right, purple curve), under visible light with cis and trans configurations (middle, orange) and in the dark with trans configurations (left, green).	62
4.4	Variation of the surface pressure (Π) overtime (t) for a) a F8-azo-H8 monolayer (pure water subphase, 20°C) under different light stimuli. In the dark (black), UV (green), and visible light (blue) and b) for a H8-azo-H8 monolayer at the air-water interface at 20°C. Under dark (left / green, start), UV (middle / purple), dark (last / black)	63
4.5	Dynamic time sweep measurement of storage (G' , closed symbols) and loss (G'' , opened symbols) moduli for F8-azo-H8 films at the air-water interface at a temperature of 20°C, frequency $\omega=0.6 \text{ rad s}^{-1}$ and strain amplitude $\gamma_0=0.1\%$ using the magnetic rod interfacial stress rheometer. The measurement started at a surface pressure of a) 6 mNm^{-1} and b) 12 mNm^{-1} . Light conditions: UV off, then UV on.	64
4.6	Storage modulus (G') versus surface pressure of the F8-azo-H8 monolayer at the air-water interface showing the order of magnitude decrease of the elastic modulus under UV irradiation for three different starting surface pressure, $\Pi=2\text{mNm}^{-1}$, $\Pi=6\text{mNm}^{-1}$ and $\Pi=12\text{mNm}^{-1}$. . .	65
4.7	Dynamic frequency sweep measurement of storage (G' , closed symbols) and loss (G'' , opened symbols) moduli for a H8-azo-H8 monolayer at the air-water interface at a temperature of 20°C at strain amplitude $\gamma_0=0.1\%$ using the magnetic rod interfacial stress rheometer. The measurement started at a surface pressure of 2 mNm^{-1} (black symbols) and then after the UV was on the surface pressure increased to 8 mNm^{-1} (red symbols).	66
4.8	Neutron reflectivity curve (Normalized Intensity ($I(\text{a.u.})$) vs q) of the F8-azo-H8 monolayer on a D_2O subphase in the dark next to the corresponding scattering length density profile in the lower inset. Upper inset: Normalized Intensity (NR) $\cdot q^4$ versus q . Colour legend: D_2O (black), F8-azo-H8 under dark (orange) and fit (green). $\Pi= 2 \text{ mNm}^{-1}$ at 20°C.	67

4.9	Neutron reflectivity curve (Normalized Intensity (I(a.u.) vs q) of the F8-azo-H8 monolayer on a D ₂ O subphase under UV irradiation together with the scattering length density profile in the lower inset. Upper inset: Normalized Intensity (NR)*q ⁴ vs q. Colour legend: D ₂ O (black), F8-azo-H8 under UV (orange) and fit (green). $\Pi=12\text{mNm}^{-1}$ at 20°C. .	68
4.10	Model proposed for F8-azo-H8 monolayer at the water-air interface before and after its exposure to UV light.	68
4.11	Neutron reflectivity curve (Normalized Intensity (I(a.u.) vs q) of the H8-azo-H8 monolayer on a D ₂ O subphase in the absence of light and under UV irradiation along with the scattering length density profile in the lower inset. Upper inset: Normalized Intensity (NR) * q ⁴ versus q. Colour legend: D ₂ O (black), H8-azo-H8 under dark (orange), H8-azo-H8 under UV (green) and fit (red). Surface pressure= 2 mNm ⁻¹ under dark and $\Pi=8\text{mNm}^{-1}$ under UV at 20°C.	69
4.12	Model proposed for the H8-azo-H8 monolayer at the air-water interface before and after its exposure to UV light.	69
5.1	Interfacial rheometry flows a) shear, b) planar extension and c) dilatation.	73
5.2	Surface pressure/area isotherm of PMMA (270k) monolayer at the water-air interface at 20°C.	77
5.3	Compression- expansion cycles of PMMA (270k). Left panel: before and Right panel: after transition at $\Pi=12\text{mNm}^{-1}$ at 20°C.	77
5.4	Model of PMMA layers at the air-water interface a)gas-phase, b)liquid-phase, c)solid-phase and d)buckling-phase	78
5.5	Linear and nonlinear rheology of PMMA (270k) using the ISR with channel width 0.9 cm a) dynamic frequency sweep measurement at $\gamma=0.1\%$ and b) dynamic strain sweep at $\omega=0.6\text{ rad/s}$. G' (closed symbols) and G'' (open symbols).	81
5.6	FT magnitude spectra of PMMA using the ISR with channel width 0.9 cm at strain amplitude of $\gamma=1\%$. Inset: Normalized amplitudes of the 2 nd harmonics of PMMA as a function of strain amplitude. The excitation frequency was $\omega_1/2\pi = 0.1\text{ Hz}$	82
5.7	Case of PMMA(270k) monolayer using the ISR with channel width 0.9 cm at strain amplitude of $\gamma=1\%$ and excitation frequency of $\omega_1/2\pi = 0.1\text{ Hz}$. Left panel: measurement of the displacement versus time after an applied force. Right panel: Bowditch-Lissajous plot of function generator in mV versus the rod position in pixel.	83
5.8	Linear and nonlinear rheology of PMMA (270k) using the ISR with channel width 0.7 cm a) dynamic frequency sweep measurement at $\gamma=0.1\%$ and b) dynamic strain sweep at $\omega=0.6\text{ rad/s}$. G' (closed symbols) and G'' (open symbols).	84

5.9	FT magnitude spectra of PMMA using the ISR with channel width 0.7 cm at strain amplitude of $\gamma = 1\%$. Inset: Normalized amplitudes of the 2 nd harmonics of PMMA as a function of strain amplitude. The excitation frequency was $\omega_1/2\pi = 0.1$ Hz. In Figure D.1 the Log-Linear plot is presented.	85
5.10	Case of PMMA(270k) monolayer using the ISR with channel width 0.7 cm at strain amplitude of $\gamma = 1\%$ and excitation frequency of $\omega_1/2\pi = 0.1$ Hz. Left panel: measurement of the displacement versus time after an applied force. Right panel: Bowditch-Lissajous plot of function generator in mV versus the rod position in pixel.	86
5.11	A cartoon of PMMA-grafted glassy needle.	87
5.12	Linear and nonlinear rheology of PMMA (270k) using the ISR with a PMMA-grafted glassy needle a) dynamic frequency sweep measurement at $\gamma = 0.1\%$ and b) dynamic strain sweep at $\omega = 0.6$ rad/s. G' (closed symbols) and G'' (open symbols).	88
5.13	FT magnitude spectra of PMMA using the ISR with a PMMA-grafted glassy needle at strain amplitude of $\gamma = 1\%$. Inset: Normalized amplitudes of the 2 nd harmonics of PMMA as a function of strain amplitude. The excitation frequency was $\omega_1/2\pi = 0.1$ Hz.	89
5.14	Case of PMMA(270k) monolayer using the ISR with a PMMA-grafted glassy needle at strain amplitude of $\gamma = 1\%$ and excitation frequency of $\omega_1/2\pi = 0.1$ Hz. Left panel: measurement of the displacement versus time after an applied force. Right panel: Bowditch-Lissajous plot of function generator in mV versus the rod position in pixel.	89
5.15	A cartoon of PMMA-grafted channel.	90
5.16	Linear and nonlinear rheology of PMMA (270k) using the ISR with a PMMA-grafted channel a) dynamic frequency sweep measurement at $\gamma = 0.1\%$ and b) dynamic strain sweep at $\omega = 0.6$ rad/s. G' (closed symbols) and G'' (open symbols).	91
5.17	FT magnitude spectra of PMMA using the ISR with a PMMA-grafted channel at strain amplitude of $\gamma = 2\%$. Inset: Normalized amplitudes of the 2 nd harmonics of PMMA as a function of strain amplitude. The excitation frequency was $\omega_1/2\pi = 0.1$ Hz.	92
5.18	Case of PMMA(270k) monolayer using the ISR with a PMMA-grafted channel at strain amplitude of $\gamma = 2\%$ and excitation frequency of $\omega_1/2\pi = 0.1$ Hz. Left panel: measurement of the displacement versus time after an applied force. Right panel: Bowditch-Lissajous plot of function generator in mV versus the rod position in pixel.	93
5.19	Phases of the 2 nd harmonics versus strain amplitude for PMMA monolayer measured using different techniques: channel with $W = 0.9$ cm (red colour), channel with $W = 0.7$ cm (black colour), grafted needle (green colour) and grafted channel (blue colour).	93

5.20	Nonlinear rheology of PMMA (270k) using the bi-conal fixture. Dynamic strain sweeps at $\omega=0.6$ rad/s. Concentration 146.27 mg/m ² (square symbols) and 73.14 mg/m ² (circle symbols). G' (closed symbols) and G'' (open symbols). [The author kindly acknowledge Patrick Ruehs for having performed the DSS experiment in ETH in the group of P. Fisher.]	95
5.21	FT magnitude spectra of PMMA using the biconal fixture at strain amplitude of $\gamma=1\%$. The excitation frequency was $\omega_1/2\pi = 0.1$ Hz. . . .	95
5.22	Case of PMMA(270k) monolayer using the bi-conical fixture at strain amplitude of $\gamma=1\%$ and excitation frequency of $\omega_1/2\pi = 0.1$ Hz. Left panel: measurement of the stress versus time after an applied deformation. Right panel: Bowditch-Lissajous plot of the LAOS data.	96
5.23	Linear and nonlinear rheology of PMMA (270k) using the double wall ring fixture a) dynamic frequency sweep measurement at $\gamma=0.1\%$ and b) dynamic strain sweep at $\omega=0.6$ rad/s. G' (closed symbols) and G'' (open symbols).	97
5.24	FT magnitude spectra of PMMA using the double wall ring fixture at strain amplitude of $\gamma=1\%$. The excitation frequency was $\omega_1/2\pi = 0.1$ Hz.	98
5.25	Case of PMMA(270k) monolayer using the double wall ring fixture at strain amplitude of $\gamma=1\%$ and excitation frequency of $\omega_1/2\pi = 0.1$ Hz. Left panel: measurement of the torque versus time. Right panel: Bowditch-Lissajous plot of the LAOS data, plotting the torque versus the displacement.	98
6.1	Surface pressure/area isotherms and compression-expansion cycles at 20°C for a) E6D30 ($M_w=1600$ gmol ⁻¹), b) E10D30 ($M_w=2400$ gmol ⁻¹), c) E11D80 ($M_w=5800$ gmol ⁻¹), d) E6D80E6 ($M_w=6300$ gmol ⁻¹), e) E40D80 ($M_w=7200$ gmol ⁻¹) and f) E10D80E10 ($M_w=7900$ gmol ⁻¹). These data are taken thanks to the collaboration with Mor Armon (University of Negev, Beer-Sheva, Israel).	105
6.2	All the surface pressure/area isotherms at 20°C of E6D30 (black), E10D30 (blue), E11D80 (red), E6D80E6 (green), E40D80 (orange) and E10D80E10 (magenta).	106
6.3	Surface pressure/area isotherms of Figure 6.2 replotted in terms of the fractional area occupied by the PDMS ($\phi=A_0/A$). The inset of this figure shows how A_0 is estimated.	107
6.4	Flory radii versus total number of repeated units (N) describing by a scaling law.	108
6.5	Left panel: Theoretical values of radii of gyration as a function of the PDMS repeated units (N_D). Right panel: Experimental Flory radii versus N_D of the diblock copolymers.	108
6.6	Interfacial rheology measurements of E6D30. Left panel: torque versus time for different shear rates. 0.05s ⁻¹ (red), 0.1s ⁻¹ (orange), 0.5s ⁻¹ (blue), 1s ⁻¹ (cyan), 1.5s ⁻¹ (magenta), 2s ⁻¹ (purple) and 2.5s ⁻¹ (green).	110

6.7	Interfacial time sweep data of E6E30 at $\omega=0.1\text{Hz}$ and $\gamma=0.1\%$. G' (closed symbols) G'' (open symbols).	110
A.1	Comparison between the performance of homemade glassy needles and glassy needles bought from KSV.	117
A.2	Characterization of metallic needles.	118
A.3	Characterization of glassy needles.	119
B.1	Mini Langmuir trough to measure oil-water interfaces.	120
B.2	Surface pressure/area isotherms of palmitic acid at the water-air interface at 20°C using the big Langmuir trough and the new mini trough.	121
B.3	Surface pressure/area isotherms of E10D80E10 at the isooctane-water interface at 20°C using the mini Langmuir trough. Spreading volume $9\mu\text{l}$ (blue data), $10\mu\text{l}$ (green data) and $18\mu\text{l}$ (red data).	122
B.4	Surface pressure/area isotherms of PS particles. Left panel: at the water-air interface and Right panel: at the isooctane-water interface at 20°C using the mini Langmuir trough. Spreading volume $5\mu\text{l}$ (blue data) and $3\mu\text{l}$ (red data).	122
C.1	Extra neutron reflectivity data (red symbols) and fits (black lines) where CF-UP model structures have been considered for a) F12-phenyl-H12, b) F12-O-phenyl-O-H12 and c) F8-azo-H8 under dark. In the inset a schematic representation of the model is presented with the alkane parts to be drawn as black segments and the fluorocarbon parts as white segments.	124
D.1	Log-Linear plot of FT magnitude spectra of PMMA using the ISR with channel width 0.7 cm at strain amplitude of $\gamma=1\%$. The excitation frequency was $\omega_1/2\pi = 0.1\text{ Hz}$	125
D.2	Log-Linear plot of FT magnitude spectra of PMMA using the ISR with a PMMA-grafted glassy needle at strain amplitude of $\gamma=1\%$. The excitation frequency was $\omega_1/2\pi = 0.1\text{ Hz}$	125

CHAPTER 1

INTRODUCTION

We have studied the interplay between structure and rheology of molecular systems at fluid interfaces and more specifically, films that have the thickness of one molecule at the air-water interface. Up to now, a great progress has been done on the tunability of structural and viscoelastic properties of 3D (bulk) systems. The goal of this thesis is to address a similar tunability in two-dimensional systems of films. We focused on the film properties of a novel series of semifluorinated alkanes, homopolymers and block copolymer systems. Firstly, we study the tunability of the films by systematically altering the chemical composition of the semifluorinated alkanes focusing on the ductility of the monolayers. Secondly, tailoring of the film properties was accomplished by application of external light stimuli to photo-sensitive semifluorinated alkanes for investigating the tunability of the semifluorinated film properties. Apart from semifluorinated alkane molecules that are constituted by two hydrophobic segments, we study the interfacial properties of a series of amphiphilic block copolymers and simple homopolymers at the air water interface. These are molecules consisting of one hydrophilic group that is bound at the aqueous subphase and one hydrophobic group. Finally, we investigated the presence of even harmonics using different interfacial rheometry techniques by implementation of Fourier transform analysis.

Over the last years, the interfacial rheology of gas/liquid and liquid/liquid interfaces has become a very important research field because of the numerous applications in food industry (Dickinson *et al.* (1991)), in biomedical applications (Zasadzinski *et al.* (2001)) and in the stability of emulsions and foams (Georgieva *et al.* (2009)) in personal care products. There are two types of interfacial rheometry techniques, the shear and the dilatational rheology. In this thesis we study the interfacial properties of insoluble monolayers using shear rheology with a magnetic rod interfacial stress rheometer, the double wall ring fixture and the bi-conical fixture mounted on commercial rheometers. In order to account for the sensitivity of each set up, a dimensionless number that is called Boussinesq number ($Bo = \eta_s / \eta_G$) is introduced to describe the importance of the surface drag with respect to the subphase drag. The interfacial viscosity (η_s) has units

of 'Pa s m' and the bulk viscosity (η) has units of 'Pa s', so the G parameter (in the previous equation) is a characteristic length scale of each set up, typically the length of the interfacial probe. According to the value of G we can estimate how sensitive each technique is. The most sensitive is the magnetic rod interfacial stress rheometer that minimizes G that corresponds to the radius of the needle (order of several hundred μm). However, in the magnetic rod interfacial stress rheometer the dynamic range of each individual rod is limited. The double wall ring has also good sensitivity with a characteristic length twice bigger (orders of few millimeter) than the magnetic rod's one. Comparing the sensitivity of the bi-conical device with the previous techniques, the characteristic length scale of the bi-conical device is related to the radius of the geometry (orders of centimeters) and consequently small values of B_0 (huge subphase contribution to the deformation profile). Nevertheless, despite the almost 50 times bigger characteristic length of the bi-conal device, the bi-conal has a dynamic range larger than the double wall ring.

In this thesis we study Langmuir monolayers, which consist either of hydrophobic segments or one hydrophilic head (an acid or alcohol group) and one hydrophobic tail. Langmuir monolayers attracted the attention during the last decades because of their applications especially in the biomedical field, as model two-dimensional systems of cell membranes (Grimard *et al.* (1993)), as lung surfactants (Clements and Avery (1998)) and as tear films (Riess (2009)). Also Langmuir monolayers find application in thin film technology mostly as sensors (Swalen *et al.* (1987)).

In Chapter 2 we describe the experimental set ups that were used in this thesis and a short description of the materials that were used to create monolayers at the air-water interface, semifluorinated alkanes, homopolymers (PMMA) and block copolymers (di-blocks and triblocks of PEO-PDMS). Firstly, we present the set up of the Langmuir trough, a technique that has been widely used in order to compress deposited layers at the air-water interface and measuring the change of the surface pressure (in mNm^{-1}) upon compression and expansion. Secondly, the apparatus of the Langmuir trough is equipped with magnetic coils and a camera in order to measure the interfacial rheology, this set up is called magnetic rod interfacial stress rheometer. For further investigation of the rheological properties of the layers at gas/liquid and liquid/liquid interfaces, a double wall ring fixture and a bi-conical device have been mounted onto commercial rheometers, a Discovery Hybrid Rheometer (DHR-TA Instruments) and an Anton-Paar

respectively. Finally, we present neutron reflectivity measurements that were performed to characterize the different structures characterizing the films at air-water interface.

In Chapter 3 we study systematically the effect of molecular architecture of semi-fluorinated alkanes on structure and rheology. Taking advantage of the possible synthesis of various semifluorinated alkanes we start from a linear-symmetric molecule and we vary the molecular architecture by creating more complex branched structures. The results indicated that the linear reference system has a ductile response upon increasing the surface pressure. This ductility was suppressed by moving to more branched structures, but in both cases the molecules had perpendicular structures at the air-water interface with the fluorocarbons to point towards the air. However, by inserting small groups (phenyl rings and oxygens) between the fluorinated and alkane chains the molecules were lying flat at the interface exhibiting a viscous-like response.

Chapter 4 describes the effect of UV light to monolayers made by semifluorinated alkyl-azobenzene derivatives. It was found that the UV irradiation influences dramatically the interfacial properties of the monolayers. Moving from trans to cis configurations under UV irradiation the molecules occupy three times bigger molecular area. Moreover, moving from trans to cis configurations the surface pressure is increased and in the same time the interfacial moduli decrease almost one order of magnitude.

In Chapter 5 we focus on the non-linear rheology of PMMA monolayers at the air-water interface. The goal of this chapter is to compare the presence of second harmonics between different interfacial rheology techniques, targeting in the elimination of the second harmonics that are related with slip phenomena. We analyzed with Fourier transform the time domain signals from dynamic strain sweep measurements using the interfacial stress rheometer, the double wall ring fixture and the bi-conical device. Using the magnetic rod interfacial stress rheometer, we used different sizes of channels, a grafted glassy needle with PMMA and a grafted channel with PMMA. The results indicate no higher harmonics using the DWR and the bi-conical fixture. However, the presence of even harmonics was shown using the magnetic rod interfacial stress rheometer for all the investigated cases.

Chapter 6 describes the formation of Langmuir monolayers of PEO-PDMS block copolymers at the air-water interface. We found that the diblock and triblocks form stable reversible monolayers at the air-water interface with a phase transition. We also

obtained a power law behaviour of the Flory radii as a function of the number of repeated units and we found that the system scales as $R_F \sim N^\nu$, with $\nu=0.56 \pm 0.01$, that is characteristic for Langmuir films in poor solvent conditions. Finally, interfacial rheology measurements performed on PEO-PDMS films showed their Newtonian behaviour.

CHAPTER 2

MATERIALS AND METHODS

2.1 The technique of "Langmuir Trough"

Many are the ways of studying molecular systems confined between two immiscible fluids: 1) The Langmuir monolayers that are insoluble, 2) the Langmuir-Blodgett (LB) films and 3) the Gibbs monolayers. Langmuir films should not be confused with LB films (Blodgett (1939)). In LB films one or more monolayers of an organic material are deposited from the surface of a liquid onto a solid substrate by emerging the solid substrate into (or from) the liquid. Apart from the insoluble Langmuir monolayers there are the Gibbs monolayers that are soluble in one of the phases separated by the interface on which the monolayer is formed (Figure 2.1). The Langmuir trough set-up was invented to study insoluble monolayers at the water-air interface. Its name is given after Irving Langmuir because of his pioneering work at 1917 (Langmuir (1917), Langmuir (1920)).

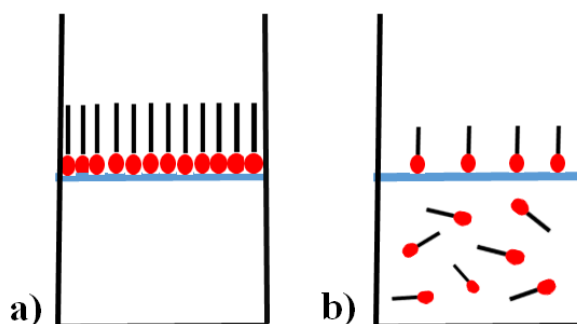


Figure 2.1: a) Langmuir films and b) Gibbs films.

The trough (KSV Instruments, Helsinki, Finland) (Fig. 2.2) typically is attached to a metal block in contact with a bath in order to allow temperature control. The trough is made of teflon, a material that is easy to keep clean. The two barriers are made of a hydrophilic material and they move towards/away from each other in order to change the surface concentration of the molecules at the interface. The Wilhelmy

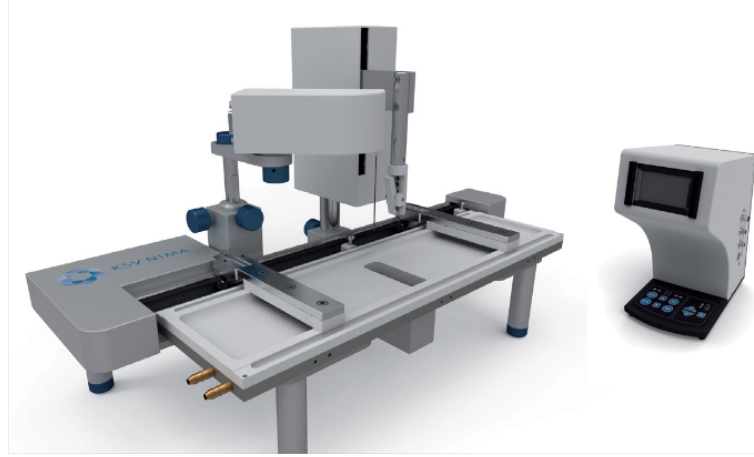


Figure 2.2: KSV NIMA Langmuir-Blodgett Trough. This image is taken from the official webpage of KSV Instruments (www.biolinscientific.com/ksvnima/products/).

plate is usually made by platinum or filter paper and is partially merged at the water-air interface. The Wilhelmy balance is responsible for monitoring the surface tension according to eq. 2.1. The surface pressure, Π , is the surface tension of the monolayer, Γ , subtracted from the surface tension of the water, Γ_0 , that is 72.8 mN/m at 20 °C (Gaines (1966)).

$$\Pi = \Gamma_0 - \Gamma \quad (2.1)$$

For the preparation of the monolayer, the diblocks have to be dissolved in a mutual volatile solvent. Using a microsyringe the solution is deposited drop-wise at the interface. A time of around 15 min is needed for the solvent evaporation. Subsequently, the barriers start to move inwards varying the concentration of the monolayer. The surface pressure-area isotherm indicates several phase transitions of the monolayer. In Fig. 2.3 a typical compression surface pressure isotherm of a Langmuir monolayer is presented. The surface pressure zero corresponds to the gas-like state of the monolayer and the liquid-like and solid-like states of the monolayer occur upon compression. These diagrams are analogous to the three dimensional pressure-volume isotherms at a constant temperature.

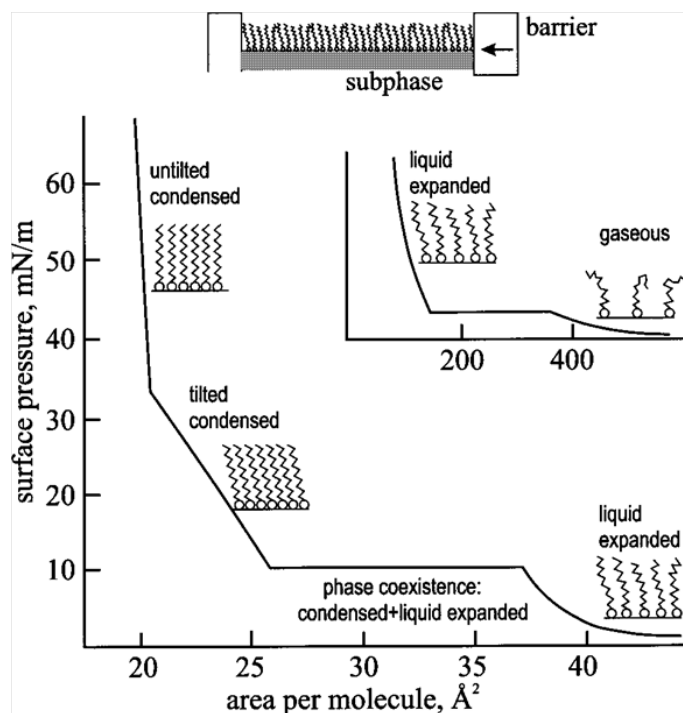


Figure 2.3: A generalized isotherm curve of Langmuir monolayer. The image is taken from Kaganer *et al.* (1999).

2.2 Interfacial Rheometry Techniques

2.2.1 Magnetic Rod Interfacial Stress Rheometer (ISR)

The magnetic rod interfacial stress rheometer (ISR) was developed by Brooks *et al.* (1999) in order to study the rheology of Langmuir films. Figure 2.4 illustrates the basic components of an interfacial stress rheometer.

According to the design of Brooks *et al.* (1999), a commercial Langmuir trough (KSV Instruments, Helsinki, Finland) is equipped by a pair of Helmholtz coils to generate a magnetic field gradient. This gradient applies a force on a magnetized rod that is supported by surface tension at the water-air interface. In the set up where this thesis was performed, the magnetized rod is positioned in the middle of a channel with a variable width R . The position of the needle is detected by a camera which is focused at the edge of the needle. In other ISR set ups, according to Brooks *et al.*, the position of the rod is detected by an inverted microscope and the resulting image is projected onto a photodiode array.

A sketch of the wiring diagram of the ISR is presented in Figure 2.5. In a typ-

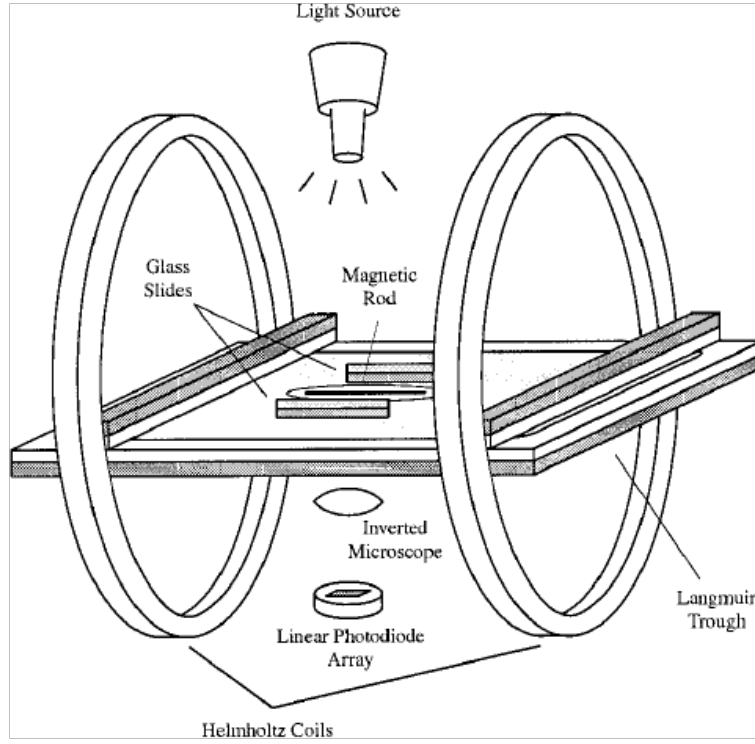


Figure 2.4: Schematic representation of the magnetic rod interfacial stress rheometer. This image has been taken from Brooks *et al.* (1999).

ical set up the one of the magnetic coils generates a magnetic field gradient and the other produces a constant magnetic field by fixing the orientation of the magnetic needle. There are two dc power supplies (Hewlett-Packard Model 6644A) that are used to drive the pair of Helmholtz coils. The current setpoint of one of these power supplies is controlled by an analog signal from a function generator (Hewlett-Packard Model 3325B) to create a time dependent magnetic field gradient. A third dc dual-power supply (Hewlett-Packard Model 6205C) is used to power the constant field coils. The forces that can be applied with the present design range from 0.001 to 30 μN .

The flow cells (Fig. 2.6) are made of hydrophilic material promoting good alignment of the magnetic rod along the channel centerline. The meniscus created by the hydrophilic material contributes to the self-centering of the needle. In Figure 2.6 the geometry produces a linear velocity profile neglecting the influence of the subphase. This problem is solved both numerically and analytically starting from the Navier-Stokes equations and using the generalized Boussinesq-Scriven equation as a suitable boundary condition (Verwijlen *et al.* (2011)). In the work of (Verwijlen *et al.* (2011)) good agreement was found between analytical solutions, numerical simulations and experiments describing the flow field and the resulting local interfacial shear rate at the

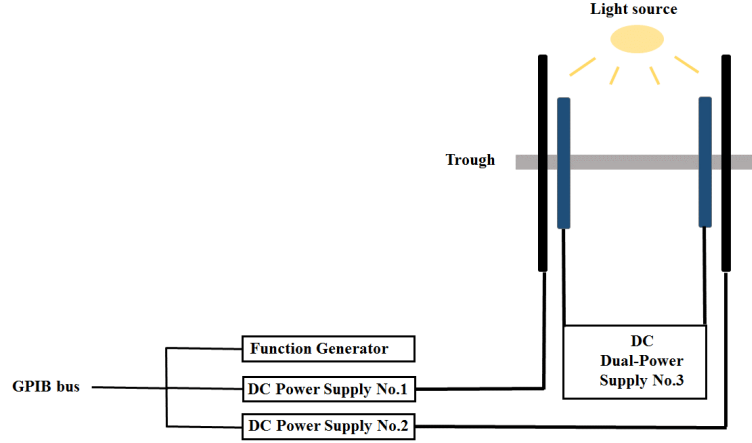


Figure 2.5: Sketch of the wiring diagram for the interfacial stress rheometer.

rod. Based on this research, an algorithm to correct the experimental data of different types of interfacial shear rheometers and geometries was proposed and evaluated. The Boussinesq number (eq.2.2) is important to estimate the relative surface and subphase contributions. When $Bo \gg 1$, the surface stresses dominate, while when $Bo \ll 1$ the subphase stresses dominate. It is defined as:

$$Bo = \frac{\eta_S \frac{V}{L_I} P_I}{\eta \frac{V}{L_S} A_S} = \frac{\eta_S L_S P_I}{\eta L_I A_S} = \frac{\eta_S}{\eta \alpha} \quad (2.2)$$

where,

η_S : the surface viscosity in Pa s m,

η : the bulk viscosity of the subphase,

V : the characteristic velocity,

L_I : the characteristic length scale at which the velocity decays at the interface,

L_S : the characteristic length scale at which the velocity decays at, the subphase,

P_I : the contact perimeter between the rheological probe and the interface and

A_S : the contact area between the probe and the subphase.

The parameter α is related to the radius of the entire geometry. For example, for the magnetic needle it is determined by the radius of the needle. According to eq.2.2, a small value of α , would be preferable to achieve a sensitive interfacial rheometry device.

Calibration Method

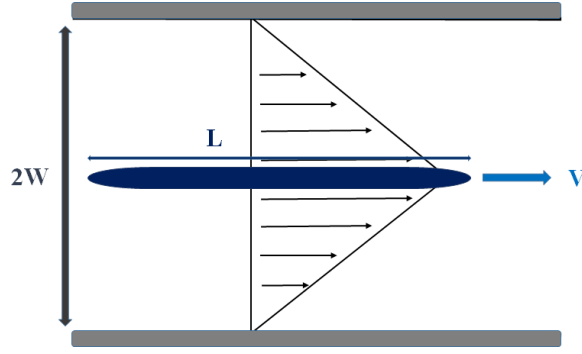


Figure 2.6: The flow cell with the magnetic needle.

For oscillatory deformations, a sinusoidal signal is applied to the rod in a range of frequencies $0.1 \leq \omega \leq 10$ rad/s. The applied sinusoidal force and the displacement of the rod are recorded as a function of time as it can be seen in Figure 2.7. The amplitude ratio and the phase difference of the signals are calculated from a fast Fourier transform (FFT) of the signals.

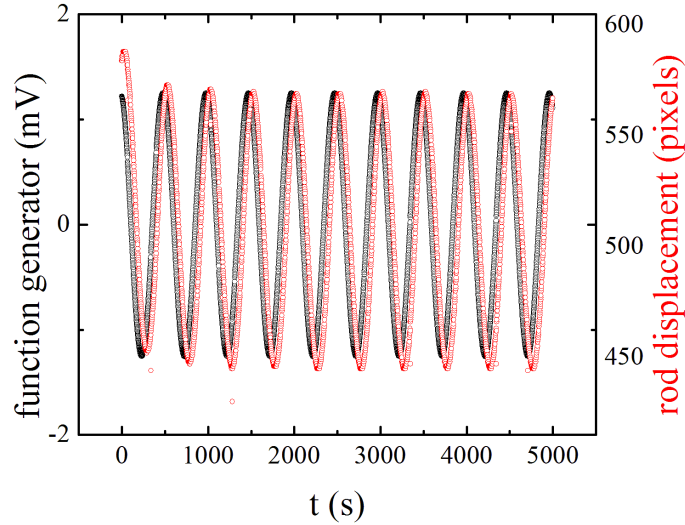


Figure 2.7: Sinusoidal signals of the applied force and the displacement taken from the magnetic rod ISR.

According to Brooks *et al.* (1999), in Figure 2.8 the measured amplitude ratio (AR_{system}) and phase difference (δ_{system}) of the monolayer-free interface is presented as a function of forcing frequency. The total frequency behaviour can be characterized by a second order system according to equations 2.3 and 2.4, with a low frequency

plateau, a damped resonance peak at 1 rad/s and inertial dampening at high frequencies.

$$AR_{system} \equiv \frac{\text{Rod Position Amplitude}}{\text{Force Amplitude}} = \frac{1}{\sqrt{(k - m\omega^2)^2 + (\omega d)^2}} \quad (2.3)$$

$$\delta_{system} \equiv \arctan\left(\frac{-\omega d}{k - m\omega^2}\right) \quad (2.4)$$

The parameters k , d , and m are analogous to a spring constant, damping coefficient and a mass of the magnetic rod, respectively.

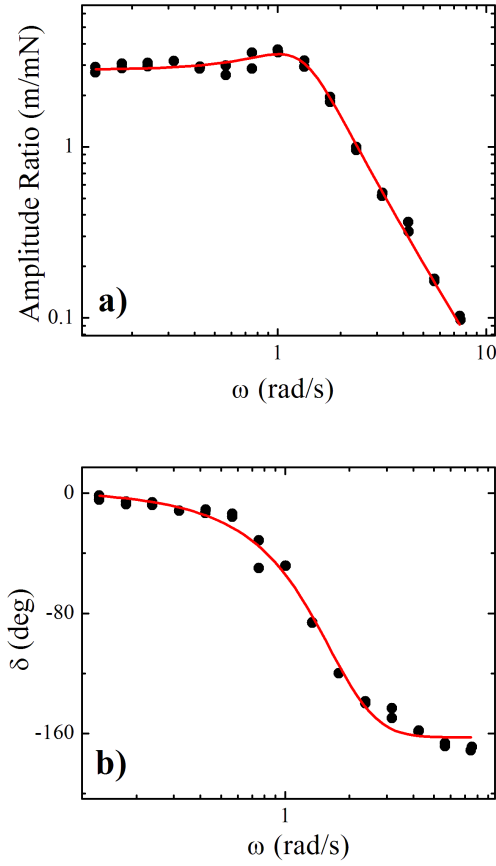


Figure 2.8: (a) Amplitude ratio and (b) phase angle as a function of forcing frequency for a monolayer-free interface.

The amplitude ratio has units of distance per current. However, the units of current have to be converted to units of force. From equation 2.3, taking the square and reciprocating

both sides of the equation, at high frequencies we have:

$$\frac{1}{(AR_{system})^2} = (k - m\omega^2)^2 + (\omega d)^2 = m^2\omega^4 + (d^2 - 2km)\omega^2 + k^2 \sim m^2\omega^4 \quad (2.5)$$

At high frequencies the equation 2.5 can be written as follows:

$$\frac{C^2}{(AR_{system})^2} \sim m^2\omega^4 \quad (2.6)$$

where C is the calibration constant in units of force/current.

Data analysis for oscillatory deformations

According to Brooks *et al.* (1999) two basic assumptions take place for the analysis of the data. First, the velocity profile that is created between the rod and the stationary walls is a linear shear profile and so, the displacement of the rod is a direct measure of the interfacial strain. Second, the surface contribution to the total drag is significantly larger than the subphase drag.

The surface dynamic shear modulus (G_S^*) is the proportionality between the surface stress, σ_S , and the surface strain, γ_S . G^* is a complex number:

$$G_S^*(\omega) = G_S'(\omega) + iG_S''(\omega) \quad (2.7)$$

Equation 2.8 shows the surface stress where F_0 is the drag on the rod and L is the length of the rod. The surface strain is calculated as it is shown in equation 2.9, assuming that the velocity profile between the rod and the walls is linear. In equation 2.9, z_0 is the rod displacement, R is the distance between the rod and the walls and α is the radius of the rod.

$$\sigma_S = \frac{F_0}{2L} \quad (2.8)$$

$$\gamma_S = \frac{z_0}{R - \alpha} \quad (2.9)$$

Accordingly, the surface dynamic shear modulus can be calculated knowing the geometrical parameters α , R and L as well as the amplitude ratio (AR) and the relative phase (δ) (eq. 2.10). The units of G^* in two-dimensional rheology is in $\text{Pa m} = \text{N m}^{-1}$.

$$G_S^*(\omega) = \frac{\sigma_S}{\gamma_S} e^{i\delta(\omega)} = \frac{(R - \alpha)}{2L} \frac{F_0}{z_0} e^{i\delta(\omega)} = \frac{(R - \alpha)}{2L} \frac{1}{AR} e^{i\delta(\omega)} \quad (2.10)$$

2.2.2 Double Wall Ring

The double wall ring (DWR) geometry to measure the viscoelastic properties of interfaces in shear flows has been reported by Vandebriel *et al.* (2010), Hermans and Vermant (2014). According to Vandebriel *et al.* (2010), the minimal surface viscosity that can be measured with the DWR is $5 \cdot 10^{-6} \text{ Pa s m}$. The measurements were performed in a stress controlled DHR-3 rheometer (TA Instruments) in ETH and an ARG-2 in Leuven. The sample is contained in a trough and the DWR geometry (Fig. 2.9) is positioned in an open teflon cup connected to a temperature-controlled Langmuir trough. The inside diameter of the ring is $R_5 = 34\text{mm}$ and the outside diameter $R_6 = 36\text{mm}$. The ring is made by Platinum(Pt)/ Iridium(Ir) such that it can be flame-treated for cleaning it from organic contaminants.

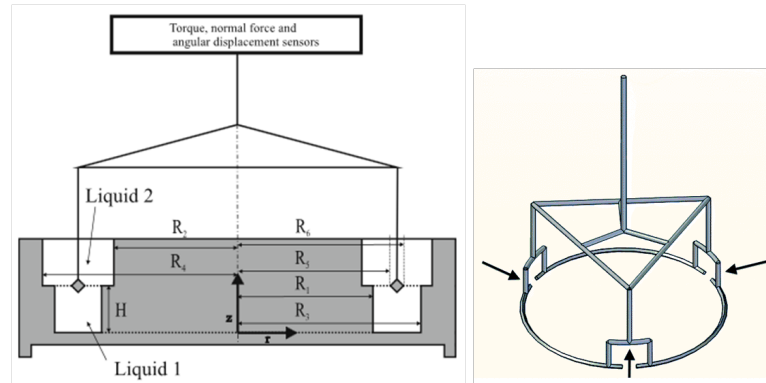


Figure 2.9: Right: A DWR and Left: Cross section of the DWR set up. This image is taken from Vandebriel *et al.* (2010).

As it is shown in Fig. 2.9, the walls of the cup and the ring geometry have small openings, allowing the interface to be homogeneous everywhere during the compression and expansion of the monolayer. The cross section of the DWR is square-shaped with a sharp edge in order to create a planar interface.

2.2.3 Bi-conal Fixture

A standard rotational rheometer was used (MCR 501, Physica) with a bi-conical geometry as it is depicted in Fig. 2.10. A full description of the bi-conical geometry rheometer is presented by Erni *et al.* (2003).

The biconal disk is oscillating or rotating with a controlled torque or rotational speed. The cup remains stable and the edge of the disk is located in the interfacial region between the two immiscible liquids or at the surface of a single liquid. The bi-conical geometry is mounted to the top driven motor and transducer unit of the rheometer. The measuring position at the interface is detected according to the normal force sensor.

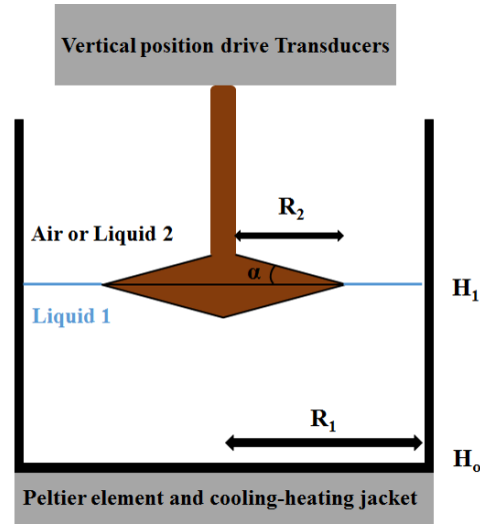


Figure 2.10: Schematic of the rotational bi-conical rheometer.

As it is depicted in Fig 2.10, the measuring cell consists of a cup that is fixed to the bottom part of the rheometer with a flange. Various cups were used made by Polytetrafluoroethylene (PTFE) or glass. The cup inner radius is $R_1=40$ mm, the disk radius $R_2=34.14$ mm and the cone angle $\alpha=5^\circ$.

A Peltier element is used to control the temperature of the cell from below and is supplemented with a brass cylinder surrounding the cup. A small recess was machined into the wall of the PTEE cup in order to minimize the formation of the meniscus. While the cell is empty the zero gap position has to be determined (H_0). One of the most crucial aspects of the measurement is the location of the bi-conical edge to the surface of the lower liquid phase. After the cup is filled with the lower phase liquid, the bi-conical tool is slowly moving downwards along the z axis and simultaneously

measures the normal force. Once H_0 is detected, the final measuring position H_1 may be calculated by adding the known volume of the disk to the liquid volume $V = \pi R_1^2 H_0$. In cases of measurements at the liquid-liquid interfaces, the low density liquid is filled with a syringe pump after the disk has been positioned at the surface of the high density liquid.

2.3 Neutron Reflectivity

Neutron reflectivity measurements were performed with the AMOR reflectometer of the Swiss Spallation Neutron Source (SINQ) at the Paul Scherrer Institute (PSI) in Switzerland. A Langmuir trough was used allowing the measurements at different surface pressures by direct measurements at the D_2O -air interface or after deposition of the layers onto silicon wafers. We use deuterated water (D_2O) instead of H_2O because hydrogen has a coherent scattering length of $-3.74 \cdot 10^{-5} \text{ \AA}$ and deuterium $6.67 \cdot 10^{-5}$, so using deuterated water the reflectivity contrast is increased. The details of the instrumentation have been described by Clemens *et al.* (2000) and Gupta *et al.* (2004).

The apparatus (AMOR) at SINQ/PSI operates in the time-of-flight (TOF) mode. It has wavelength range of $0.15 \text{ nm} < \lambda < 1.3 \text{ nm}$ as well as in the monochromatic ($\theta - 2\theta$) mode with both polarized and unpolarized neutrons. As it is represented in Figure 2.11, a pulsed cold neutron beam is produced from the end position of the neutron guide by a dual-chopper system (side-by-side) having two windows at 180° and that is rotatable with a maximum frequency of 200 Hz. Also, supermirrors (FeCoV/Ti :N) are used as polarizer/analyser with a polarization efficiency of $\sim 97\%$. A Ni/Ti multilayer is used as a monochromator, giving $\gg 50\%$ reflectivity at a wavelength of 0.47 nm.

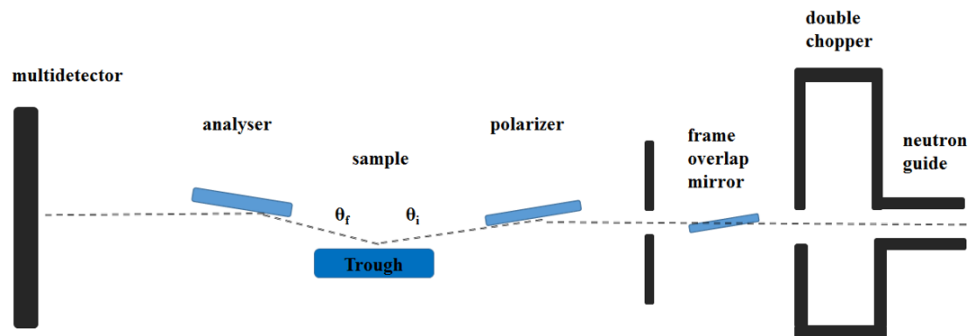


Figure 2.11: Sketch of the overall instrumental layout of the PSI reflectometer.

The measurements of this work were made at three incident angles (0.6° , 1.4° and 2.4°) which gave a range of momentum transfer Q , ($Q = (4\pi \sin \theta)/\lambda$, with λ being the wavelength and θ the angle of incidence) from 0.1 to 1.5 nm^{-1} . The obtained reflectivity data were analysed using the Parratt32 software, version 1.6 (Helmholtz-Zentrum Berlin für Materialien und Energie GmbH, Germany) according to Parratt (1954).

2.4 Scanning force microscopy

The SFA films were transferred from the water-air interface to silicon wafer substrates as it is demonstrated in Figure 2.12. The silicon wafers were located at the bottom of the trough tilted in a slight angle to one side. Then the water was pumped out carefully with a pump resulting in a lowering of the water-air interface. When the interface reached the silicon wafer substrate the SFA layer was deposited onto the silicon wafer surface. Subsequently the films were analyzed with scanning force microscopy (SFM, Dimension 3100, Bruker, United States, and MFP-3D, Asylum Research, USA) in intermittent contact mode. For the SFM measurements we used silicon cantilevers (Olympus OMCL-AC240TS, nominal tip radius $<7 \text{ nm}$, resonance frequency $50 - 90 \text{ kHz}$, spring constant $0.7 - 3.8 \text{ Nm}^{-1}$). Prior measurements the cantilevers were cleaned in an Ar plasma (Plasma Cleaner/Sterilizer PDC-002, 200W, Harrick Scientific Corp., United States) for 30 s at a pressure of approximately 1.6 mbar. All shown SFM images were flattened and analyzed using Gwyddion Software (www.gwyddion.net).

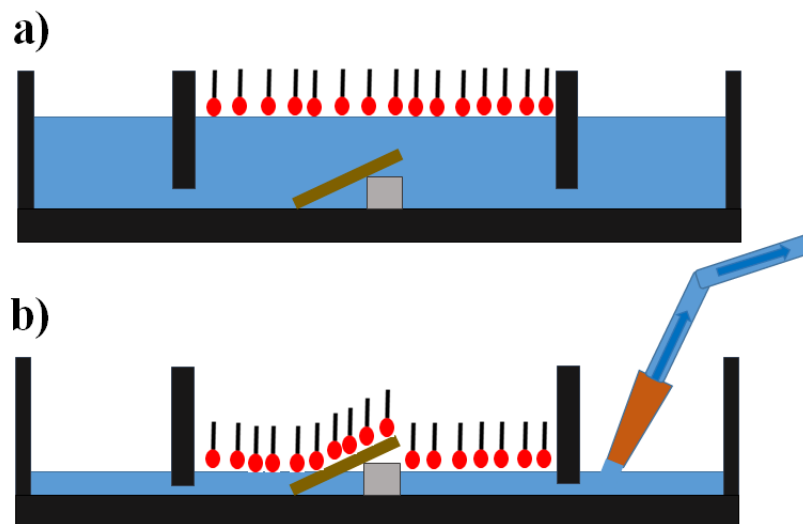


Figure 2.12: Transferring procedure of the layers onto silicon wafers. This image has been taken from Vogel *et al.* (2011)

2.5 Materials

Firstly we built Langmuir monolayers at the water-air interface using a series of semifluorinated alkanes, molecules that consist of two hydrophobic segments, one fluorinated and one hydrogenated. Secondly, monolayers of the homopolymer Poly(methyl methacrylate) (PMMA) were studied. Finally, different architectures of diblock and triblock copolymers of polyethylene oxide (PEO) and Polydimethylsiloxane (PDMS) were also investigated.

Semifluorinated alkanes

Semifluorinated alkanes (SFAs) can be considered as analogues to diblocks or surfactants because of the different chemical nature of their two blocks. They consist of linked fluorocarbon and hydrocarbon chains and are known to form Langmuir monolayers at the water-air interface (de Viguerie *et al.* (2011)). The semifluorinated alkane materials that were used in this thesis were provided from the group of Klaus Müllen from the Max Planck Institute in Mainz and their names and molecular weights are presented in Table 2.1.

In this work Perfluoro(dodecyl)dodecane (F12H12) (Fig.2.13) is used as the reference system. We altered the molecular architecture by introducing different groups between the two blocks. An aromatic core that connects the fluorinated and the alkyl

chain was introduced (F12-phenyl-H12) (Fig.2.15) and then added two oxygens (F12-O-phenyl-O-H12) (Fig.2.16). Subsequently, we shift from linear to a star-like structure by creating a derivative with four side chains connected to an extended aromatic core (bis(F11H1-core-H12)) (Fig.2.14). Also, two extra branched like structures were used, Didodecyl-2,7-bis(perfluorododecyl)-9H-fluoren (Fig.2.17) and 9,9-Didodecyl-9H-fluoren (Fig.2.18). The synthesis and 3D characterization of Perfluoro(dodecyl)dodecane (F12H12) and bis(3-(1-perfluoroundecylmethoxy)-5-dodecyloxyphenyl) ethyne (Fig. 2.14) has been reported by Rabolt *et al.* (1984) and Clark *et al.* (2009), respectively. The synthesis of the rest semifluorinated alkanes has been described in the thesis of Stangenberg (2013).

For the investigation of the photo-responsive films of SFAs at the water-air interface an azobenzene group is inserted between the fluorocarbon and hydrocarbon chains. The thermodynamic, optical, structural, and dynamic properties of the semifluorinated azobenzene derivatives (E)-1-(4-octylphenyl)-2-(4-(perfluorooctyl)phenyl)diazene) and the analogous (E)-1,2-bis(4-octylphenyl)diazene (Fig.2.19) that were used in this study, have been reported by Stangenberg *et al.* (2014). The photo-induced isomerization from the extended coplanar (trans) to the twisted (cis) forms of azobenzene derivatives is accompanied by a significant change in the dipole moment from 0 to 3 D. In general, the presence of fluorine in perfluoroalkyl chains can enhance the self-assembly because the fluorines are bulkier and are much more rigid than their hydrogenated analogous. In the present work, dilute solutions of the above SFAs were made in mutually good solvent n-hexane and were spread on the Langmuir trough drop-wise using a 50 μ L syringe. After the spreading the layer was left at rest for 15 minutes for the evaporation of the n-hexane.

Table 2.1: Characteristics of semifluorinated alkanes.

Short name	Chemical name	M _w (gmol ⁻¹)
F12H12	Perfluoro(dodecyl)dodecane	788.4
F12-phenyl-H12	1-Dodecyl-4-(perfluorododecyl)benzol	864.5
F12-O-phenyl-O-H12	1-(Dodecyloxy)-4-((perfluorododecyl)oxy)benzol	896.5
bis(F11H1-core-H12)	bis(3-(1- perfluoroundecylmethoxy)-5-dodecyloxyphenyl)ethyne	1743.1
2F12-core-2H12	Didodecyl-2,7-bis(perfluordodecyl)-9H-fluoren	1739.0
2H-core-2H12	9,9-Didodecyl-9H-fluoren	502.9
F8-azo-H8	(E)-1-(4-octylphenyl)- 2-(4-(perfluorooctyl)phenyl)diazene	712.5
H8-azo-H8	(E)-1,2-bis(4-octylphenyl)diazene	406.6

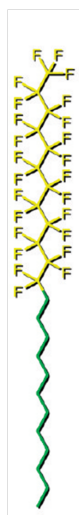


Figure 2.13: Perfluoro(dodecyl)dodecane (F12H12). The cartoon illustration is taken from Clark *et al.* (2009).

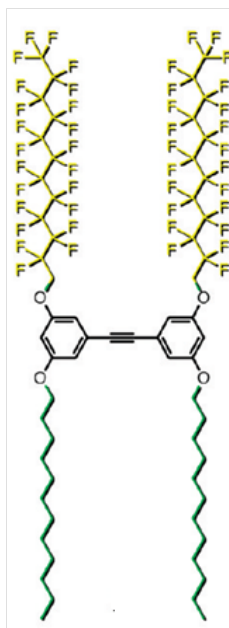


Figure 2.14: Biphasic DPA, bis(3-(1-perfluoroundecylmethoxy)-5-dodecyloxyphenyl)ethyne (bis(F11H1-core-H12)). The cartoon illustration is taken from Clark *et al.* (2009).

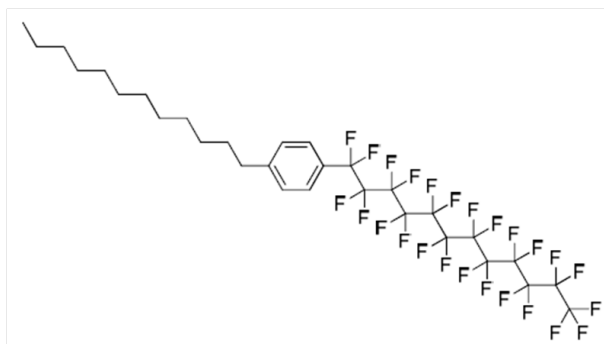


Figure 2.15: 1-Dodecyl-4-(perfluorododecyl)benzol (F12-phenyl-H12). This cartoon illustration has been taken from Stangenberg (2013).

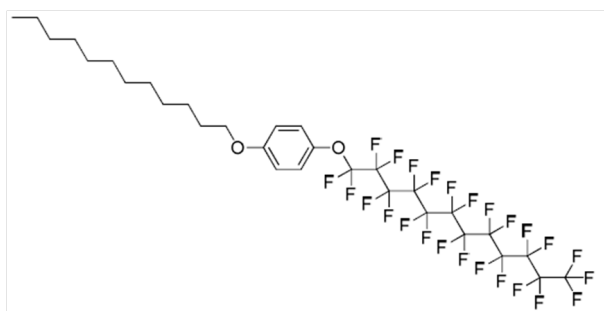


Figure 2.16: 1-(Dodecyloxy)-4-((perfluorododecyl)oxy)benzol (F12-O-phenyl-O-H12). This cartoon illustration has been taken from Stangenberg (2013).

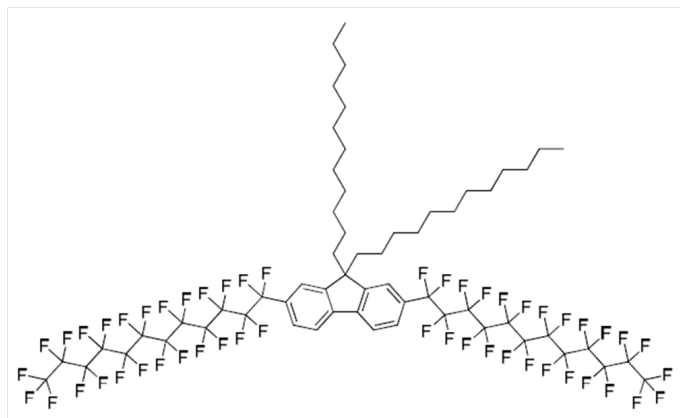


Figure 2.17: Didodecyl-2,7-bis(perfluorododecyl)-9H-fluorene (2F12-core-H12). This cartoon illustration has been taken from Stangenberg (2013).

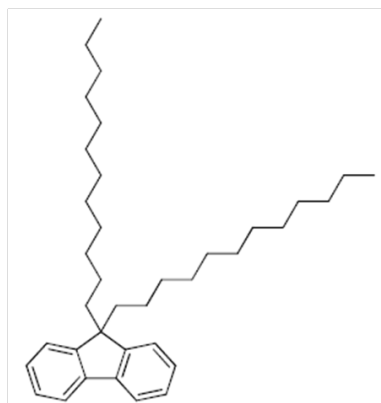


Figure 2.18: 9,9-Didodecyl-9H-fluorene (2H-core-2H12). This cartoon illustration has been taken from Stangenberg (2013).

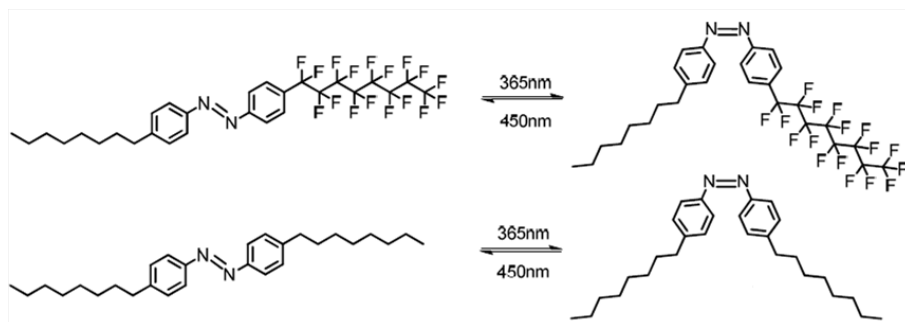


Figure 2.19: Azobenzene derivatives (E)-1-(4-octylphenyl)-2-(4-(perfluorooctyl)phenyl)diazene (F8-azo-H8) and (E)-1,2-bis(4-octylphenyl)diazene (H8-azo-H8). This cartoon illustration has been taken from Stangenberg (2013).

Diblocks and triblocks of Polyethyleneoxide (PEO) - Polydimethylsiloxane (PDMS)

As we aim to form stable monolayers able to form supramolecular structures, we chose to study PEO-PDMS polymers at the air-water interface because of their amphiphilic nature: they are polymers constituted by a hydrophilic part (PEO) and a hydrophobic part (PDMS). Such polymers can be considered a model system for amphiphilic molecules as both of the subchains can be well characterized on the monomer scale. In Figure 2.20 the general formula of PEO-PDMS is shown where the number of PEO units is denoted with m and the number of PDMS units with n . These materials are provided by the group of Moshe Gottlieb of Ben-Gurion University of the Negev Beer-Sheva (Israel).

For the synthesis of the triblocks, a commercial α, ω dimethylsilane poly (dimethyl siloxane) (SiH-PDMS) of the desired length was used, while for the diblock copolymers the α -dimethylsilane- ω -trimethylsiloxane PDMS was synthesized using anionically catalyzed ring opening polymerization. Further details of the synthesis have been reported in Laufer (2013). The copolymer structures and their molecular weights that were used in this thesis are presented in Table 2.2. The materials were dissolved in 2,2,4-Trimethylpentane with concentration of 1 mg/ml. The depositions at the water-air interface were performed drop-wise by spreading the solution using a 50 μ L syringe and each measurement was performed after a waiting time of 15 minutes, that is necessary for the evaporation of the volatile solvent.

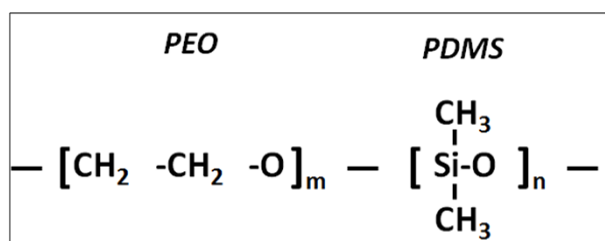


Figure 2.20: Diblocks of Polyethyleneoxide (PEO)- Polydimethylsiloxane (PDMS).

Table 2.2: Characteristics of PEO-PDMS diblock and triblock copolymers.

Name	Formula	$M_w(\text{gmol}^{-1})$
E6D30	$(\text{PEO})_6(\text{PDMS})_{30}$	1600
E10D30	$(\text{PEO})_{10}(\text{PDMS})_{30}$	2400
E11D80	$(\text{PEO})_{11}(\text{PDMS})_{80}$	5800
E6D80E6	$(\text{PEO})_6(\text{PDMS})_{80}(\text{PEO})_6$	6300
E10D80E10	$(\text{PEO})_{10}(\text{PDMS})_{80}(\text{PEO})_{10}$	7900
E40D80	$(\text{PEO})_{40}(\text{PDMS})_{80}$	7200

Poly(methyl methacrylate) (PMMA)

Poly(methyl methacrylate) (PMMA) polymer was obtained by PSS (Mainz, Germany) that was synthesized anionically. Figure 2.21 depicts the general formula of PMMA. Its weight-average molar mass was 270000 g/mol and its polydispersity index $\text{PDI} = M_w/M_n$ of 1.04. The spreading solution was made by using chloroform with at a concentration of 1 mg/ml. The surface depositions of the PMMA at the water-air interface were performed drop-wise by spreading the solution using a 50 μL syringe. The polymer layer was left at rest for about 15 minutes for the evaporation of the solvent. Finally, fast compression and expansion cycles were performed to ensure a homogeneous layer.

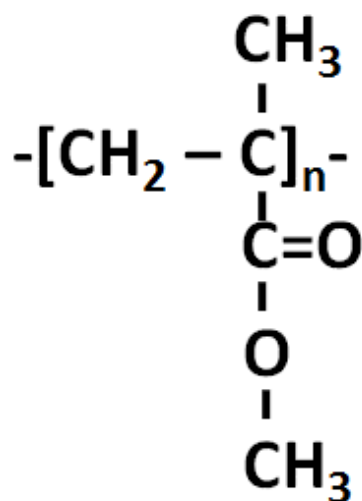


Figure 2.21: Poly(methyl methacrylate) (PMMA).

CHAPTER 3

SEMIFLUORINATED ALKANES AT THE WATER-AIR INTERFACE: EFFECTS OF MOLECULAR ARCHITECTURE ON STRUCTURE AND RHEOLOGY

3.1 State of the art

Semifluorinated alkanes (SFAs), with general formula ($C_nF_{2n+1}C_mH_{2m+1}$), consist of linked fluorocarbon and hydrocarbon segments that are bound covalently. These molecules have shown particular behaviour in the bulk and at interfaces. Because of the hydrophobic nature of both their fluorocarbon and hydrocarbon chains they are known to form Langmuir monolayers at the water-air interface. Significant contribution in the research of SFAs has been achieved by Gaines (1991), Broniatowski and Dynarowicz-Latka (2008), Bardin *et al.* (2011), Krafft (2012a), Krafft (2012b) and Krafft and Riess (2009). The unique properties of these materials have been reviewed extensively. The fluorine atoms are more electronegative comparing to the hydrogen atoms and they form a dense electron shield around the carbon backbone. On the contrary, the fluorine atoms have smaller polarizability than the hydrogens. Consequently, the cohesive energy between the fluorinated molecules is smaller than the energy between the hydrogens. Also the surface tension of fluorocarbons is about 10 mNm^{-1} , lower than the hydrocarbon one.

Regarding other physico-chemical characteristics of SFAs, as it is shown in Figure 3.1, they are amphisteric molecules with approximate cross sections of 0.20 nm^2 for the CH-chain (planar/*all-trans* conformation) and 0.30 nm^2 for the CF-chain (helical conformation), because the fluorine atoms have a greater atomic radius than hydrogen. Also semifluorinated alkanes have an amphidynamic character, one moiety is stiff and rod-like, while the other is flexible and the junction of the CF_2-CH_2 bond carries a strong dipole moment.

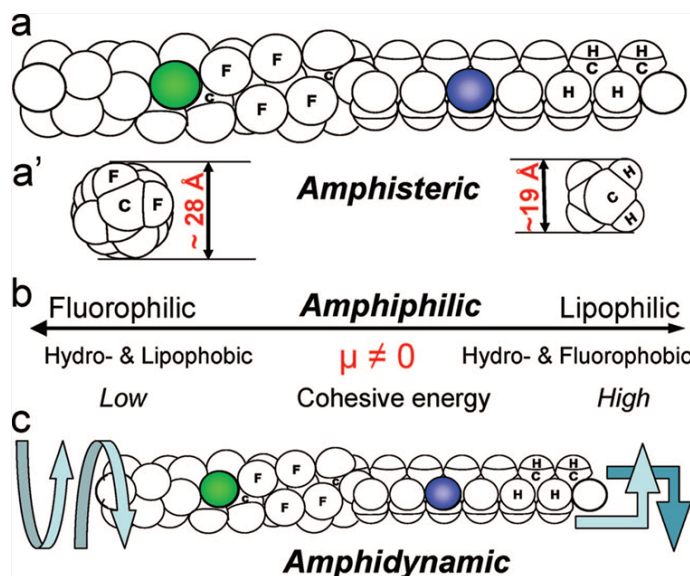


Figure 3.1: Linear F_nH_m diblocks are (a) Amphisteric, (b) Amphiphilic, and (c) Amphidynamic. The image has been taken from Krafft and Riess (2009).

There is a richness of solid state packing structures of SFAs that has been reported by Nunez *et al.* (2008), Gottwald *et al.* (2002), Stangenberg *et al.* (2013) and Clark *et al.* (2009). More specifically, the biphasic F12H12 undergoes two first-order transitions that are strongly pressure dependent with two transition temperatures. At low temperatures, a solid phase is made by fluorocarbon bilayer lamella, with an interdigitated hydrocarbon layer. At higher temperatures, an isotropic liquid phase has been reported. The thermal behaviour and phase structure of geminidiblock semifluorinated alkanes (tetrablocks) in the bulk state has been explored by Lux *et al.* (2013). In the low temperature range a disorder plastic rotator phase has been reported made by rows of ribbons, in this regime, melt of the alkyl chains takes place, while at a higher temperature, where melt of the fluorocarbons is observed there is a lamellar phase kind of smectic-B and at even higher temperatures an isotropic liquid phase. SFAs blended with amphiphilic block copolymers confined at the water-air interface have been used in order to create surfaces with low energy. Gamboa *et al.* (2002) mixed semifluorinated alkanes with PS-PEO and produced honeycomb structures with periodicity of 40 nm. The volumetric and viscosity behaviour of perfluoroalkylalkane solutions has been studied extensively at different pressures and temperatures via a combination of numerical simulations and experiments (Duarte *et al.* (2013), Morgado *et al.* (2011a), Morgado *et al.* (2011b), Morgado *et al.* (2007a), Morgado *et al.* (2007b)).

At the water-air interface the self-assemblies and the hierarchical ordering of

F12H12 have been studied by de Viguerie *et al.* (2011). In Figure 3.2 the proposed model for the hierarchical formation of F12H12 into surface micelles has been reported by de Viguerie *et al.* (2011). It has been shown in the literature that SFAs self assemble into hexagonal lattices comprising of disk-like micelles (Lux *et al.* (2013), Bardin *et al.* (2010), Maaloum *et al.* (2002), Zhang *et al.* (2005), Eftaiha and Paige (2012)). Brewster angle microscopy (BAM) and Scanning Force Microscopy (SFM) have been used in order to characterize the morphology of SFA Langmuir monolayers at the water-air interface, and their structural behaviour onto silicon substrates. The formation of the disk-like micelles was studied theoretically by Semenov *et al.* (2006) who attributed their formation to liquid/liquid (rather than liquid/gas) phase separation in the Langmuir monolayer. The micelles were shown to form islands of the higher-density phase with roughly vertical orientation of F_nH_m molecules (fluorocarbon blocks extending toward the air and hydrocarbon blocks toward water), whereas the matrix was the lower-density phase with the F_nH_m diblocks lying nearly parallel to the water surface. The micelles and the hexagonal structures were stabilized by electrostatic repulsive interactions, which were due to the vertical dipole moments of the CF_2-CH_2 bonds in the vertical phase. These interactions suppressed the micelle size polydispersity. These findings were supported by recent experimental studies with symmetric and asymmetric SFAs using neutron reflectivity, SFM and rheology (de Viguerie *et al.* (2011), Klein *et al.* (2011)).

SFAs find several applications in medicine and biomedical field (Kissa (New York, 2001), Riess (2002), Krafft (2001)) mostly as liquid drug carrier systems for topical ocular drug delivery, for the detached retina therapy (Riess (2009)) and as blood-substitutes (Meinert and Knoblich (1993)). It has been shown that emulsions with semi-fluorinated alkanes dissolve about the same amount of oxygen as emulsions with perfluorocarbons. The stability of these emulsions depends on the nature of the alkyl and the perfluoroalkyl chain and, according to toxicity tests against human carcinoma cells, semifluorinated alkanes with alkyl chains are harmless in the examined range from C_6 to C_{10} (Meinert and Knoblich (1993)). Moreover, the use of synthetic DPPC/F8H2 diblock compositions is thought to be a new approach to lung surfactant therapy (Krafft and Riess (2009)).

From the above literature review it is evident that semifluorinated alkanes are good candidates to form ordered films at the water-air interface with potentially tunable

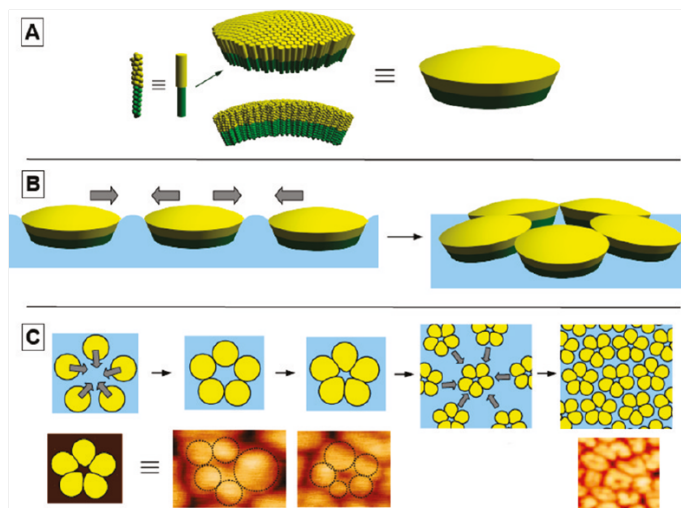


Figure 3.2: Model proposed for the hierarchical formation of the surface micelles. (A) Self-assembly of the amphiphobic F12H12 molecules in parallel orientation with the F-block pointing up to the air into curved primary aggregates with ca. 10 nm diameter. (B) Secondary assembly (side view) of the primary aggregates into clusters of the surface micelles driven by capillary forces. (C) Surface micelle aggregation (top view) with slight deformation of the primary aggregates and comparison to the SFM image details. The image has been taken from de Viguerie *et al.* (2011).

properties. What remains a challenge is tailoring the film properties varying molecular characteristics and for developing appropriate protocols. Drawing analogies from the bulk, it is known that macromolecular architecture can affect the rheology of polymers. The intrinsic structuring capability of SFAs is anticipated to be a novel building motif in supramolecular architectures, and the challenge is to link it to their stability and properties. Hence, exploiting the structure-rheology interplay as a function of molecular architecture of SFA at the air-water interface is of fundamental importance and represents the goal of this work.

The goal of this chapter is to connect the architecture of the SFAs with their organization at the air-water interface and the associated rheological properties. We aim specifically at: (i) relating the chemical composition at the molecular scale with the interfacial stability and rheology of the layers at air-water interface. (ii) investigating and discriminating via packing models the molecular orientation and layer thickness under different surface pressures for different architectures. Starting with a reference system, Perfluoro(dodecyl)dodecane (F12H12) (Fig.2.13) a phenyl is introduced that connects the fluorinated and the alkyl chain (F12-phenyl-H12) (Fig.2.15) and then two oxygens are introduced (F12-O-phenyl-O-H12) (Fig.2.16). Then we are shifting from linear to

a star-like structure by creating a derivative with four side chains connected to an extended aromatic core (bis(F11H1-core-H12)) (Fig.2.14). Finally, two extra branched structures are used, (2F12-core-2H12) (Fig.2.17) and (2H-core-H12) (Fig.2.18). In this chapter the experimental results are presented as follows: In the first section of this chapter we present the results of F12H12 and bis(F11H1-core-H12) are presented. In the second section we compare the results of F12-phenyl-H12 and F12-O-phenyl-O-H12 and in the third section the experimental results of 2F12-core-2H12 and 2H-core-H12.

3.2 Perfluoro(dodecyl)dodecane (F12H12) and bis(3-(1-perfluoroundecylmethoxy) -5-dodecyloxyphenyl)ethyne (bis(F11H1-core-H12))

3.2.1 Surface Pressure Area Isotherms

Figure 3.3 depicts the surface pressure/area isotherms of F12H12 and bis(F11H1-core-H12) at 20 °C. We compare the surface area requirement of each molecular system i.e., the area that the molecules occupy when they are packed, this can be probed when the surface pressure increases, estimated knowing the dimensions of the molecules from de Viguerie *et al.* (2011). More specifically, the F-block has length of 17Å and area of 28 Å². The length of the H-block is 16.5Å and its area 20Å². We also investigate the possible transitions and collapse of the layer where the slope of the isotherm changes. The reference system F12H12 shows the first increase of surface pressure at surface area of 33-34 Å² conforming to the neutron reflectivity and SFM results, which point to the predominantly vertical orientation of the molecules. In the case of bis(F11H1-core-H12) the surface pressure starts to increase for A= 95Å² /molecule, which is substantially larger (3 times larger) than F12H12. This surface area requirement corresponds to the calculated surface area of the extended aromatic core indicating the vertical orientation of the molecules. By compressing the layer the surface pressure increases until 38 mN m⁻¹ which corresponds to a molecular area of 42Å². Moreover, there is a kink observed at A= 53 Å²/molecule which corresponds to a probable collapse (changing in the packing order).

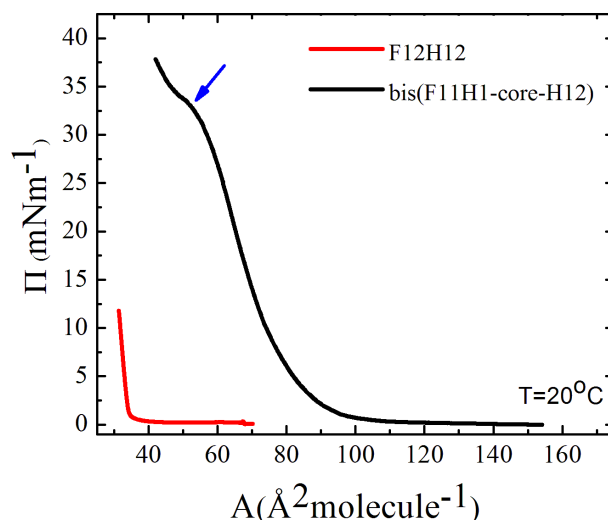


Figure 3.3: Surface pressure/area isotherms of F12H12 and bis(F11H1-core-H12) monolayers at the water-air interface at 20°C. The arrow shows a change in the packing order of the monolayer.

Compression-expansion cycles were performed in order to check the possible hysteresis (irreversibility) of the layers, and hence their stability. Isotherms which during expansion, following compression, exhibit no hysteresis are considered to be reversible hereafter. Furthermore, when the layer is reversible the recompression (second compression-expansion cycle) follows the same path like the first cycle. Reversibility tests of the reference system F12H12 have been previously performed by Klein *et al.* (2011). Figure 3.4 depicts the compression-expansion cycles of F12H12 and bis(F11H1-core-H12) measured at 20 °C. From the compression-expansion cycles of bis(F11H1-core-H12) layer we observe that the path of the first expansion doesn't overlap with the path of compression, yielding a fully irreversible compression-expansion layer deformation. Moreover, during the second compression- expansion cycle the monolayer doesn't recover, following the path of the first expansion. In this case the irreversible layer deformation is the presence of a stronger attraction between the molecules causing the formation of three dimensional aggregates at the air-water interface.

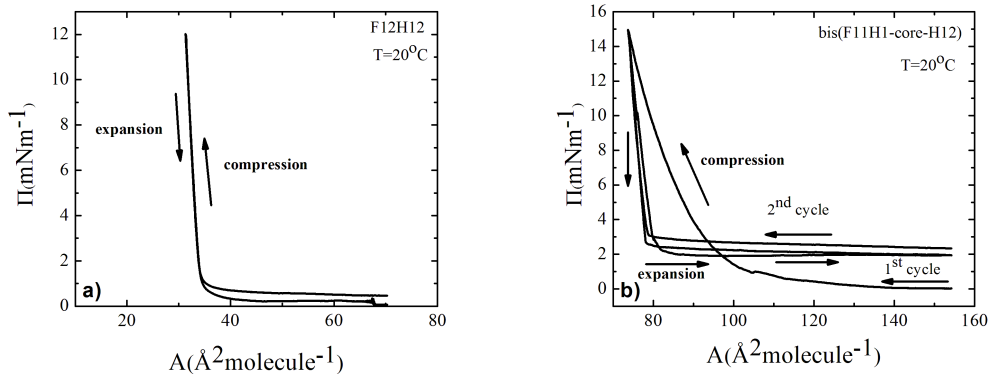


Figure 3.4: Compression- expansion cycles of a) F12H12 and b) bis(F11H1-core-H12) at 20°C.

3.2.2 Interfacial Rheology

The role of preshear was investigated for F12H12 and bis(F11H1-core-H12) using the double wall ring rheometer. We used a preshear protocol at $\omega=10$ rad/s for 2 min. A dynamic time sweep (DTS) test was performed to F12H12 at $\omega=0.65$ rad/s and $\gamma=1\%$. As it is shown in Figure 3.5a the data are scattered and after a period of 60 min they could not equilibrate, an indication of the destroyed monolayer of the micelles. A completely different behaviour was observed for the layer of bis(F11H1-core-H12). After preshear ($\omega=10$ rad/s for 2 min) a DTS was performed at $\omega=0.65$ rad/s and $\gamma=0.1\%$. In Figure 3.5b we notice the difference of G' and G'' without preshear and after preshear. In this case bis(F11H1-core-H12) layer shows that after preshear its molecules are reorganised in a way that equilibrate the layer. Taking into account this finding, all the next rheological measurements of bis(F11H1-core-H12) were performed after the layer was presheared, while in the case of the of F12H12 no preshear took place before the rheological measurements.

The linear viscoelasticity data of F12H12 have been studied by Klein *et al.* (2011) who used the magnetic rod interfacial stress rheometer. Complementary measurements were performed here in order to determine the extent of the linear viscoelastic regime. We performed dynamic strain sweep tests in the range $1\% < \gamma < 100\%$ at 0.65 rad/s. Figure 3.6a depicts the storage modulus (G') and the loss modulus (G'') as a function of strain amplitude (γ) for five different surface pressures at 0.65 rad/s, for F12H12 layers. By increasing the surface pressure the storage modulus is increased corresponding to an increase of the elasticity of the layer. Figure 3.6b depicts the corresponding stress

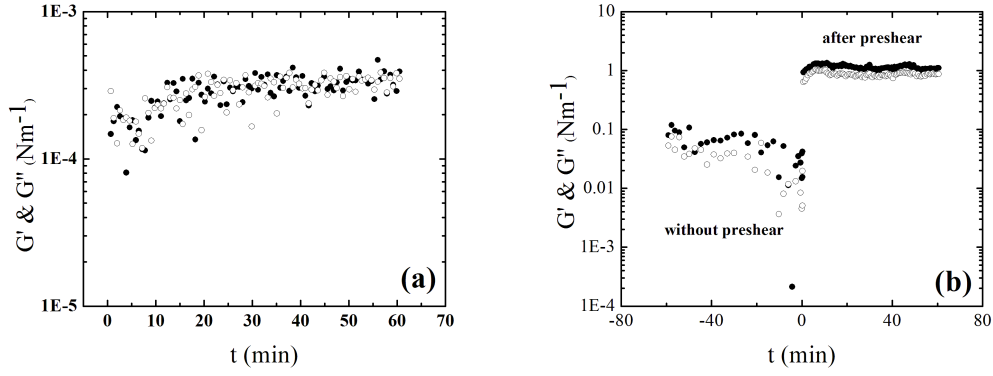


Figure 3.5: The role of preshear at $\omega=10$ rad/s for 2 min for a) F12H12 and b) bis(F11H1-core-H12) at $\Pi=2$ mNm $^{-1}$. G' (closed symbols) G'' (open symbols).

versus strain for all surface pressures examined.

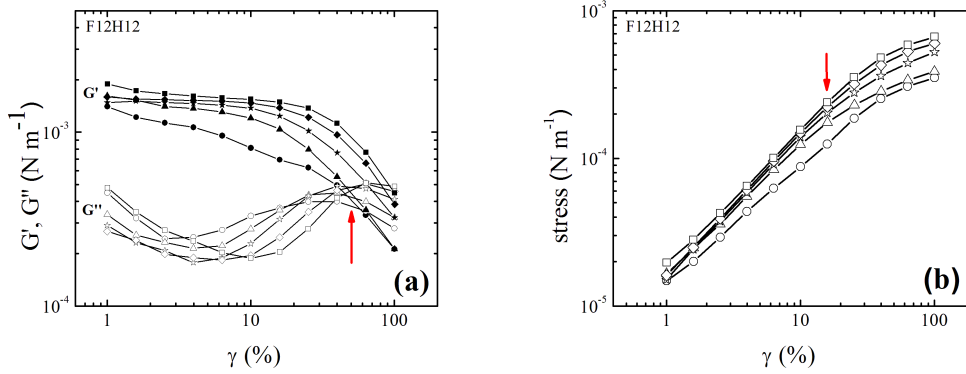


Figure 3.6: Nonlinear viscoelasticity of F12H12 at $\omega=0.65$ rad/s. a) Dynamic Strain Sweep measurement at five different surface pressures, 2 mNm $^{-1}$ (circles), 4 mNm $^{-1}$ (triangles), 6 mNm $^{-1}$ (stars), 8 mNm $^{-1}$ (diamonds) and 10 mNm $^{-1}$ (squares). The red arrow indicates the crossover. b) Interfacial stress as a function of strain. The red arrow indicates the onset of a nonlinear stress-strain relation. G' (closed symbols) and G'' (open symbols).

The dynamic frequency sweep measurement of bis(F11H1-core-H12) was performed in the Double Wall Ring (DWR) (Figure 3.7) in five different surface pressures at strain amplitude $\gamma=0.1\%$. With increasing surface pressure, both surface elastic and viscous moduli increase. For all surface pressures $G' \gg G''$, we show a signature of solid like behaviour with a frequency independent G' .

In Figure 3.8a the dynamic strain sweep measurements of bis(F11H1-core-H12) are presented for five different surface pressures at $\omega=0.65$ rad/s and the red vertical arrow indicates the crossover. Figure 3.8b shows the stress as function of strain am-

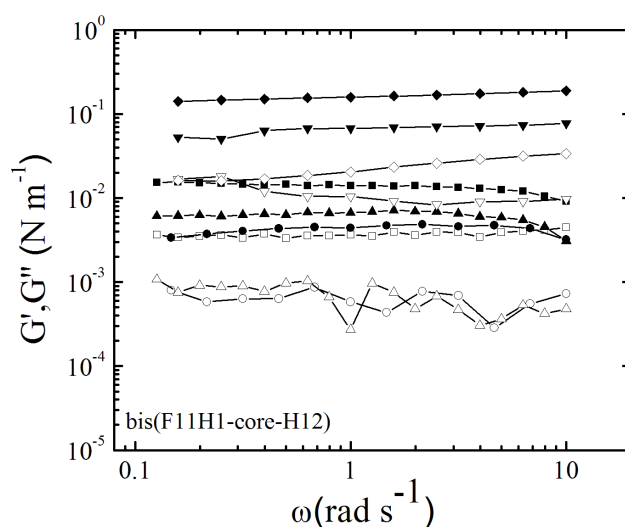


Figure 3.7: a) Interfacial frequency sweep data of bis(F11H1-core-H12) at $\gamma=0.1$ % and 20°C. The surface moduli are depicted as functions of frequency at 4 mNm^{-1} (circles), 8 mNm^{-1} (triangles), 10 mNm^{-1} (squares), 20 mNm^{-1} (inverted triangles) and 22 mNm^{-1} (diamonds) measured on Double Wall Ring (DWR). G' (closed symbols) G'' (open symbols).

plitude for all the range of surface pressures that were examined. In this figure the onset of nonlinear stress-strain relation is indicated with a red vertical arrow. Comparing the two systems at $\Pi=4\text{mNm}^{-1}$, the layer of bis(F11H1-core-H12) (crossover at $\gamma=1.3\%$) breaks (i.e, yields) at a strain amplitude roughly 40 times smaller than in the F12H12 case (crossover at $\gamma=54\%$). While by increasing the surface pressure to 10 mNm^{-1} the layer of bis(F11H1-core-H12) (crossover at $\gamma=1.2\%$) breaks at a strain amplitude roughly 78 times smaller than in F12H12 (crossover at $\gamma=93.4\%$). These observations suggest that the interfacial film of bis(F11H1-core-H12) tolane derivative exhibits a more "brittle" viscoelastic behaviour in comparison to the respective film from F12H12. Figure 3.9 depicts the surface storage modulus (G') as a function of surface pressure for F12H12 and bis(F11H1-core-H12) with their power laws of 0.75 and 2 respectively. While in Figure 3.10 the maximum linear strain amplitude and stress has been plotted as a function of surface pressure for F12H12 and bis(F11H1-core-H12). The extent of the linear regime has been determined locating its upper bound where G' changes by more than 10 % with respect to its constant value.

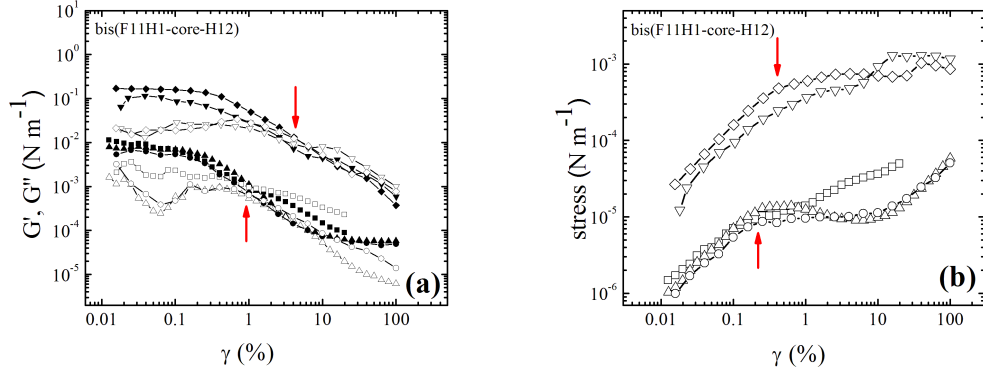


Figure 3.8: Nonlinear viscoelasticity of bis(F11H1-core-H12) at $\omega=0.65$ rad/s. a) Dynamic Strain Sweep measurement at five different surface pressures, 4 mNm^{-1} (circles), 8 mNm^{-1} (triangles), 10 mNm^{-1} (squares), 20 mNm^{-1} (inverted triangles) and 22 mNm^{-1} (diamonds). b) Interfacial Stress as a function of strain. G' (closed symbols) and G'' (open symbols).

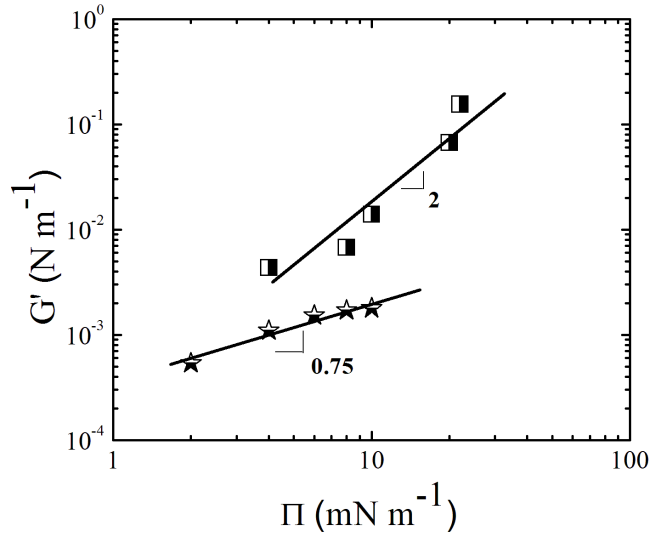


Figure 3.9: Comparison of storage modulus vs surface pressure of bis(F11H1-core-H12) (square symbols) and F12H12 (stars). The error bars are included in the size of the symbols.

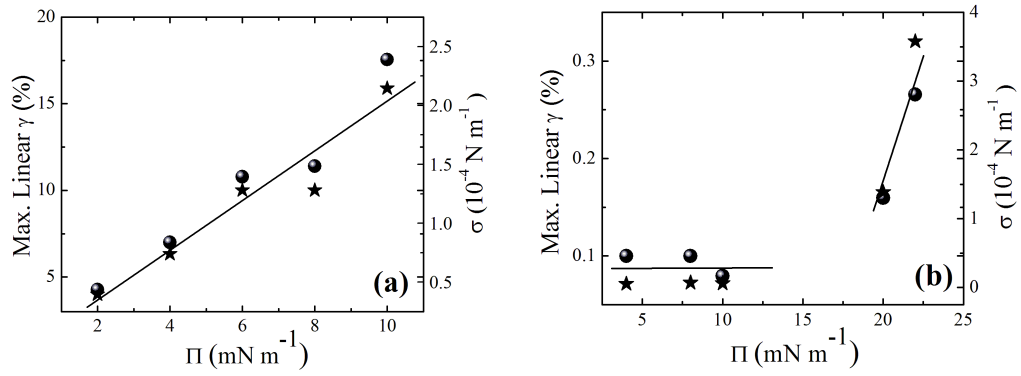


Figure 3.10: Maximum linear strain amplitude (spherical symbols) and stress (star symbols) versus surface pressure for a) F12H12 and b) bis(F11H1-core-H12).

3.2.3 Neutron Reflectivity

We performed neutron reflectivity measurements at the water-air interface in order to investigate the organization of the different SFAs. We have assessed available packing models by variation of the structural parameters such as number of layers, layer thickness, scattering length density and surface roughness for each layer. Also the layers were transferred onto silicon substrates to obtain data at larger q vectors and potentially discriminate F-up or H-up structures in the neutron reflectivity experiments. The neutron reflectivity intensity depends on the scattering length density profile. During the analysis of the reflectivity spectra we try to discriminate the different possible packing models of the systems. These models include either vertical or parallel molecular packing where the F-blocks or the H-blocks are pointing towards the air or towards the aqueous phase. The fitting is attempted by variation of the following structural parameters: (i) Number of layers: Depending on the specific packing model. (ii) Scattering length density (SLD): It is calculated according to www.ncnr.nist.gov, knowing the bulk density of the molecules. (iii) Layer thickness: In case of vertical orientation models, a stretched molecule has extended length of $d(FnHm) = 1.3 + 1.265n + 2.58 \text{ \AA}$. Also from the molecular area of the isotherms and SFM we can extract information about the thickness. (iv) Roughness: Initially we find the roughness of the D₂O by fitting the reflectivity data of D₂O without the layer, this gives a value of 5 \AA . The scattering length density profile ($\rho(z)$) is calculated for a set of N layers using the Parratt32 formalism

(equation 3.1) (Parratt (1954)):

$$\rho(z) = \rho_0 + \sum_{i=1}^{N+1} \frac{\rho_i - \rho_{i-1}}{2} (1 + \operatorname{erf}(\frac{z - z_i}{\sqrt{2}\sigma_i})) \quad (3.1)$$

with

$$z_i = \sum_{j=1}^i t_j \quad (3.2)$$

where t is the thickness, ρ_i is the real part of the scattering length density and σ_i is the roughness of each layer. In this equation the model assumes a linear superposition of error functions each of which describes the density profile of each layer.

In Figure 3.11 the obtained reflectivity data and the scattering length density for the bis(F11H1-core-H12) system at the air/D₂O interface are represented. Three different surface pressures were examined, where no significant difference was observed in the normalized intensity. In the different surface pressures the neutron reflectivity intensity was within the statistical limit of the data. In the case of bis(F11H1-core-H12) at the air/D₂O interface a reflectivity minimum is observed in all surface pressures at $q=0.07\text{\AA}^{-1}$. From the literature (de Viguerie *et al.* (2011)) we know the approximate dimensions of the fully extended molecule of F12H12. The length of the CF-block is 17\AA , of the CH-block is 16.5\AA and the approximate size of the phenyl ring is around 6\AA . From the isotherm we got a molecular area of 95\AA^2 , an indication of vertical orientation of the molecules. From the neutron reflectivity data, a good fit could be obtained by choice of 2 layers, where the first one is on contact with the aqueous phase and consists of the CH-block and the core with $\text{SLD}=1.47 \times 10^{-7}\text{\AA}^{-2}$, and a second layer consisting of CF-blocks ($\text{SLD}=4.6 \times 10^{-6}\text{\AA}^{-2}$). A model where the CF-blocks are pointing towards the air is proposed. Alternative models were tried in order to obtain a good fit: with CF-blocks in contact with the water or "lying flat". In all these alternative cases the convergence between the experimental data and the fits was not good. In the suggested 2-layer model the thickness of the CF-block is 6.3\AA and the thickness of the CH-block (with the core) is 29.7\AA . In Figure 3.12 the obtained reflectivity data and the proposed model for the bis(F11H1-core-H12) at the air/silicon interface are shown. The proposed packing model of the air/silicon interface was again found to be the CF-blocks pointing towards the air. However, in this case the thickness of the CF-block layer is the same

with the CH-block layer ($d=23\text{\AA}$). Comparing the scattering length density profiles at $\Pi=2\text{ mN m}^{-1}$ and $\Pi=5\text{ mN m}^{-1}$ the best fit was obtained by increasing the value for the layer roughness from 6 \AA ($\Pi=2\text{ mN m}^{-1}$) to 17 \AA ($\Pi=5\text{ mN m}^{-1}$).

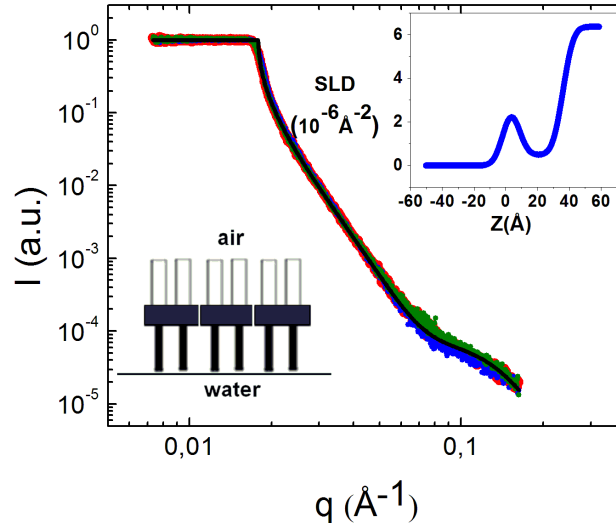


Figure 3.11: Neutron reflectivity study of bis(F11H1-core-H12). Neutron Reflectivity curve and Scattering Length Density profile (inset) at air/D₂O interface. Surface pressures: 2 mN m^{-1} (blue color), 5 mN m^{-1} (red color) and 12.8 mN m^{-1} (green color). In the figures, the normalized intensity is denoted as $I\text{ (a.u.)}$.

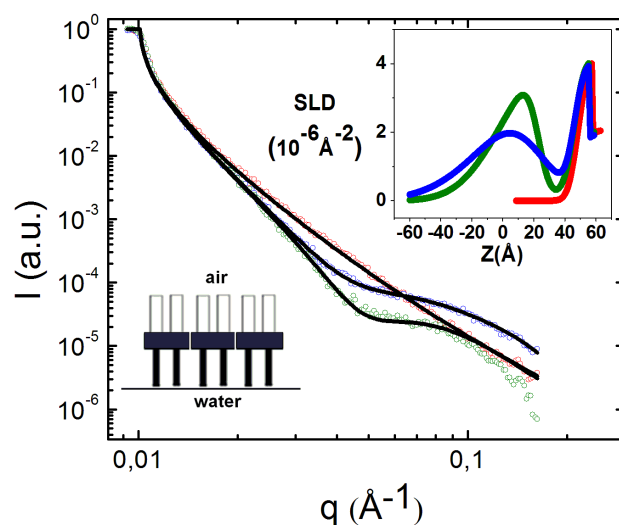


Figure 3.12: Neutron Reflectivity curve and Scattering Length Density profile (inset) of bis(F11H1-core-H12) at air/si-wafer interface. Surface pressures: 2 mNm^{-1} (blue color) and 5 mNm^{-1} (green color) and bare wafer (red color). In the figures, the normalized intensity is denoted as I (a.u.).

3.2.4 Scanning Force Microscopy

The films were transferred from the water-air interface to silicon wafer substrates as it is demonstrated in Figure 2.12. The silicon wafers were located at the bottom of the trough tilted in a slight angle on the one side. The water was pumped out carefully and the layer was deposited onto the silicon wafer. Figure 3.13 depicts the height and phase image of bis(F11H1-core-H12) film transferred at $\Pi=2 \text{ mNm}^{-1}$. Despite the low surface pressure, huge elongated aggregates are observed. While in Figure 3.14 the formation of 30 nm diameter micelles of F12H12 is presented.

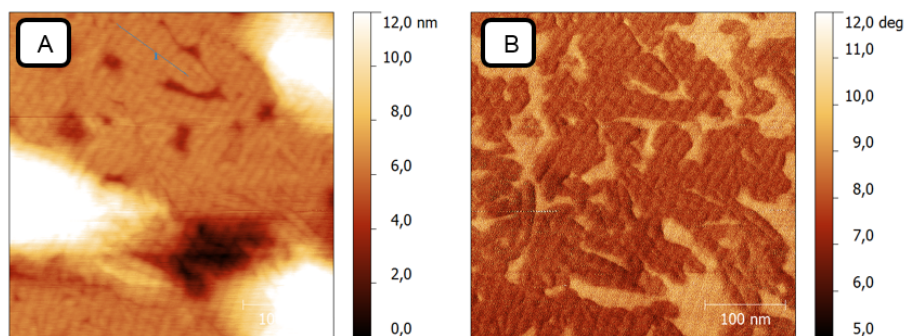


Figure 3.13: Height image (A) and phase image (B) of bis(F11H1-core-H12) transferred at $\Pi=2 \text{ mN/m}$.

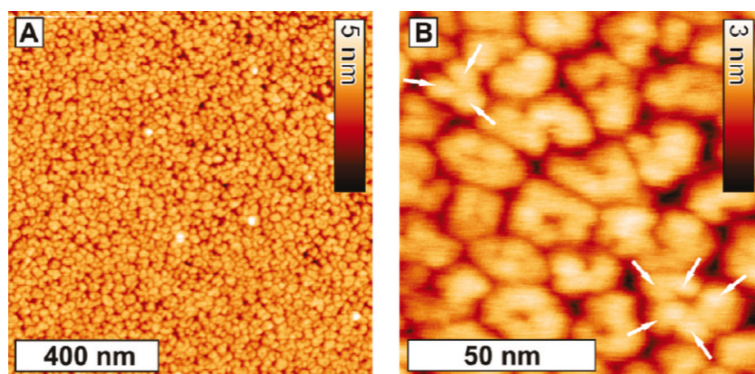


Figure 3.14: SFM topographic image of an F12H12 monolayer transferred at $\Pi=2$ mN/m. (B) Zoom-in of the topographic image. This image has been taken from de Viguerie *et al.* (2011)

3.3 1-Dodecyl-4-(perfluorododecyl)benzol (F12-phenyl-H12) and 1-(Dodecyloxy)-4-((perfluorododecyl)oxy)benzol (F12-O-phenyl-O-H12)

3.3.1 Surface Pressure Area Isotherms

Figure 3.15 presents the surface pressure-area isotherms of F12-phenyl-H12 and F12-O-phenyl-O-H12 at $T=20^{\circ}\text{C}$. The F12-phenyl-H12 derivative shows an increase of the surface pressure at 68\AA^2 (almost two times larger than F12H12) which increases until 35 mN m^{-1} corresponding to an area of $50\text{ \AA}^2/\text{molecule}$. The increase of surface pressure for F12-O-phenyl-O-H12 occurs at a molecular area 4 times larger ($130\text{ \AA}^2/\text{molecule}$) in comparison with F12H12 and it increases until 15 mN m^{-1} which corresponds to a molecular area of 37 \AA^2 . The large surface requirement could be an indication of the "lying flat" molecular packing of the system knowing the dimensions of the molecule from de Viguerie *et al.* (2011). Also a kink was observed at $A=113\text{ \AA}^2/\text{molecule}$ which we attribute to a possible transition during the compression.

Figure 3.16a shows three compression-expansion cycles of F12-phenyl-H12. During the expansion of the layer the initial value returns to zero while during recompression the shape of the isotherm recovers. In the case of F12-O-phenyl-O-H12 (Fig. 3.16b) it forms a fully reversible layer under compression-expansion cycles, reproducing the transition at $\Pi=4\text{ mNm}^{-1}$. Different volumes ($40\mu\text{l}$, $60\mu\text{l}$ and $200\mu\text{l}$) of the solutions of F12-O-phenyl-O-H12 were spread at the water-air interface in order to obtain the

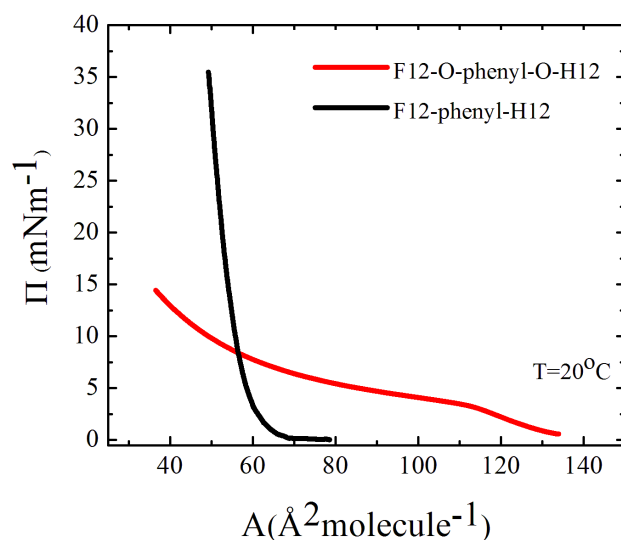


Figure 3.15: Surface pressure/area isotherms of F12-phenyl-H12 and F12-O-phenyl-O-H12 monolayers at the water-air interface at 20°C.

whole surface pressure/ area isotherm of F12-O-phenyl-O-H12. As it is shown in Figure 3.17a, the isotherms seem to have good overlapping, an indication of their reversible character that was described before. In Figure 3.17b the temperature effect on the layer stability and the possible phase transition was investigated, at $T=5^{\circ}\text{C}$ and $T=10^{\circ}\text{C}$ for F12-O-phenyl-O-H12 system and the results showed similar behaviour to those measured at $T=20^{\circ}\text{C}$.

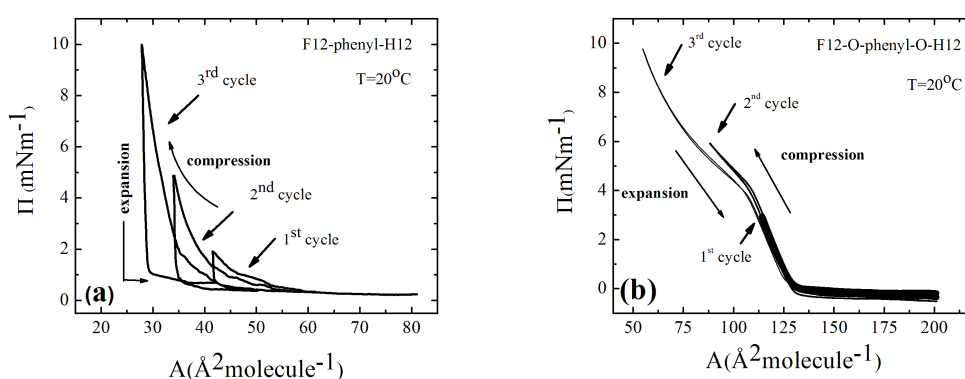


Figure 3.16: Compression- expansion cycles of a) F12-phenyl-H12 and b) F12-O-phenyl-O-H12 at 20°C.

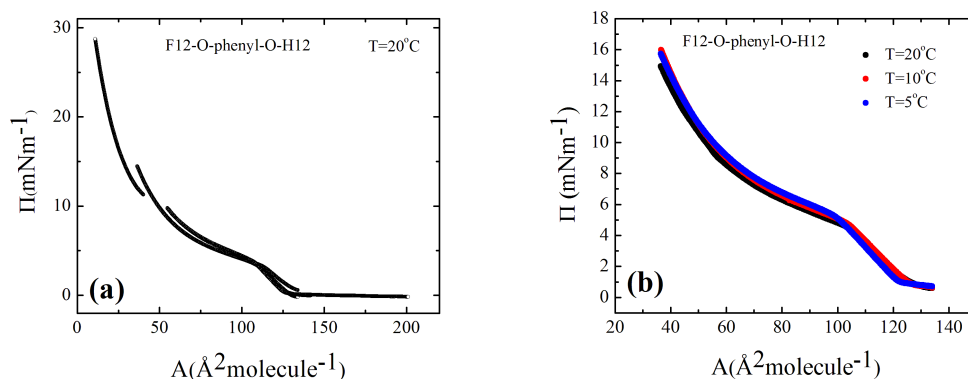


Figure 3.17: a) Whole surface pressure/area isotherm of F12-O-phenyl-O-H12 at 20°C and b) surface pressure/area isotherms of F12-O-phenyl-O-H12 at different temperatures.

3.3.2 Interfacial Rheology

The linear viscoelastic behaviour of F12-phenyl-H12 and F12-O-phenyl-O-H12 was investigated using the magnetic rod interfacial rheometer. Dynamic frequency sweep measurements were performed in the range $0.1\text{rad/s} < \omega < 10\text{rad/s}$ at strain amplitude $\gamma=0.1\%$. Figure 3.18a and 3.18b depicts the storage modulus (G') and the loss modulus (G'') as a function of frequency (ω) of F12-phenyl-H12 and F12-O-phenyl-O-H12 layers respectively. The interfacial moduli in both cases are close to the moduli of the water as they were measured in the same conditions, showing that the monolayers of F12-phenyl-H12 and F12-O-phenyl-O-H12 are very weak. It's worth noting here that the positive value of G' at low frequency is due to the compliance of the setup and must not be attributed to any physical properties of the layer. As it is shown in Figure 3.19, plotting the interfacial viscosity versus frequency of F12-phenyl-H12, F12-O-phenyl-O-H12 and water it is confirmed that the interfacial viscosity of the layers is close to the water's viscosity.

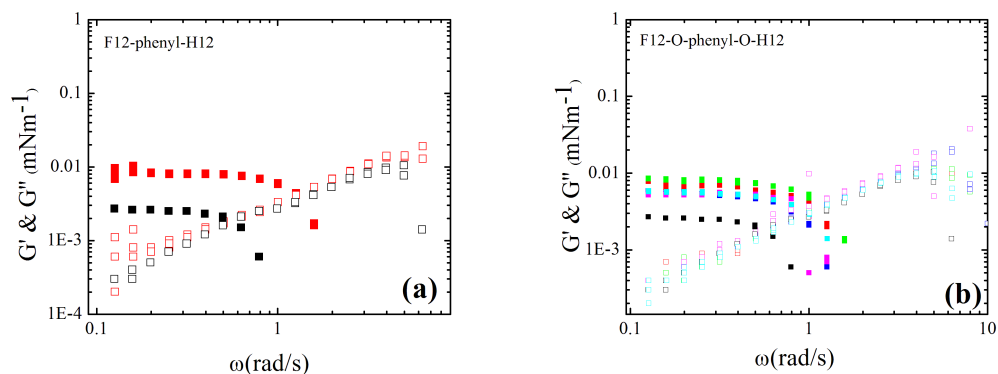


Figure 3.18: a) Interfacial frequency sweep data of F12-phenyl-H12 (red symbols) at 2 mN/m and water (black symbols). b) Interfacial frequency sweep data of F12-O-phenyl-O-H12 as functions of frequency at 2 mN/m (red symbols), 4 mN/m (green symbols), 8 mN/m (magenta symbols), 15 mN/m (cyan symbols) and water (black symbols). G' (closed symbols), G'' (open symbols)

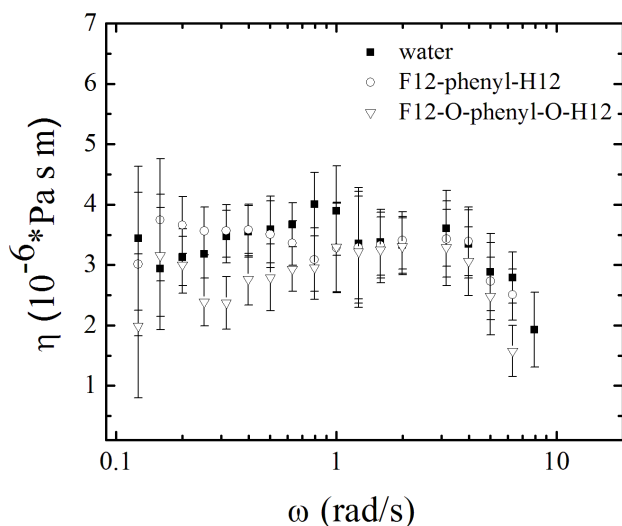


Figure 3.19: Interfacial viscosity of F12-phenyl-H12, F12-O-phenyl-O-H12 and water as a functions of frequency at 20°C.

Creep experiments were performed and the time-dependent compliance ($J(t)$) data were converted to frequency-dependent moduli in order to obtain information at lower frequencies. The compliance was measured in the linear regime by imposing a low stress and the conversion was performed by Fourier transformation. In this work we used approximate numerical formulas according to Schwarzl (1969) where the advantage of these formulas is that they do not involve any integration of the measured functions. In order to investigate the rheological behaviour of F12-O-phenyl-O-H12 we performed a creep measurement at shear stress of 10^{-4} Pa m and surface pressure of 2 mNm^{-1} (Figure 3.20a reports the creep compliance) in a stress-controlled rheometer using the Double Wall Ring (DWR) fixture. This measurement was necessary in order to properly characterize the viscoelasticity of the interface over a wide frequency range, given that the dynamic frequency sweep measurements (typically at frequencies not exceeding 100 rad/s) suggested a very weak interface (liquid-like). Figure 3.20b depicts the extracted interfacial dynamic moduli from the creep measurement, the storage (G') and the loss (G'') modulus as a function of frequency. In the frequency range $10^{-3} \text{ rad s}^{-1} \leq \omega \leq 14 \text{ rad s}^{-1}$ the layer shows a viscoelastic fluid behaviour with $G'' > G'$, $G'' \sim \omega$ and $G' \sim \omega^2$. We note that at frequencies below 10 rad/s the liquid-like layer has moduli G' lower than those of the other films of F12H12 and bis(F11H1-core-H12) but G'' significantly larger. On the other hand, at higher frequencies the solid-like response is characterized by a large G' . Finally, it is worth to be mentioned that the absence of experimental data in the interval between 0.1-10 rad/s of the compliance is attributed to failure of the rheometer during the measurement.

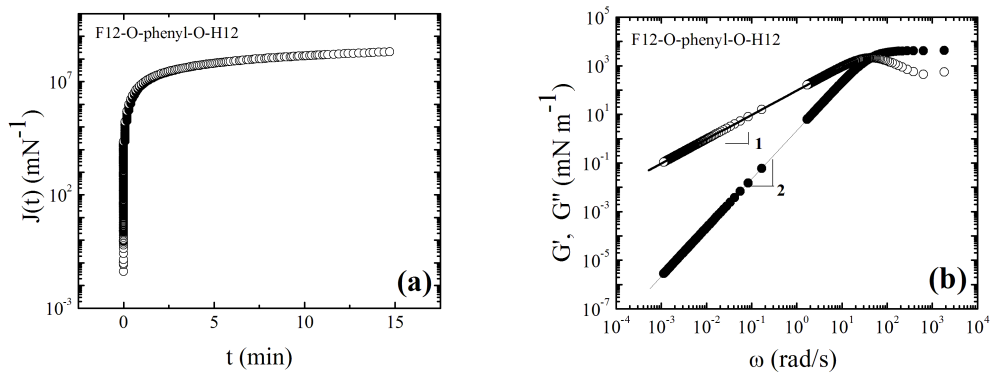


Figure 3.20: Interfacial rheology of F12-O-phenyl-O-H12. a) Creep test using the Double Wall Ring (DWR) fixture. The shear stress applied was 10^{-4} Pa m. b) Dynamic moduli, i.e. G' (open circles) and G'' (closed circles), extracted from creep data with their linear fits (solid lines).

3.3.3 Neutron Reflectivity

Figure 3.21 depicts the reflectivity data and the proposed model for the F12-phenyl-H12 derivative at the air/D₂O interface. In this case from the isotherm information we were not able to estimate the vertical or parallel orientation of the molecules because the molecular area was 68 Å². From SFM the thickness could be estimated approximately to 8-10 Å. From neutron reflectivity, at the examined surface pressure (2 mNm⁻¹), the spectra fit well to one layer model with unknown orientation (also called mixed) with a thickness of 15 Å.

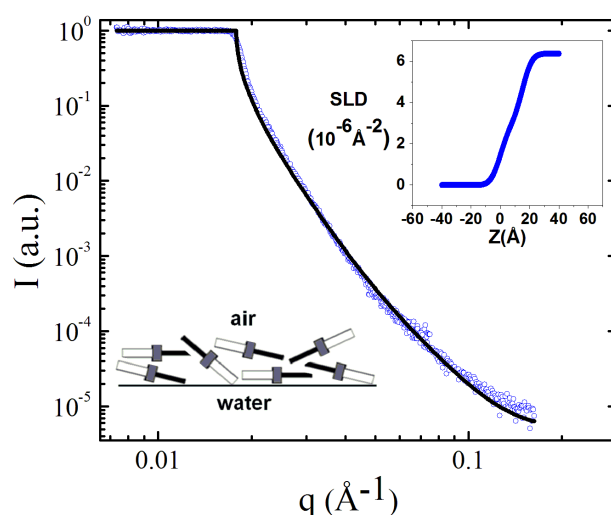


Figure 3.21: Neutron reflectivity curve and Scattering Length Density profile (inset) of F12-phenyl-H12 at the air/D₂O interface. Surface pressures: 2 mNm⁻¹ (blue color) and the fit (black line). The normalized intensity is denoted as I (a.u.).

In Figure 3.22 the obtained neutron reflectivity data with the proposed model of F12-O-phenyl-O-H12 are shown. From the surface pressure isotherm of F12-O-phenyl-O-H12 we obtained a molecular area of 130 Å², a clear indication of a "lying flat" orientation of the molecules. During the neutron reflectivity experiments the surface pressure was set at 2 mNm⁻¹ and 20 mNm⁻¹. A reasonable fit was obtained by assuming a two-layer model of total thickness 10 Å (5 Å per each) with SLD = 1.48 × 10⁻⁶ Å⁻². Consequently, in both surface pressures a parallel packing model is suggested, with thickness of 10 Å. From the scattering length density profile we can distinguish the increased roughness from 5 Å (Π = 2 mNm⁻¹) to 50 Å (Π = 20 mNm⁻¹). Taking into account the presence of two oxygen groups we could propose a parallel packing model

with an interdigitating structure of the chains as it is shown in the inset of Figure 3.22, where the oxygen atoms tend to be on contact with the aqueous phase. In Appendix the non-convergent fits of the perpendicular orientation models are presented.

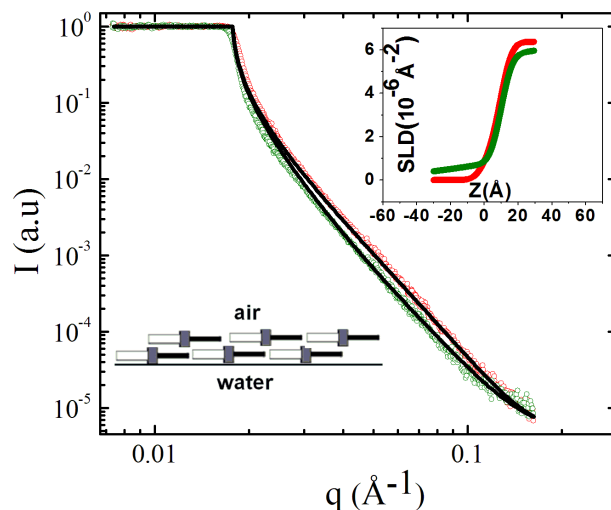


Figure 3.22: Neutron reflectivity curve and Scattering Length Density profile (inset) of F12-O-phenyl-O-H12 at the air/D₂O interface. Surface pressures: 2 mNm⁻¹ (red color) and 20 mNm⁻¹ (green color). The fits are presented with the black lines. The normalized intensity is denoted as I (a.u.).

3.3.4 Scanning Force Microscopy

Figure 3.23 depicts the phase image of F12-phenyl-H12 film transferred at 2 mNm⁻¹. The possible film thickness is maybe around 8~10 Å, which is less than the thickness from the neutron reflectivity measurements. Figures 3.24 and 3.25 depict the height and phase images of F12-O-phenyl-O-H12 molecules transferred before ($\Pi=2$ mNm⁻¹) and after ($\Pi=13$ mNm⁻¹) the phase transition at $\Pi=4$ mNm⁻¹ respectively. At 2 mNm⁻¹ (before phase transition), F12-O-phenyl-O-H12 molecules form bright islands on silicon wafer from height images. From the phase images, we can clearly notice that there are different phases inside the bright island and they are surrounded by the bright structures. For F12-O-phenyl-O-H12 films transferred at 13 mNm⁻¹ (after phase transition), it forms homogeneous, dense structures and the peak-to-peak roughness is around 3 Å. From neutron reflectivity at 2 mNm⁻¹ and 13 mNm⁻¹ the layer thickness is 10~11 Å and the roughness 5 Å. The roughness is in accordance with the SFM at low surface pressures.

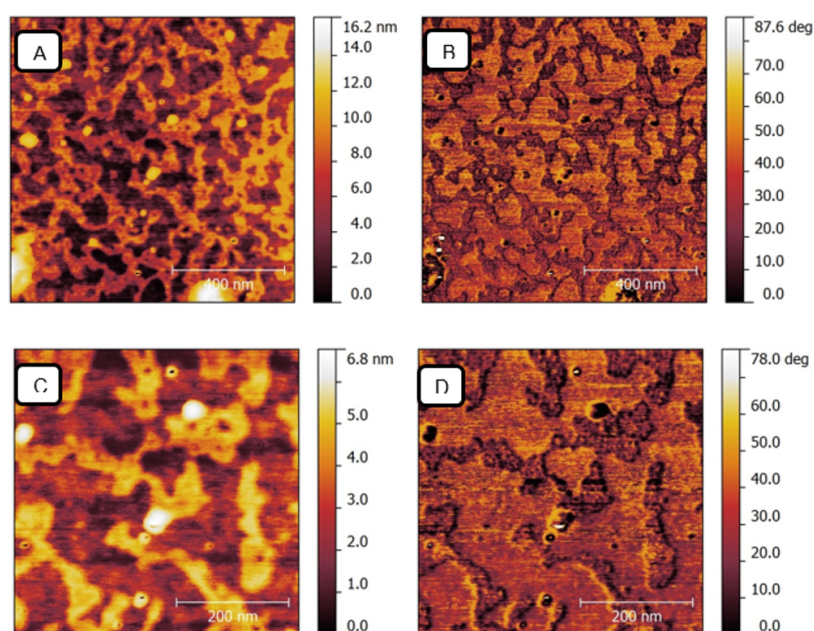


Figure 3.23: Height images (A, C) and phase images (B, D) of F12-phenyl-H12 film transferred at 2 mNm^{-1} . Images C and D are recorded at higher magnification.

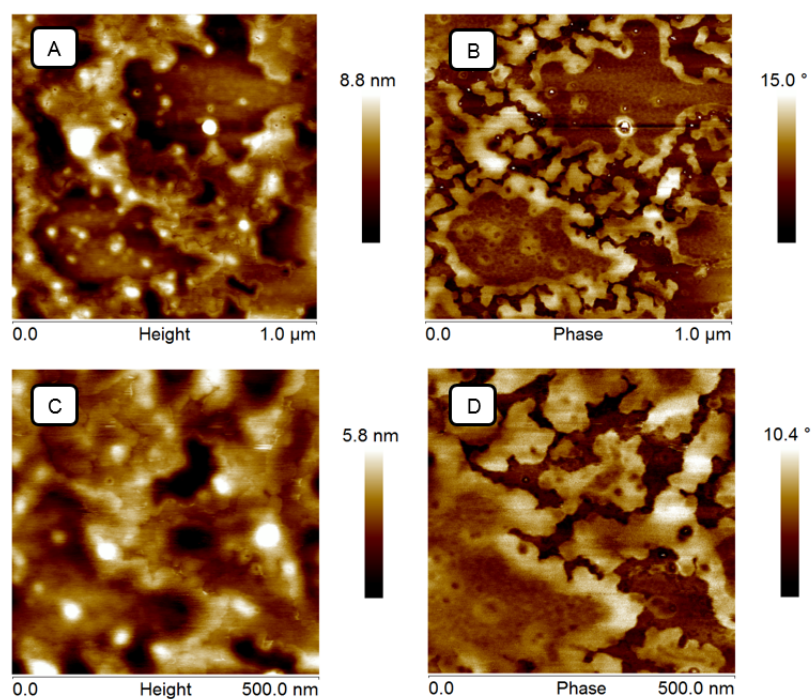


Figure 3.24: Height images (A, C) and phase images (B, D) of F12-O-phenyl-O-H12 film transferred at 2 mNm^{-1} . Images C and D are recorded at higher magnification.

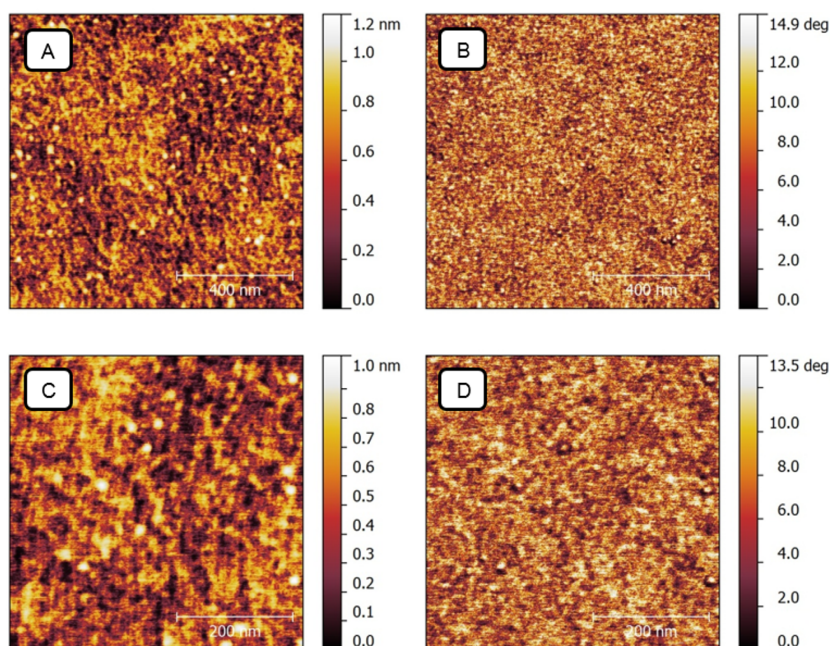


Figure 3.25: Height images (A, C) and phase images (B, D) of F12-O-phenyl-O-H12 film transferred at 13 mNm^{-1} . Images C and D are recorded at higher magnification.

3.4 Didodecyl-2,7-bis(perfluordodecyl)-9H-fluoren (2F12-core-2H12) and 9,9-Didodecyl-9H-fluoren (2H-core-2H12)

3.4.1 Surface Pressure Area Isotherms

Figure 3.26 depicts two cycles of the compression-expansion surface pressure-area isotherms of 2F12-core-2H12 at 20°C . The first increase in surface pressure occurs at surface area of 50 \AA^2 indicating the vertical orientation of the molecules. By compressing the layer a phase transition occurs at molecular area of 45 \AA^2 and surface pressure 3 mN m^{-1} . The highest surface pressure of the isotherm occurs at surface area of 20 \AA^2 with corresponds to a surface pressure of 45 mN m^{-1} . During the expansion of the layer the initial value returns to zero. From the first compression/expansion cycle a hysteresis of the layer is observed: because the first expansion doesn't overlap with the path of compression. During the second compression the isotherm follows different path comparing to the first compression, an indication of the irriversivility of the layer. The path of the first expansion, second compression and second expansion of the layer follows

almost the same path, leading to the observation that three-dimensional aggregates have been formed and behave reversibly.

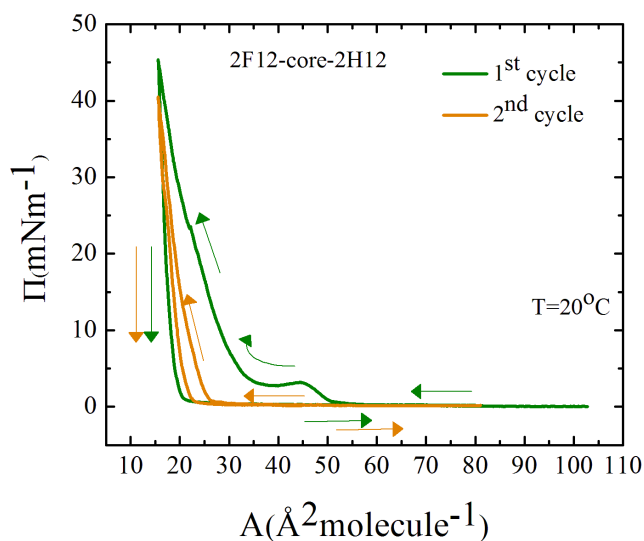


Figure 3.26: Compression- expansion cycles of 2F12-core-2H12 at 20°C.

In the case of 2H-core-2H12, as it is presented in Figure 3.27 the surface pressure starts to increase at $A = 19 \text{ Å}^2 / \text{molecule}$, which is substantially 2.6 times smaller than the molecular packing area of 2F12-core-2H12. Two compression-expansion cycles were performed where no hysteresis was observed indicating a fully reversible layer deformation of 2H-core-2H12. More specifically, during the expansion of the layer the initial value returns to zero while during recompression the shape of the isotherm fully recovers. Comparing the experimental packing molecular area at 19 Å^2 with the one that can be theoretically calculated (85 Å^2), assuming that the aromatic core is on contact with the water and the alkyl chains extend towards the air, the experimental value is 4.5 times smaller than the theoretical one. This observation supports the hypothesis that aggregates are formed rapidly as the solution is spread at air/water interface.

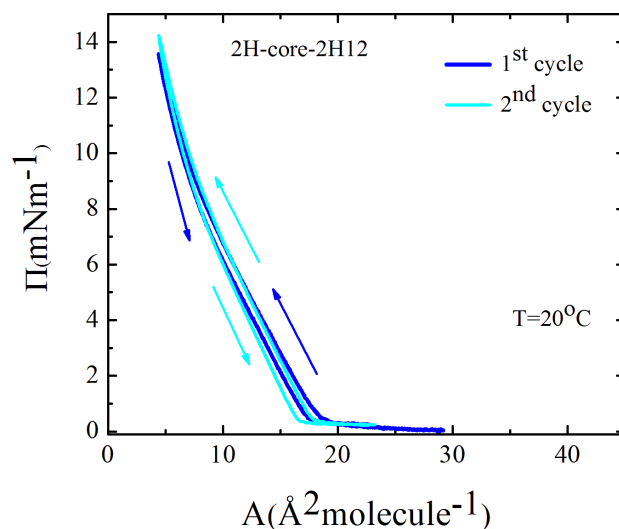


Figure 3.27: Compression- expansion cycles of 2H-core-2H12 at 20°C.

3.4.2 Interfacial Rheology

The linear viscoelasticity data of 2F12-core-2H12 are presented in Figure 3.29a. The measurement was performed on the Double Wall Ring rheometer without following the protocol of preshear because, as it is shown in Figure 3.28 the preshear damages the monolayer. Dynamic frequency sweep measurements were performed in four different surface pressures at strain amplitude $\gamma = 0.01\%$. By increasing the surface pressure, both surface elastic and viscous moduli increase. For all surface pressures $G' \gg G''$, a signature of solid like behaviour with a frequency independent G' . The dynamic moduli are two orders of magnitude higher compared to F12H12 and one order of magnitude higher in comparison with bis(F11H1-core-H12) at the same surface pressures. Consequently, the layers of 2F12-core-2H12 show the stiffest behaviour of all SFAs systems that were investigated in this thesis. Interestingly, even at surface pressure of 0 mNm^{-1} the storage modulus has relatively very high values ($G' = 20 \text{ mNm}^{-1}$ at $\omega = 0.1 \text{ rad/s}$). As it was shown in Figure 3.26, at surface pressure 3 mNm^{-1} a phase transition was observed. Consistently with this finding, at the same surface pressure, the surface moduli were decreased.

In order to determine the extend of the linear viscoelastic regime we performed Dynamic Strain Sweep tests with the DWR in the range of $0.01\% < \gamma(\text{strain amplitude}) < 100\%$ at 0.65 rad/s . Figure 3.29b shows the storage modulus (G') and the loss modulus (G'')

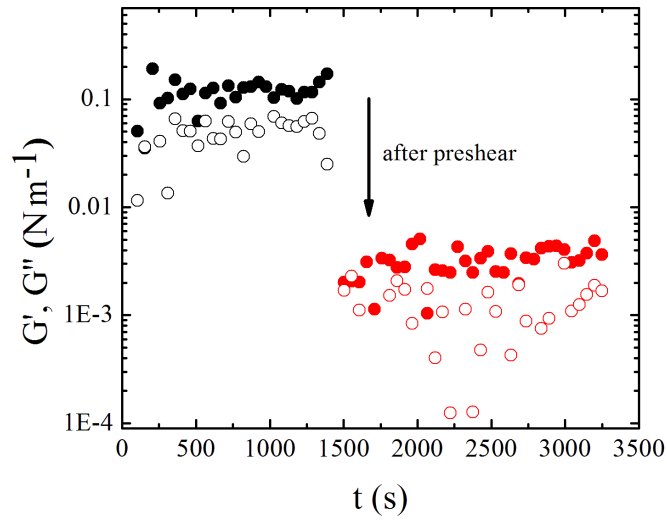


Figure 3.28: The role of preshear at $\omega=10$ rad/s for 2 min for 2F12-core-2H12. G' (closed symbols) G'' (open symbols).

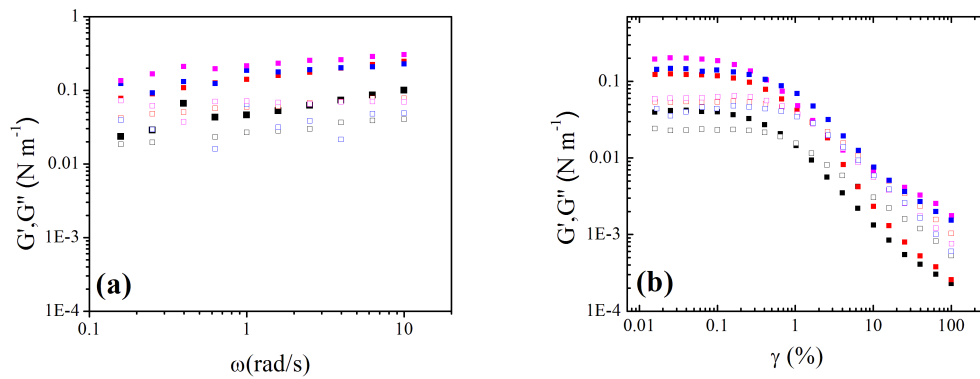


Figure 3.29: a) Interfacial frequency sweep data of 2F12-core-2H12 at 20°C. The surface moduli are depicted as functions of frequency at 0 mNm^{-1} (black colour), 1 mNm^{-1} (red colour), 2 mNm^{-1} (magenta colour), 3 mNm^{-1} (blue colour) measured on Double Wall Ring (DWR). b) Dynamic Strain Sweep measurement of 2F12-core-2H12 at four different surface pressures, 0 mNm^{-1} (black colour), 1 mNm^{-1} (red colour), 2 mNm^{-1} (magenta colour), 3 mNm^{-1} (blue colour) measured on Double Wall Ring (DWR). G' (closed symbols) G'' (open symbols).

as a function of strain amplitude (γ) for four different surface pressures at 0.65 rad/s. In all the surface pressures the maximum linear strain amplitude reaches the value of $\gamma=0.1$ %. These observations suggest that the interfacial film of 2F12-core-2H12 exhibits brittle-like viscoelastic response similar with the layers of bis(F11H1-core-H12).

The interfacial rheology measurements of 2H-core-2H12 were performed with the bi-conical fixture. The linear viscoelastic behaviour of 2H-core-2H12 is presented in Figure 3.30a. Dynamic frequency sweep measurements were performed in the range $0.1\text{rad/s} < \omega < 10\text{rad/s}$ at strain amplitudes $\gamma=0.01$ % and $\gamma=0.1$ %. The interfacial moduli in both cases are scattered showing a behaviour close to water with very weak signal. In Figure 3.30b the dynamic strain sweep measurement of 2H-core-2H12 is presented at $\omega=0.65$ rad/s showing a liquid-like response. The same measurement was performed with the magnetic rod interfacial stress rheometer and the signals were close to the water ones (similar with Fig. 3.18).

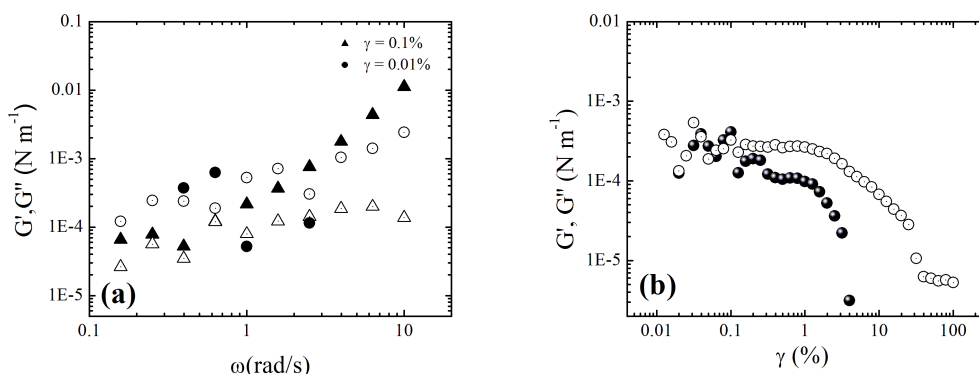


Figure 3.30: a) Interfacial rheology of 2H-core-2H12 measured on the bi-conical fixture at surface pressure 12 mNm^{-1} . a) Dynamic Frequency Sweep measurement at strain amplitude $\gamma=0.01$ % and $\gamma=0.1$ % and b) Dynamic Strain Sweep measurement at $\omega=0.65$ rad/s. G' (closed symbols) G'' (open symbols).

3.4.3 Neutron Reflectivity

In Figure 3.31 the obtained reflectivity data and the scattering length density for the 2F12-core-2H12 system at the air/D₂O interface are presented. The measurement was performed at surface pressure 2 mNm^{-1} . A reflectivity minimum is observed at $q=0.09 \text{ \AA}^{-1}$. From the literature we know the approximate dimensions of the fully extended molecule of F12H12 (de Viguerie *et al.* (2011)). Taking into account the dif-

ferent possible packing models by varying the structural parameters (number of layers, and for each layer, layer thickness, scattering length density and surface roughness) the scattering density profile was calculated. For each case, we fix the following parameters: number of layers and the scattering length density and we let as a free parameter for the minimization the rest of the parameters, layer thickness and surface roughness. In the first step the layer thicknesses were fixed to the expected value and in a second step these values were left to be optimized. From the surface pressure/area isotherm we got a molecular area of 50\AA^2 , that is an indication of vertical orientation of the molecules. From the neutron reflectivity data, a good fit could be obtained assuming 2 layers. Hence, a model where the CF-blocks are pointing towards the air is proposed. The first layer is in contact with the aqueous phase and consists of the CH-block with $\text{SLD} = -3.66 \times 10^{-7} \text{\AA}^{-2}$, and a second layer consisting of CF-blocks and the aromatic core with $\text{SLD} = 4.4 \times 10^{-6} \text{\AA}^{-2}$. In the suggested 2-layer model the thickness of the CF-block (with the core) is 8.12\AA and the thickness of the CH-block is 15.1\AA . Different models were used in order to obtain a good fit, where the F-blocks were in contact with the water or the molecules were "lying flat". In these alternative cases the convergence between the experimental data and the fits were not good.

In Figure 3.32 the obtained reflectivity data and the proposed model for the 2H-core-2H12 at the air/silicon interface are shown. The proposed packing model of the air/silicon interface was found to be the CH-blocks pointing towards the air. In this case the thickness of the CH-block layer is 8.33\AA and of the layer that consists of the aromatic core is 13.65\AA . For the layer with the core the scattering length density is $\text{SLD} = 1.81 \times 10^{-6} \text{\AA}^{-2}$, and for the layer with the CH-blocks the scattering length density is $\text{SLD} = -3.66 \times 10^{-7} \text{\AA}^{-2}$.

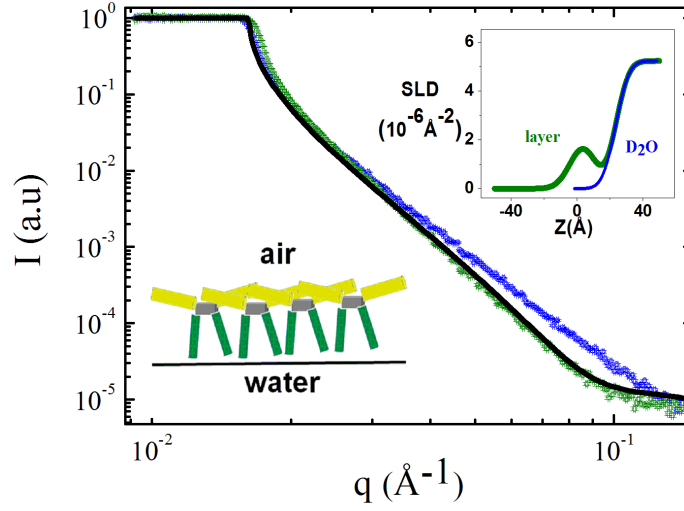


Figure 3.31: Neutron reflectivity curve and Scattering Length Density profile (inset) of 2F12-core-2H12 at the air/D₂O interface. Surface pressures: 2 mNm⁻¹(green color),the fit (black line) and D₂O reflectivity data (blue colour). The normalized intensity is denoted as I (a.u.).

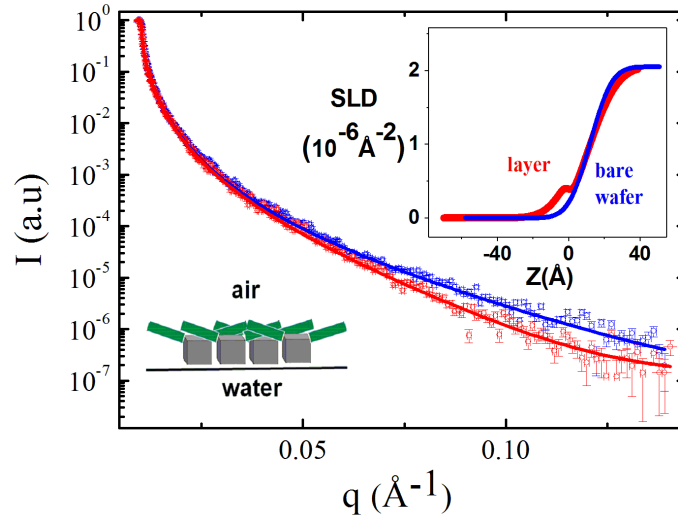


Figure 3.32: Neutron reflectivity curve and Scattering Length Density profile (inset) of 2H-core-2H12 at the air/silicon wafer interface. Surface pressures: 2 mNm⁻¹ (red color) and the fit (red line), silicon wafer reflectivity data (blue color) and its fit (blue line). The normalized intensity is denoted as I (a.u.).

3.4.4 Scanning Force Microscopy

Figure 3.33 depicts the height and phase images of 2F12-core-2H12 film transferred at $\Pi=2\text{mNm}^{-1}$. Despite the low surface pressure, the formation of dense structure is shown.

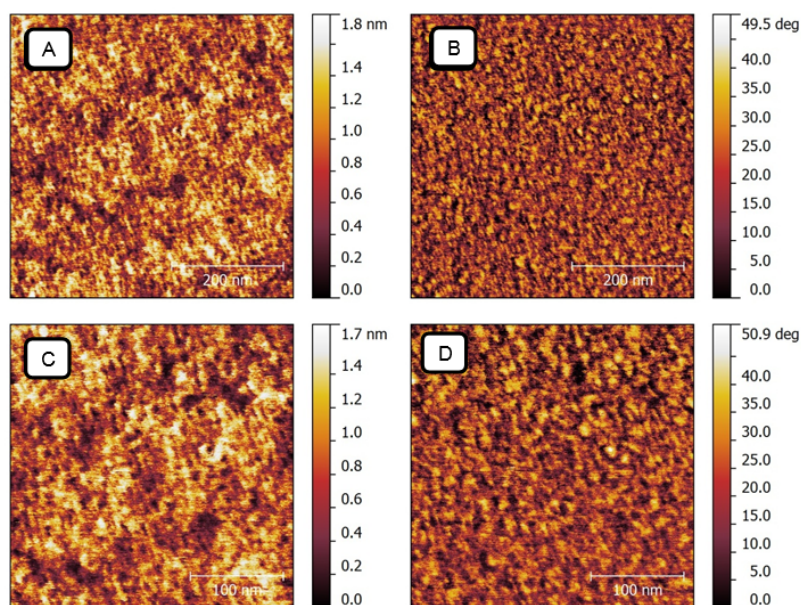


Figure 3.33: Height images (A, C) and phase images (B, D) of 2F12-core-2H12 film transferred at 2 mNm^{-1} . Images C and D are recorded at higher magnification.

3.5 Concluding remarks

The goal of this chapter was to investigate systematically the properties and stability of semifluorinated alkanes monolayers at the water-air interface, taking advantage of their synthetic ability to vary the molecular structure. Starting from a reference system perfluoro (dodecyl) dodecane (F12H12), we introduce an aromatic core between the fluorinated and alkyl chains (F12-phenyl-H12), then two oxygens (F12-O-phenyl-O-H12) and finally consider a tolane derivative with four side chains connected to an extended aromatic core bis(F11H1-core-H12), 2F12-core-2H12 and 2H-core-H12.

We used a Langmuir trough to investigate the surface pressure/area isotherms of these systems at the air-water interface. Using neutron reflectivity at the water-air interface and scanning force microscopy after transferring to silicon wafers we investigated the structure of these systems. Also we performed interfacial rheology measurements by means of the Double Wall Ring (DWR) fixture, the bi-conical fixture and the magnetic rod interfacial stress rheometer. We found that the molecular changes have profound consequences on the stability, organization and viscoelasticity of these complex fluid interfaces.

We showed that the apparent ductility of F12H12 films increases as the monolayers are brought to high surface pressures. On the other hand, the insertion of an aromatic core between the fluorinated and alkyl chains (F12-phenyl-H12) suppresses the elasticity of the system, making the film a viscoelastic liquid within the range of frequency investigated here. Moreover, a "lying-flat" configuration of the molecules characterizes the F12-phenyl-H12 films showing that the addition of the aromatic core dramatically change the minimum energy configuration of each molecule at the water-air interface with respect to their F12H12 counterparts that were found to form circular micelles. Further alteration of the structure by addition of two oxygen atoms (F12-O-phenyl-O-H12) revealed a "lying-flat" configuration with interdigitating structure of the layers, whose stability was promoted by the oxygen tendency to be exposed to water. The fluorocarbon chains of bis (F11H1-core-H12) were found to exhibit vertical conformation at the air/water interface and form rather brittle-like monolayers with high storage moduli. We hypothesize that the single-molecule conformation at the interface is responsible for the brittle failure of the films. Furthermore, 2F12-core-2H12 films exhibit solid response: they showed the largest storage modulus and the more brittle-like

behaviour, having a structure consistent with the CF-blocks pointing towards the air. Finally, its analogue system, without fluorocarbon chains 2H-core-2H12 films exhibit viscous response, supported by a structural model based on a vertical orientation of the molecules and the aromatic core in contact with the aqueous phase.

Consequently, our results indicate that the structure and viscoelasticity of semi-fluorinated alkane films are strictly ruled by the topology and chemical composition of the molecules: the modification of the chemical structure of the molecules, passing from linear to branched, led to a large variation of the film response, under shear and compression/ expansion cycles.

CHAPTER 4

RESPONSIVE FLUID INTERFACES: PROPERTIES OF PHOTO-SENSITIVE FILMS OF SEMIFLUORINATED ALKYL-AZOBENZENES AT THE WATER-AIR INTERFACE

4.1 State of the art

Photo-sensitive films represent materials that can be alternated between well-defined structures by external stimulation e.g light irradiation. They are of particular interest because they possess a large interface between the different phases, since the interaction between the stimulus and the responsive material is enhanced compared to the bulk (Zhang and Li (2012)). Azobenzene-containing derivatives exhibit a reversible transformation from the stable trans to the less stable cis form. Photosensitive azobenzene-containing molecules which undergo trans-cis isomerization upon irradiation are potential candidates for various electro-optical applications (Feringa *et al.* (2000), Kumar and Neckers (1989), Xie *et al.* (1993)) and photosensitive devices (Kocer *et al.* (2005)). Also some azobenzene systems exhibit photoinduced optical anisotropy, meaning that they can become dichroic and birefringent after light irradiation with several photonic applications (Yaroshchuk *et al.* (2003)). They have been used for reversible optical data storage (Feringa *et al.* (1993)) and high density data storage films (Liu *et al.* (1990)). Ikeda *et al.* (2000) developed azobenzene liquid crystal (LCs) films that showed a nematic phase in trans-isomers and no LC phase in cis-isomers. In that study trans-cis photoisomerization of azobenzene with a laser pulse resulted in a nematic-to-isotropic phase transition with a rapid optical response of 200 microseconds. Also LB films of amphiphilic azobenzene derivatives have been used as command surfaces for macroscopic reorganization in liquid-crystal thin films (Seki *et al.* (1993)). Photosensitive materials in general have found application in pharmacotherapy (Velema *et al.* (2014))

by incorporating photoswitchable groups into the molecular structure of bioactive compounds.

Wustneck *et al.* (1999) investigated the cis-trans photoisomerization of azobenzene-containing trifluoromethoxy-substituted metacrylate copolymer monolayers at a fluid interface that were characterized with surface pressure/area isotherms and were described by a new theoretical approach taking into account a possible side chain aggregation. The monolayers were spread at the surface of a pendant drop. The authors showed that the minimum area demand per repeating unit of the trans conformation is smaller than that of the cis conformer, the aggregate tendency is higher for the trans conformers at low surface coverage and the trans/cis ratio increases during the trans restoration. Ultrathin films of two novel azobenzene-functionalized 1,3,5-triazine-4,6-dithiols were investigated by Muzikante *et al.* (2002). Switching between trans-and cis-forms was observed by measuring the surface potential by means of the Kelvin probe technique while alternating irradiation the self assembling monolayer with ultraviolet or visible light. In literature the most investigated systems are self-assembled monolayers (SAMs) of azobenzene-containing alkanethiols (Evans *et al.* (1998), Caldwell *et al.* (1995)).

Yim and Fuller (2003) studied the interfacial rheology of photosensitive monolayers using azobenzene-containing fatty acids. It was found that the trans configuration produces a well-packed film with non-Newtonian behaviour while the cis configuration produces a structureless Newtonian film that cannot be oriented by surface flows. In the study of Chevallier *et al.* (2011) the adsorption dynamics of azobenzene-based charged surfactants were investigated at the air-water interface and it was found that the cis-isomer adsorbs 10 times faster than the trans-isomer but the cis isomer desorbs 300 times faster. Hence, the surface was enriched in the trans isomer within few seconds and upon illumination with UV or blue light part of the trans interface was converted into the cis conformation leading to a rapid rise of the surface tension. Other studies support the higher surface affinity of trans-isomers and their ability to stabilize foams (Chevallier *et al.* (2012)). Shang *et al.* (2003) studied neutral surfactants containing one azobenzene group in their tail showed changes in the surface tension and the critical micellar concentration (cmc). Recently, the temperature dependence of aggregation and dynamic surface tension in a photoresponsive surfactant system at the air-water interface for the cis and trans isomers was investigated by Ciccirelli *et al.* (2007a,b). In

that study fluorescence measurements were performed in order to determine the effect of temperature on the cmc of the surfactant and it was found that the critical concentration associated with the formation of cis-dominant aggregates increases by increasing the temperature and also the cmc of the trans isomer increases when the temperature is increased, and the phenomenon is enhanced for temperatures greater than 35 °C.

Regarding the kinetics of trans-cis azobenzene-containing systems as it was studied in Langmuir-Blodgett (LB) films it was found that the isomerization follows the first order kinetics (Liu *et al.* (1992)). Few deviations from the trans to cis kinetics of the isomerization have been reported (Mita *et al.* (1989)). Kumar and Suresh (2009) studied the kinetics from trans to cis photoisomerization of the Langmuir monolayer of a mesogenic azobenzene dimer at the water-air interface finding that the trans to cis isomerization reaction shows deviation from the first-order kinetics. Such deviation was attributed to the simultaneous photoisomerization of trans isomers to form cis isomers and the reverse thermal isomerization of the metastable cis isomers to form the stable trans isomers.

As discussed in the previous chapter, semifluorinated alkanes (SFAs) containing fluorinated alkyl chains besides hydrogenated alkyl moieties constitute a specific class of materials that can organize into ordered structures due to the mutual incompatibility of the fluorinated and hydrogenated segments. Based on this structure-guiding motif they have received attention over the last years, for example for their ability to form different mesophases in the bulk (Clark *et al.* (2009), Nunez *et al.* (2008), Lee *et al.* (2009)), and stable Langmuir layers at the air-water interface via hierarchical self-assembly, despite the hydrophobicity of both fluorinated and alkane moieties (Krafft and Riess (2009), Gaines (1991), Broniatowski and Dynarowicz-Latka (2008)). The specific challenges with fluid interfaces coated with SFAs is the manipulation of their properties using external, specifically with light.

From the above it is evident that fluid interfaces decorated with azobenzene moieties exhibit interesting photo-responsive properties and are promising candidates in electro-optical thin-film applications. However, despite the work done so far, a clear link between interfacial structure and 2D-mechanical properties in such responsive materials is missing. This is especially true for systems with the ability to exhibit different levels of hierarchical self-assembly at interfaces, such as semifluorinated alkanes.

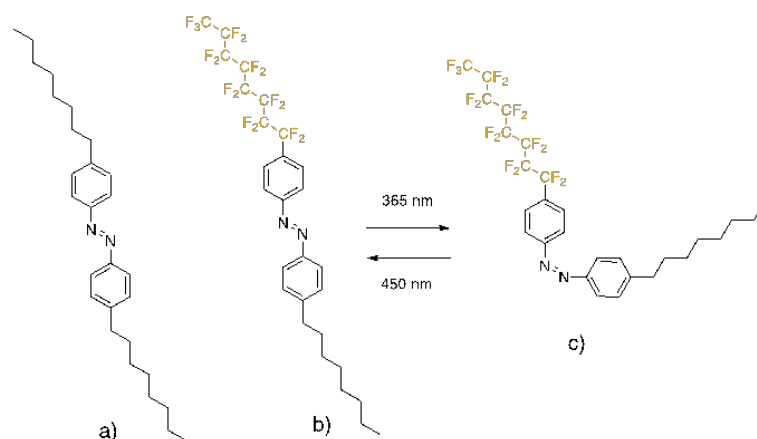


Figure 4.1: Chemical structures of (a) bis(4-octylphenyl)diazene (abbreviated H8-azo-H8), (b) [4 (heptadecafluorooctyl)phenyl](4-octylphenyl)diazene (abbreviated F8-azo-H8) and (c) light-induced change of conformation from trans to cis.

In the present study we address the above challenge by investigating the effects of UV stimulus on the interfacial properties of a novel azobenzene derivative of semi-fluorinated alkane (E)-1-(4-octylphenyl)- 2-(4-(perfluorooctyl)phenyl)diazene (in short F8-azo-H8) and its fully hydrogenated analogue (E)-1,2-bis(4-octylphenyl)diazene (abbreviated here as H8-azo-H8) (Fig.4.1). This water-insoluble molecule can be spread at the air-water interface and form Langmuir layers whose mechanical behaviour is further controlled by irradiated light. The hierarchical self-assembly is studied by means of neutron reflectivity, surface pressure isotherms and compression-expansion cycles using a Langmuir trough and interfacial rheology using the magnetic rod Interfacial Stress Rheometer (ISR). We found that UV irradiation influences dramatically the packing behaviour of the azobenzene molecules leading from vertically oriented structures to a featureless configuration without phase transition. These results are supported by interfacial rheology measurements, in which a decrease of the elastic modulus over one order of magnitude was observed under UV irradiation. The analysis of neutron reflectivity spectra allowed to draft molecular packing models considering the configuration changes under UV light.

In this chapter we present firstly the results from the surface pressure/area isotherms. In the second section we discuss the results from the interfacial rheology measurements and in the third section the neutron reflectivity.

4.2 Surface Pressure Area Isotherms

The surface pressure/area isotherms of the azobenzene containing semifluorinated alkane F8-azo-H8 under different irradiation conditions are presented in Figure 4.2. After spreading the molecules at the air-water interface in the absence of light, the azobenzene units of the SFA are predominantly in the trans configuration. The trans-to-cis configurational change of the azobenzene units upon irradiation with UV light, which can be reverted by exposure to visible light, has a direct consequence on the surface pressure isotherms. As shown in Figure 4.2, during the compression-expansion under UV irradiation (the isotherm labeled "UV") the F8-azo-H8 molecules predominantly exists in the cis configuration (about 70 percent in the photostationary equilibrium) and apparently occupy a molecular area at the onset of the pressure increase (say about 2 mN m^{-1}), which is about three times larger than that in the trans configuration (measurements performed in the absence of light, isotherm labeled "DARK"). Under UV irradiation there is a kink observed at $A = 95 \text{ \AA}^2/\text{molecule}$ which corresponds to a change in the packing order of the film. This surface area requirement under dark corresponds to the calculated surface area of the extended azobenzene core indicating the vertical orientation of the molecules. Under visible light, the situation is intermediate, as most molecules revert from the cis to the trans form. Moreover, we note that the isotherm compression-expansion is completely reversible in the dark while showing a slight hysteresis under UV or visible light irradiation. Nevertheless, these compression-expansion cycles suggest that even at the highest pressures reached (18 mN m^{-1}) there was no signature of an irreversible film collapse or other degradative effects discernible in the isotherms, hence the applied films deformation is fully reversible.

To verify the specific structure-guiding character of the fluorocarbon chain, we performed experiments under similar conditions with the analogue azobenzene derivative H8-azo-H8, which contains two identical hydrocarbon chains instead of a fluorocarbon chain. Again, we observe from surface pressure-area isotherms that the molecules occupy a molecular area about three times larger in the cis configuration under UV irradiation compared to the trans isomer in the dark (Figure 4.3). More specifically, in the case of H8-azo-H8 monolayers under UV irradiation the surface pressure starts to increase for $A = 60 \text{ \AA}^2/\text{molecule}$, which is 3 times larger than the molecular area that is occupied by the H8-azo-H8 monolayers under dark. Under UV irradiation, by com-

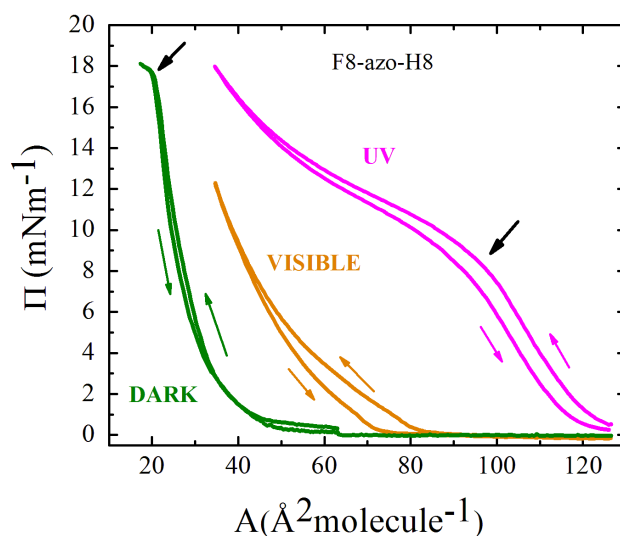


Figure 4.2: Surface pressure (Π) versus molecular area (A) isotherms of F8-azo-H8 monolayers at the air-water interface at 20°C, under different irradiation conditions: UV light inducing predominantly cis configuration (right curve in purple, labelled "UV"), visible light with cis and trans configurations (middle curve, orange, "VISIBLE") and in the dark with trans configurations (left curve, green, "DARK"). The arrows indicate compression and expansion directions with very little hysteresis.

pressing the layer the surface pressure increases until 8 mN m^{-1} which corresponds to a molecular area of 25 Å^2 . Moreover, there is a kink observed at $A = 35 \text{ Å}^2/\text{molecule}$ which corresponds to a probable collapse (changing in the packing order). For all the different light conditions the compression-expansion cycles suggest that the films deformation is fully reversible.

In Figure 4.4a the variation of the surface pressure overtime for a F8-azo-H8 monolayer is presented upon exposure to different light stimuli. The measurement started when the monolayer was compressed at a surface pressure of 2 mN m^{-1} in the dark and after about 1 hour the UV lamp was switched on. During this irradiation the surface pressure increased and reached a maximum value of about 16 mNm^{-1} within about 1 hour. Then the monolayer was exposed to visible light and the surface pressure dropped to 4 mNm^{-1} after 3 hours. A similar measurement was performed for its hydrogenated analogue H8-azo-H8. In Figure 4.4b the surface pressure versus time of a H8-azo-H8 monolayer at the air-water interface is shown. The time-resolved surface pressure shows increase under UV irradiation (although not as high values as for F8-azo-H8) from $\Pi = 2 \text{ mN m}^{-1}$ to $\Pi = 8 \text{ mN m}^{-1}$, but no significant change is observed when switching off

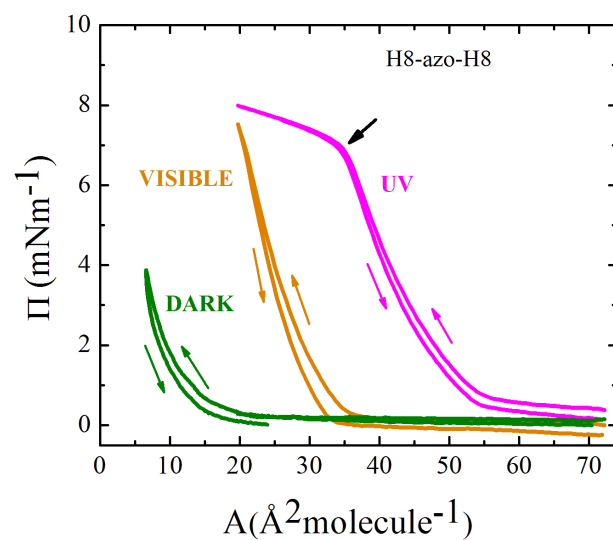


Figure 4.3: Surface pressure (Π) versus molecular area (A) isotherms of H8-azo-H8 monolayers at the air-water interface at 20°C. Under UV light with cis configurations (right, purple curve), under visible light with cis and trans configurations (middle, orange) and in the dark with trans configurations (left, green).

UV irradiation. The data indicate that the H8-azo-H8 monolayer is stable under these experimental conditions.

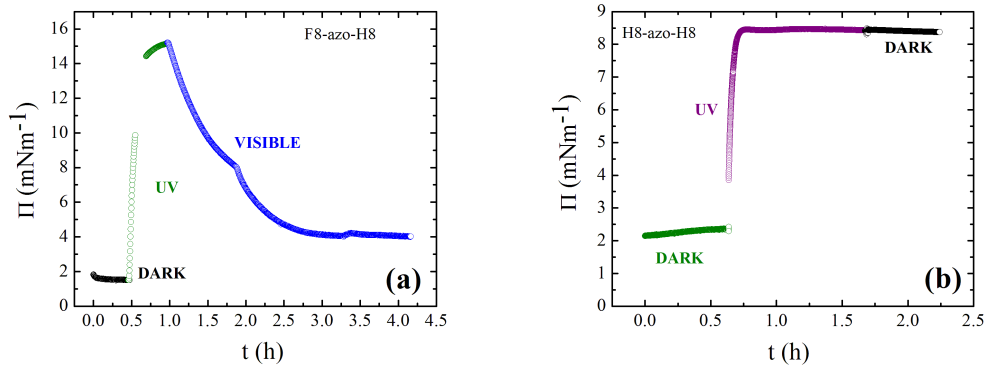


Figure 4.4: Variation of the surface pressure (Π) overtime (t) for a) a F8-azo-H8 monolayer (pure water subphase, 20°C) under different light stimuli. In the dark (black), UV (green), and visible light (blue) and b) for a H8-azo-H8 monolayer at the air-water interface at 20°C. Under dark (left / green, start), UV (middle / purple), dark (last / black) .

4.3 Interfacial Rheology

In order to determine the viscoelastic properties of F8-azo-H8 film upon exposure to different light stimuli, dynamic time sweep tests were performed with the magnetic rod interfacial stress rheometer at strain amplitude $\gamma=0.1\%$ and at $\omega=0.6$ rad/s. The results of these measurements are demonstrated in Figure 4.5 where they depict the UV-induced change of the storage (G') and loss (G'') moduli. In Figure 4.5a the measurement started when the monolayer was compressed to surface pressure 6 mNm⁻¹ under dark light conditions. After 60 min the monolayer was irradiated with the UV light. This led to an increase of surface pressure to $\Pi = 19$ mNm⁻¹ and an order of magnitude decrease to the storage and loss modulus. After 70 min the UV light was switched off and for the next 30 min the moduli remained stable. A second dynamic time sweep test is demonstrated in Figure 4.5b where the measurement under dark starts at surface pressure of 12 mNm⁻¹. In the course of the experiment the conditions changed from dark to UV irradiation. This resulted in an increase of the surface pressure to 17 mNm⁻¹, which is apparently caused by a structural reorganization of the F8-azo-H8 film leading to a decrease of G' and G'' by about one order of magnitude when UV is switched on. In this case, the moduli response is almost instantaneous when changing irradiation, while for static lighting conditions the moduli are constant. Finally, it is worth mentioning that the moduli are very weak and the response of the F8-azo-H8 monolayers is liquid-like.

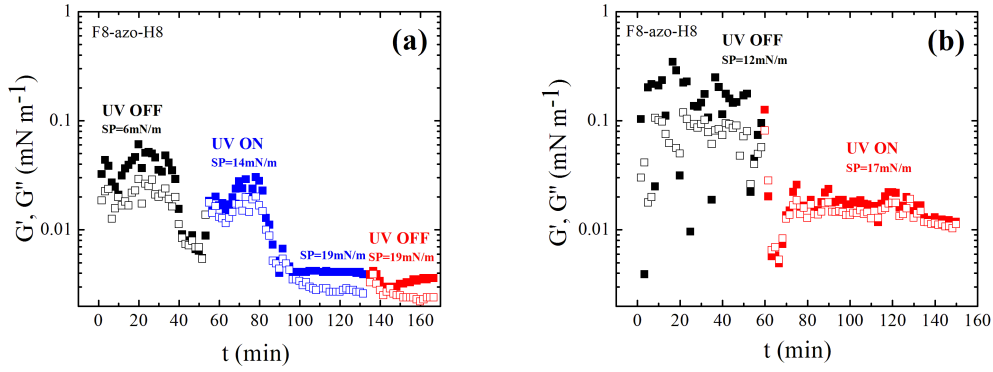


Figure 4.5: Dynamic time sweep measurement of storage (G' , closed symbols) and loss (G'' , opened symbols) moduli for F8-azo-H8 films at the air-water interface at a temperature of 20°C , frequency $\omega=0.6 \text{ rad s}^{-1}$ and strain amplitude $\gamma_0=0.1\%$ using the magnetic rod interfacial stress rheometer. The measurement started at a surface pressure of a) 6 mNm^{-1} and b) 12 mNm^{-1} . Light conditions: UV off, then UV on.

As described previously, a series of dynamic time sweep measurements were performed using the magnetic rod interfacial stress rheometer starting at different surface pressures. In Figure 4.6 the storage modulus (G') versus surface pressure of the F8-azo-H8 monolayer at the air-water interface for three different starting surface pressures $\Pi=2 \text{ mNm}^{-1}$, $\Pi=6 \text{ mNm}^{-1}$ and $\Pi=12 \text{ mNm}^{-1}$. As a general trend, we find that G' is reduced upon UV irradiation while at the same time the surface pressure increases. It can be further concluded that the lower the initial surface pressure in the dark, the larger the surface pressure jump and the lower the modulus decrease when UV is switched on. We discuss below the structural analysis of the films, which was performed by neutron reflectivity measurements. In all measurements including all the investigated light conditions we notice that the moduli are very weak indicating a liquid-like response. This is further confirmed by analysis of the apparent Poisson ratio of the films. The effective compression modulus, $\varepsilon = -A \text{ d}\Pi/\text{d}A$, extracted from the pressure area isotherms, is of the order of 10 mNm^{-1} , i.e., orders of magnitude higher than the shear modulus. Hence, the Poisson ratio of the quasi-2D layer is $\nu = \varepsilon / (\varepsilon + G) \approx 1$, which is the expected value for a liquid interface (Jasiuk *et al.* (1994), Bhaskar, Tretiakov and Wojciechowski (2007)).

The linear viscoelastic behaviour of H8-azo-H8 under dark and UV irradiation was investigated using the magnetic rod interfacial stress rheometer. Dynamic frequency sweep measurements were performed in the range of $0.1 \text{ rad/s} < \omega < 10 \text{ rad/s}$ at strain am-

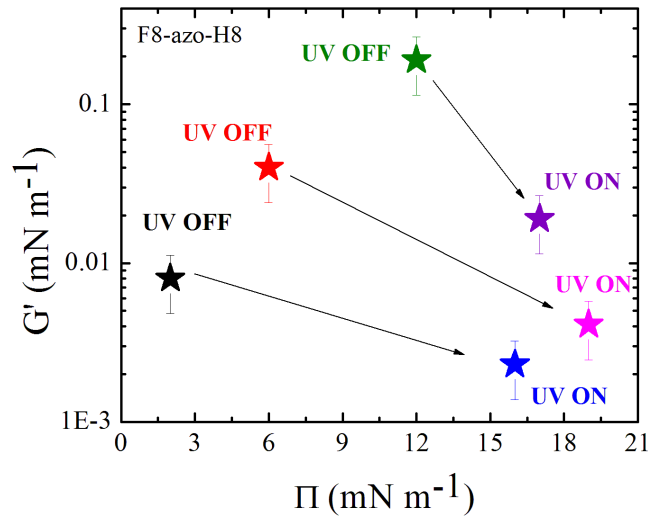


Figure 4.6: Storage modulus (G') versus surface pressure of the F8-azo-H8 monolayer at the air-water interface showing the order of magnitude decrease of the elastic modulus under UV irradiation for three different starting surface pressure, $\Pi=2\text{mNm}^{-1}$, $\Pi=6\text{mNm}^{-1}$ and $\Pi=12\text{mNm}^{-1}$.

plitude $\gamma=0.1\%$. Figure 4.7 depicts the storage modulus (G') and the loss modulus (G'') as a function of frequency (ω) of H8-azo-H8 layers. Interestingly, the H8-azo-H8 interface has a viscous rheological response indistinguishable from the water subphase. It's worth to be mentioned here that the positive value of G' at low frequency is due to the compliance of the setup and must not be attributed to any physical properties of the layer. Similarly with F8-azo-H8, almost one order of magnitude decrease was observed in the interfacial moduli moving from trans to cis conformations.

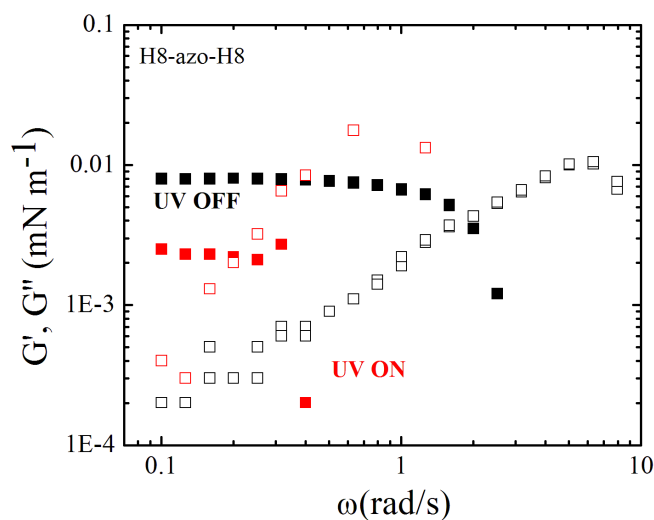


Figure 4.7: Dynamic frequency sweep measurement of storage (G' , closed symbols) and loss (G'' , opened symbols) moduli for a H8-azo-H8 monolayer at the air-water interface at a temperature of 20°C at strain amplitude $\gamma_0=0.1\%$ using the magnetic rod interfacial stress rheometer. The measurement started at a surface pressure of 2 mNm⁻¹ (black symbols) and then after the UV was on the surface pressure increased to 8 mNm⁻¹ (red symbols).

4.4 Neutron Reflectivity

Complementary neutron reflectivity measurements were performed at the water-air interface in order to investigate the organization of the azobenzene containing semifluorinated alkanes upon exposure to different light stimuli. After obtaining the neutron reflectivity data as a function of the scattering vector q , we try to assess available packing models by variation of the structural parameters such as number of layers, layer thickness, scattering length density and surface roughness for each layer. The results from the neutron reflectivity experiments of F8-azo-H8 under dark are depicted in Figure 4.8 and under UV irradiation in Figure 4.9, where the scattering curves as normalized intensity versus q are compared with the bare D₂O subphase in the dark and under UV irradiation. In the upper insets of these figures we show the same data in a more sensitive representation (Normalized Intensity (NR) * q^4 versus q) that allows to better distinguish the small structural effect of F8-azo-H8 at the air-water interface, which is consistent with the scattering length density profiles of the lower insets. In the SLD profile zero scattering length density corresponds to the air phase and the upper limit to the deuterated water phase. From the best fitting we can extract the scattering length

density profile and the proposed molecular model for interfacial arrangement of the F8-azo-H8 molecules in the monolayer. A two layer model with total layer thickness of 43.7 Å with the CF-blocks pointing towards the subphase, is suggested. In the Appendix C of this thesis we present the non-convergent fit of the model, where the fluorocarbons point towards the air and the hydrocarbons are on contact with the aqueous phase. Under UV irradiation, an average layer thickness of 9.6 Å is found for a structureless film with random molecular orientation. As schematically illustrated in Figure 4.10, it is suggested that the F8-azo-H8 molecules in their trans configuration organize with their long axis perpendicular to the air-water interface in the dark. When the UV light is switched on, the induced trans-to-cis isomerization gives rise to a random, structureless arrangement. This configuration-induced change of packing order is accompanied by a decrease of interfacial viscoelastic moduli and a concurrent increase of surface pressure.

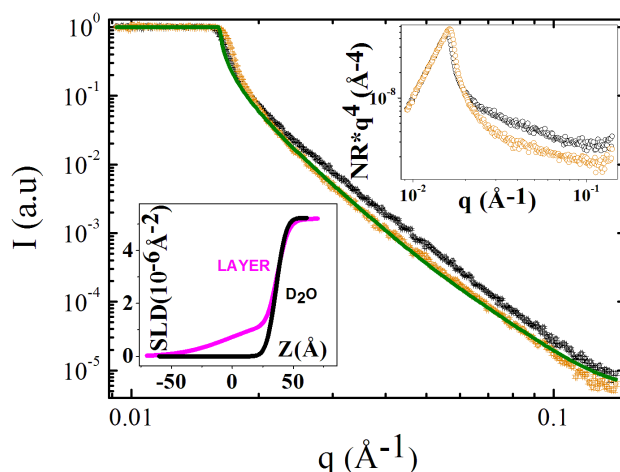


Figure 4.8: Neutron reflectivity curve (Normalized Intensity $I(\text{a.u.})$ vs q) of the F8-azo-H8 monolayer on a D_2O subphase in the dark next to the corresponding scattering length density profile in the lower inset. Upper inset: Normalized Intensity (NR) $\cdot q^4$ versus q . Colour legend: D_2O (black), F8-azo-H8 under dark (orange) and fit (green). $\Pi = 2 \text{ mNm}^{-1}$ at 20°C .

In Figure 4.11 the results from the neutron reflectivity experiments of H8-azo-H8 under dark and under UV are demonstrated. The scattering curves as normalized intensity versus q are compared with the bare D_2O subphase in the dark and under UV irradiation. In the upper insets of these figures we show the same data in a more sensitive representation (Normalized Intensity (NR) $\cdot q^4$ versus q), which is consistent with the scattering length density profiles of the lower insets. From the best fitting we can extract

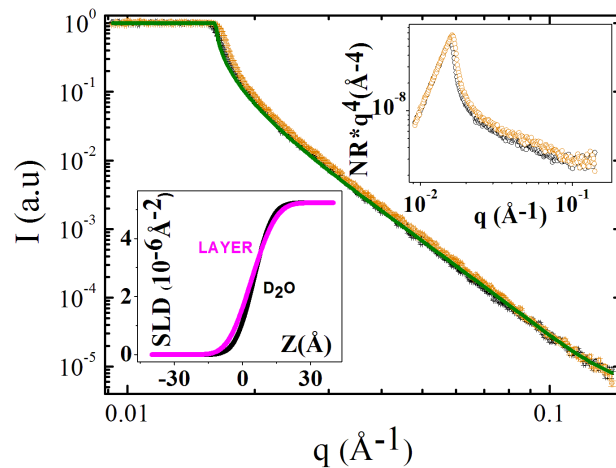


Figure 4.9: Neutron reflectivity curve (Normalized Intensity (I (a.u.) vs q) of the F8-azo-H8 monolayer on a D_2O subphase under UV irradiation together with the scattering length density profile in the lower inset. Upper inset: Normalized Intensity ($NR \cdot q^4$) vs q . Colour legend: D_2O (black), F8-azo-H8 under UV (orange) and fit (green). $\Pi = 12 \text{mNm}^{-1}$ at 20°C .

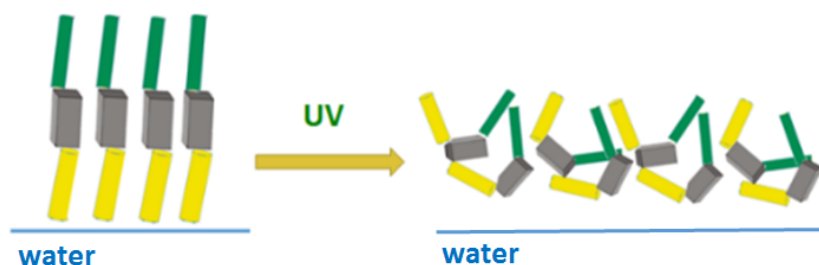


Figure 4.10: Model proposed for F8-azo-H8 monolayer at the water-air interface before and after its exposure to UV light.

the scattering length density profile and the proposed molecular model for interfacial arrangement of the H8-azo-H8 molecules in the monolayer. A layer thickness of 6.5 Å for a structureless film morphology with random molecular orientation is found for both isomers in the dark and under UV exposure. In this case, a different model for the molecular arrangement of H8-azo-H8 is suggested as it is depicted in Figure 4.12. The molecular packing models providing the best fit to the reflectivity curves indicate a loose random organization of the molecules with no significant effect of light irradiation on the level of spacial correlation.

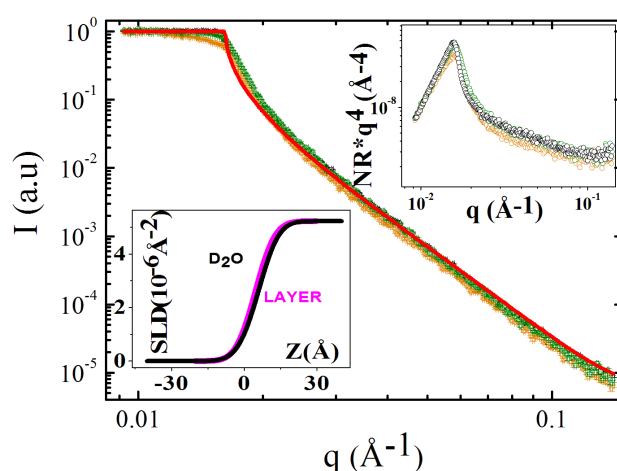


Figure 4.11: Neutron reflectivity curve (Normalized Intensity ($I(\text{a.u.})$) vs q) of the H8-azo-H8 monolayer on a D_2O subphase in the absence of light and under UV irradiation along with the scattering length density profile in the lower inset. Upper inset: Normalized Intensity (NR) $\times q^4$ versus q . Colour legend: D_2O (black), H8-azo-H8 under dark (orange), H8-azo-H8 under UV (green) and fit (red). Surface pressure = 2 mNm^{-1} under dark and $\Pi = 8 \text{ mNm}^{-1}$ under UV at 20°C .

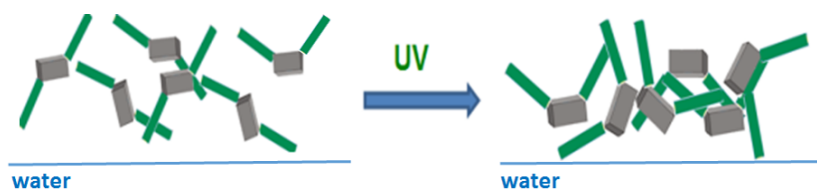


Figure 4.12: Model proposed for the H8-azo-H8 monolayer at the air-water interface before and after its exposure to UV light.

4.5 Concluding Remarks

We investigated monolayers of the semifluorinated azobenzene derivative (E)-1-(4-octylphenyl)-2-(4-(perfluorooctyl)phenyl)diazene (in short F8-azo-H8) and its fully hydrogenated analogue (E)-1,2-bis(4-octylphenyl)diazene (abbreviated here as H8-azo-H8) at the air-water interface. We have studied the structural and rheological tunability of these layers at the air-water interface, under different conditions of light irradiation by neutron reflectivity, surface pressure-area isotherms with compression-expansion cycles, and interfacial rheology using the magnetic rod interfacial stress rheometer. Based on the well-known photochromic effect of UV and visible light irradiation on the cis-trans isomerization, such light exposure drastically influences also the packing behaviour of the SFA azobenzene molecules in a reversible way. Here it was found that the UV irradiation significantly influences the interfacial organization and viscoelasticity of the SFA derivatives of F8-azo-H8 and the symmetric hydrocarbon derivative H8-azo-H8.

From the surface pressure/area isotherms under different light irradiating conditions we found that the molecular area occupied by the cis-configured molecules is 3 times larger than the area occupied by the trans configurations. From the neutron reflectivity experiments we found that for the case of F8-azo-H8, a transition from an organized layer structure with the molecular main axis vertically oriented in the trans form to random packing of the cis isomer can be observed and it is accompanied by a decrease of the layer thickness. In the case of H8-azo-H8 layers from neutron reflectivity it was not possible to distinguish the expected ordered structure that was found from the surface pressure/area isotherms because of the weak signal of the reflectivity data that were close to the response of water. Interestingly, for both semifluorinated alkyl-azobenzene derivatives we found that upon UV irradiation the increase in surface pressure is accompanied by a decrease of viscoelastic moduli. It turns out that the fluorocarbon component of the F8-azo-H8 molecule has a pivotal role as it is responsible for the presence of a strong dipole in the F-H direction, i.e. along with extended and stiff molecular shape of the azobenzene moiety in the trans-configuration, yielding the perpendicular order as indicated in Figure 4.10.

To conclude, these findings confirm the capability of these systems to change behaviour upon irradiation with light and provide the means to tailor their mechanical

properties by exploiting the sensitivity of molecular configuration to UV irradiation. To complete this study it would be highly desirable to investigate azobenzene molecules containing semifluorinated alkanes with higher molecular weights in order to study the effect of the length of azobenzene chains on the overall response of the layers.

CHAPTER 5

FOURIER TRANSFORM RHEOLOGY OF PMMA INTERFACES

5.1 State of the art

The two-dimensional rheology of liquid-liquid interfaces has been a subject of research, mainly because of its significant role in the stability of foams and emulsions. Also the importance of understanding the dynamics and the mechanical properties of such systems is a topic of great scientific interest targeting in the tuning of interfaces for specific applications. There are three different types of deformation that can be applied on the interfaces as it can be seen in Figure 5.1: 1) shear deformation 2) planar extension and 3) dilatational deformation. The first and the second corresponds to a deformation where the area does not change, while the third is accompanied by a change of the area. The linear and non-linear rheological characterization of liquid-liquid interfaces can be achieved nowadays using a variety of different experimental setups for shear and dilatational rheology. (Brooks *et al.* (1999), Vandebril *et al.* (2010), Erni *et al.* (2003), Miller *et al.* (1993), Miller *et al.* (2010)). In measurements performed under oscillatory shear, we typically distinguish two regimes: 1) the small amplitude oscillatory regime (SAOS), also called linear viscoelastic (LVE) regime, where the stress is well described by a single Fourier harmonic and 2) the large amplitude oscillatory regime (LAOS), where the stress response is a distorted sinusoidal function and more than one harmonic must be employed to fit his temporal behaviour. Most of the reported studies concerning in the non-linear interfacial rheology have been performed using the barrier oscillation method in Langmuir trough, the pendant drop and the bi-conical device as well. (Danov *et al.* (2012), Erni *et al.* (2012), Erni and Parker (2012), Krishnaswamy *et al.* (2007), Torcello-Gomez *et al.* (2011), Jaishankar *et al.* (2011)).

In bulk rheology, large amplitude oscillatory shear (LAOS) measurements have become very popular as a tool to characterize the nonlinear rheological properties of the materials, being the non-linear viscoelastic response of a material easily quantifiable by

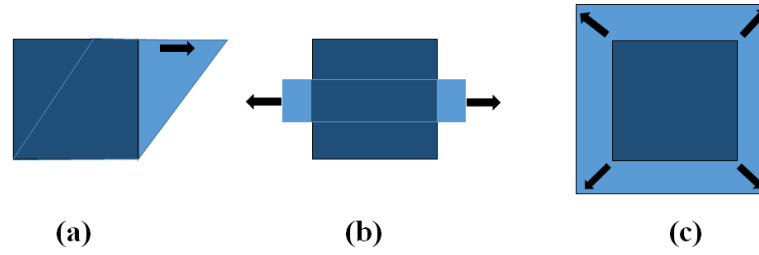


Figure 5.1: Interfacial rheometry flows a) shear, b) planar extension and c) dilatation.

using Fourier transform analysis (Wilhelm *et al.* (1998)). During a LAOS experiment, an oscillatory strain (or stress) is imposed on the sample and its stress (strain) response is collected in time. In LVE regime the collected signal has always the same frequency but a non-zero phase shift according to the magnitude of the dissipated energy by the system within one cycle (magnitude of G''). In the case of the nonlinear regime the response signal consists of higher harmonics (multiples of the excitation frequency). The LAOS response can be described by the Bowditch-Lissajous plots (van Dusschoten and Wilhelm (2001)), where the stress is plotted versus strain or strain rate.

Since the 1960's, LAOS experiments have been performed for natural rubber and rubber filled with carbon black (Payne (1962)). Earlier publications (Harris (1965), Onogi and Matsumoto (1970), Matsumoto *et al.* (1973), Tee and Dealy (1975)) proposed FT-rheology as a powerful tool to extract structural information of viscoelastic materials in the non-linear regime. These days, FT rheology is used for polymer melts (Fleury *et al.* (2004), Schlatter *et al.* (2005), Sugimoto *et al.* (2006)), polymer solutions (Neidhofer *et al.* (2003), Neidhofer *et al.* (2004)), polymer blends (Carotenuto *et al.* (2008), Filipe *et al.* (2004)), proteins and colloidal materials (Wilhelm *et al.* (2000)). Philippoff (1966) investigated the nonlinear response of polymer solutions and they detected the growth of third harmonics. Also Onogi and Matsumoto (1970) observed odd harmonics up to the order of 5^{th} order. In dispersions, Klein *et al.* (2007) observed non negligible contribution of higher harmonics up to the 20^{th} order while very high harmonics ($>150^{th}$) are distinguishable in emulsions (Hyun *et al.* (2011)). During the 1990's, important contribution in LAOS research was achieved by Giacomini (Giacomini and Oakley (1992), Giacomini *et al.* (1993)) that performed waveform analysis and the Fourier transform analysis of the stress periodic response. Wilhelm *et al.* (Wilhelm *et al.* (1998), Wilhelm *et al.* (1999), Wilhelm *et al.* (2000), van Dusschoten and Wilhelm (2001)) developed a method for high sensitivity Fourier transform using NMR spec-

troscopy and oscillatory rheology and their contributions led to an improvement of 2-3 decades in the signal to noise ratio with a final signal to noise ratio $S/N=10^5$. The goal of recent research in LAOS is the physical interpretation of the nonlinear signals and the use of Chebychev polynomials (Ewoldt *et al.* (2008)). Klein *et al.* (2007, 2008) have used different kind of orthogonal set of functions to decompose the stress response in the non linear regime. Interpretation of LAOS signal remains a challenge due to the non-constant flow history.

Comparing with the 3D nonlinear rheology, at fluid interfaces there is not much progress in the field of the nonlinear rheology because of the complexity in the understanding of the data in interfacial rheology. In literature, the method of the oscillation barriers of a Langmuir trough is commonly used. In this method the barriers of the Langmuir trough are moving sinusoidally inwards and outwards causing a sinusoidal response in the surface pressure of the layer that is measured with the Wilhelmy plate. So, by repeated compression expansion cycles the compression modulus of the interfacial layer is probed. It's worth to mention that here the main contributions to the deformation comes from the dilatational components and compression rather than the shear ones. Hilles *et al.* (2006) used the oscillation barrier method and described a Fourier transform method to analyze the interfacial rheology data of insoluble Langmuir polymer monolayers beyond the linear viscoelastic regime using a simple 2-D rubber model to describe the behaviour of the monolayers in the non-linear region. Also they found that in the concentrate regime, the monolayers show a transition from elastic to plastic behaviour. Another very commonly used method in interfacial rheology is the bi-conical device that is mounted in a Physica MCR rheometer (Anton Paar) and is of the great advantage to be more accurate with respect to the resolution of torque and deformation. Given to the high quality data of this device it has been used to study the LAOS behaviour of surfactants and proteins (Torcello-Gomez *et al.* (2011), Jaishankar *et al.* (2011), Wulff-Perez *et al.* (2011) and Espinosa *et al.* (2011)). The drawback of the bi-conical device method is that it cannot control the surface pressure. However, a method which combines both high accuracy and control of the surface pressure is the double wall ring (DWR) fixture that is mounted in an DHR rheometer with a Langmuir trough that can control surface pressure by moving the barriers (Vandebril *et al.* (2010), Hermans and Vermant (2014)). The Fourier transform analysis of LAOS measurements using the DWR fixture has not been studied up to now in the literature and one of

the goals of this chapter was to investigate the presence of higher harmonics using the DWR.

From the above literature review it is evident that despite the huge progress in FT analysis of bulk rheology there has not been great progress in the same field for two-dimensional systems. Problems related with the even harmonics and more specifically with the slip phenomena are still under debate. The most sensitive technique that measures interfacial rheology is the magnetic rod interfacial stress rheometer, whose response, in terms of higher harmonics spectrum has not been investigated up to now. We include such study in this thesis aiming to improve the current set-up by showing the higher harmonics are often due to issues concerning subphase drag, the geometry and the surface properties of the magnetic rods and the channels.

In the current chapter we used as model system Poly(methyl methacrylate) polymer (PMMA) ($M_w=270000$ g/mol) to build layers at the air-water interface. PMMA was chosen as model system because it has been widely studied in the bulk and, moreover it forms very stable elastic monolayers at the air-water interface. We performed non-linear measurements of PMMA layers with different set ups and we employed different methods in order to investigate the presence of higher harmonics between the different set ups and methods. The set ups that were used are the magnetic rod interfacial stress rheometer, the bi-conical fixture and the double wall ring fixture. Using the ISR, we varied the methods by using different sizes of channels, PMMA-grafted and ungrafted, different magnetic probes such as metallic, glassy and glassy grafted with PMMA. In this chapter we focus to the investigation of the even harmonics (and especially the 2nd harmonic) that are related with the asymmetry of the stress response under oscillatory shear and we try to come up with ways and methods that eliminate these harmonics in the interfacial rheology measurements.

The results and discussion of this chapter have been separated into seven subsections. In the first subsection we present the surface pressure/area isotherms of PMMA (270k) layers. In the second, a short description of the nonlinear Fourier transform analysis. And subsequently one subsection is for one of the different methods that were used where the linear and nonlinear viscoelastic response is presented and finally all the Fourier transform analysis of the nonlinear tests.

5.2 Results and discussion

5.2.1 Surface pressure/area isotherms

PMMA appears to be a promising candidate for investigating the respective rheological nonlinearities because of its ability to form stable elastic layers at the air-water interface. PMMA is a polymer with a high bulk glass transition temperature, T_g ($\sim 115^\circ\text{C}$) and according to Srivastava *et al.* (2011) its rheological properties at the air-water interface exhibit a transition from viscous to visco-elastic and then to a soft glassy monolayer with either an increase of the concentration or a decrease of the temperature. At high concentrations and low temperatures, $G' > G''$ and the G' is almost independent of the angular frequency indicating the formation of a highly elastic-solid phase. At higher temperatures and lower concentrations the rheological properties of the PMMA monolayer follows prediction of the SGR model, assuming a elastic-solid phase that is a glass or gel phase.

For the preparation of the layers, we dissolved an amount of PMMA in chloroform that is a good solvent for PMMA to obtain a solution of concentration $c=1\text{mg/ml}$. Subsequently, we spread $20\ \mu\text{l}$ of the solution using a microsyringe dropwise at the air water interface of a Langmuir trough. After spreading, the monolayer was left at rest for about 15 minutes, for the evaporation of the solvent. It is important to mention that fast compression-expansion cycles were performed as a mixing procedure in order to homogenize the PMMA layer.

The surface pressure-area isotherm of the PMMA (270k) layer is shown in Figure 5.2. Starting from $\Pi=0$, where the layer is in the gas-phase, we compress the layer and the surface pressure that is reached is $\Pi = 45\text{mNm}^{-1}$. Moreover, a kink is observed at $\Pi = 12\text{mNm}^{-1}$, that is an indication of the change in the packing order of the layer. Same results with the same phase transition for all the kinds of tacticity of the PMMA have been reported by Gavranovic *et al.* (2005), Srivastava *et al.* (2011), Capan *et al.* (2005), Hsu *et al.* (2006), and Maestro *et al.* (2009). It is also measured that the molecular area of the PMMA coils is approximately 400 nm^2 (the area at which the surface pressure increases).

Figure 5.3 depicts the compression- expansion cycles of PMMA layers. We note

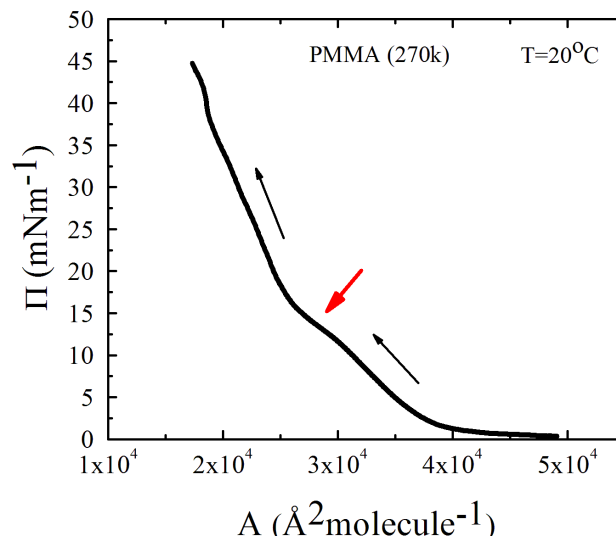


Figure 5.2: Surface pressure/area isotherm of PMMA (270k) monolayer at the water-air interface at 20°C.

that for surface pressures below 12 mNm⁻¹ there is a fully reversible layer deformation. On the contrary, a huge hysteresis during expansion is shown for surface pressure higher than 12 mNm⁻¹. This suggests some kind of thixotropic response of the layer, apparently because some buckling or other local structural change takes place during the compression.

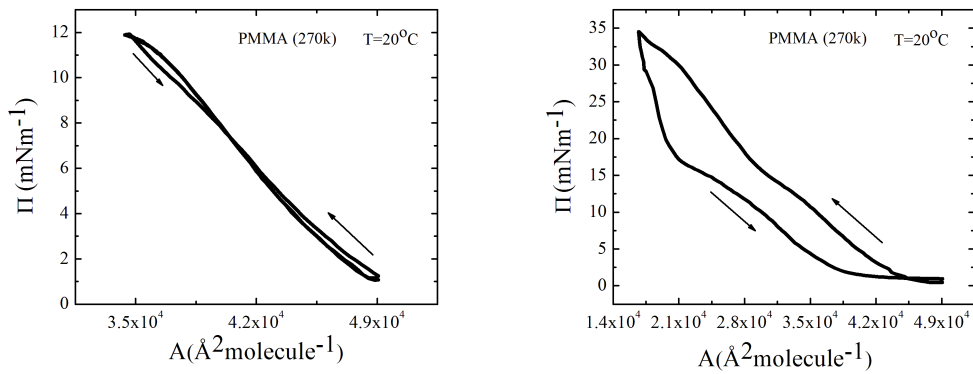


Figure 5.3: Compression- expansion cycles of PMMA (270k). Left panel: before and Right panel: after transition at $\Pi=12$ mNm⁻¹ at 20°C.

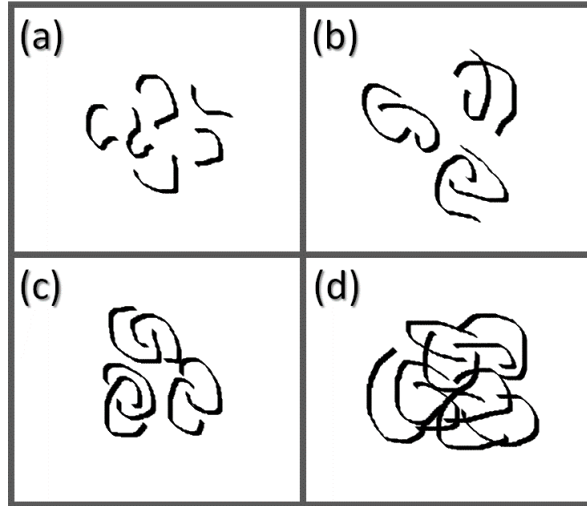


Figure 5.4: Model of PMMA layers at the air-water interface a) gas-phase, b) liquid-phase, c) solid-phase and d) buckling-phase

5.2.2 Nonlinear-FT analysis procedure

The software of the magnetic rod interfacial stress rheometer was adapted in order to control the time domain data of the measurements for the nonlinear tests. It is worth to note that this adaptation could not increase the time resolution of 30 data points per second as determined by the optics. This sampling rate is relevant for the frequency of the modulation signal of the magnetic field and for the detection of the movement of the magnetic rod. On the other hand, the ISR software was equipped with an option to perform a user-defined oversampling (van Dusschoten and Wilhelm (2001)) of the optical data. Also, the voltage data from the modulation of the magnetic field was oversampled. At sufficiently slow excitation frequencies, oversampling takes averages over longer durations and therefore can substantially reduce the noise in the data. Averaging is only done if the time resolution of the data acquisition is sufficient to detect the desired highest frequency of the measurement. This highest frequency is identified with the Nyquist frequency, which is the maximum frequency that can be resolved with a Fourier transform at a certain sampling rate. It is defined as half of the sampling frequency of a discrete signal.

The analysis of the raw time domain data was conducted with a home-written, customized LabVIEW software. This LabVIEW software performs the complete data analysis, reading the data from a file, performing the FT-analysis and saving the selected time domain data, the intensity values and the phase values of the higher harmonics (up

to the ninth harmonic), and the magnitude and phase spectrum of the frequency domain data.

However, there are technical constraints regarding the use of the nonlinear interfacial measurements because the software can record the maximum output of an analog camera of 30 frames per second and can detect the modulation of the magnetic field with the same frequency. For the magnetic rod interfacial stress rheometer, the maximum time resolution is 30 Hz and the Nyquist frequency is 15 Hz. As a consequence for the present set-up, if the magnetic rod of the ISR is excited with a maximum frequency of 1 Hz, and without using oversampling, the detection limit is the 15th higher harmonic. For higher frequencies, oversampling should not be conducted, because it would reduce the amount of data points per second by averaging to a value that is not sufficient anymore to resolve potential higher harmonics, therefore resulting in unreliable data. For the measurements that were performed in this chapter, the excitation frequency was 0.1 Hz so oversampling was applied in all cases and as a result a better signal-to-noise ratio of the raw data was achieved.

Due to large asymmetries of the magnetic rod interfacial stress rheometer, wall slip and possible subphase contribution, the measured response of the layers is expected to show a large contribution of even harmonics. Indeed, the large subphase contribution is expected to create deviations from the linear response that goes beyond the real non-linear behaviour of the layers. In the following subsections we present different set ups and methods: Layers of PMMA homopolymers were deposited at air-water interface and their rheological response was analyzed via FT-analysis at different strain amplitudes.

5.2.3 Magnetic rod interfacial stress rheometer: The effect of channel size

We used a Teflon-coated steel sewing needle that can be approximated as a rod with length 55.2 mm and diameter 500 μm . It is important to note that it is not a true symmetric rod but a rotationally symmetric needle with one sharp edge. In Chapter 2 the details of the instrumentation are presented. In the ISR set up the edge of one end of the rod was monitored, and the position was recorded in pixels of the camera. In all

rheological measurements with the ISR the excitation frequency $\omega=1/2\pi$ ranged from 0.0016 to 1.6 Hz, and the strain amplitude (γ) from 0.1 to 100 %. Finally, the dynamic surface moduli G' (storage) and G'' (loss) could be measured with a resolution of about $\pm 1 \mu\text{N/m}$.

Aspect ratio of channel width to rod diameter $\lambda=18$.

The criteria to choose the size of the channel is the capillary length scale q^{-1} ($=\sqrt{\gamma/(\rho g)}$) (Kralchevsky and Nagayama (1994)) which shows the scale at which lateral capillary forces between the walls and the needle become significant and for a water-air interface the capillary length scale is $q^{-1} = 2.7 \text{ mm}$. In this case the channel width is 0.9 cm.

In Figure 5.5a the linear viscoelastic response of PMMA is presented at $\gamma=0.1\%$. All the rheological measurements of this chapter were performed at temperature of 25 °C. Here the surface pressure of this measurement was 16 mNm^{-1} , since the magnetic rod could still move easily through the monolayer. The PMMA monolayer exhibits a dominant elastic behaviour with the storage interfacial modulus being bigger than the loss modulus up to $\omega=2 \text{ rad/s}$. In Figure 5.5b the dynamic strain sweep data are depicted at $\omega=0.6 \text{ rad/s}$. In the strain sweep experiment, the behaviour is elastic up to $\gamma=5\%$ and we can detect a linear regime up to $\gamma=0.3\%$.

In order to investigate the presence of the higher harmonics and specifically the presence of 2^{nd} harmonics, we implemented the Fourier transform rheology (FTR) at the time domain data of the dynamic strain sweep that is shown in Figure 5.5b. In Figure 5.6 the FT magnitude spectra of PMMA are presented for $\gamma=1\%$ where we observe the presence of 2^{nd} harmonics. The inset of this figure shows the normalized intensity of the 2^{nd} harmonics as a function of all strains. At this strain amplitude ($\gamma=1\%$) we present the time domain data and the Bowditch-Lissajous plot in Figure 5.7. We have also to mention that in the magnitude spectrum, higher harmonics up to the 9^{th} harmonic could easily be detected. However, this data is not shown here, because we focus on the most dominant harmonics (2^{nd} harmonics).

Therefore, the induced nonlinear mechanical response is considered to originate from the measurement system as a whole, i.e., the water, the channel, the needle, and the machine (Helmholtz coils, rod). The higher harmonics could in fact originate from

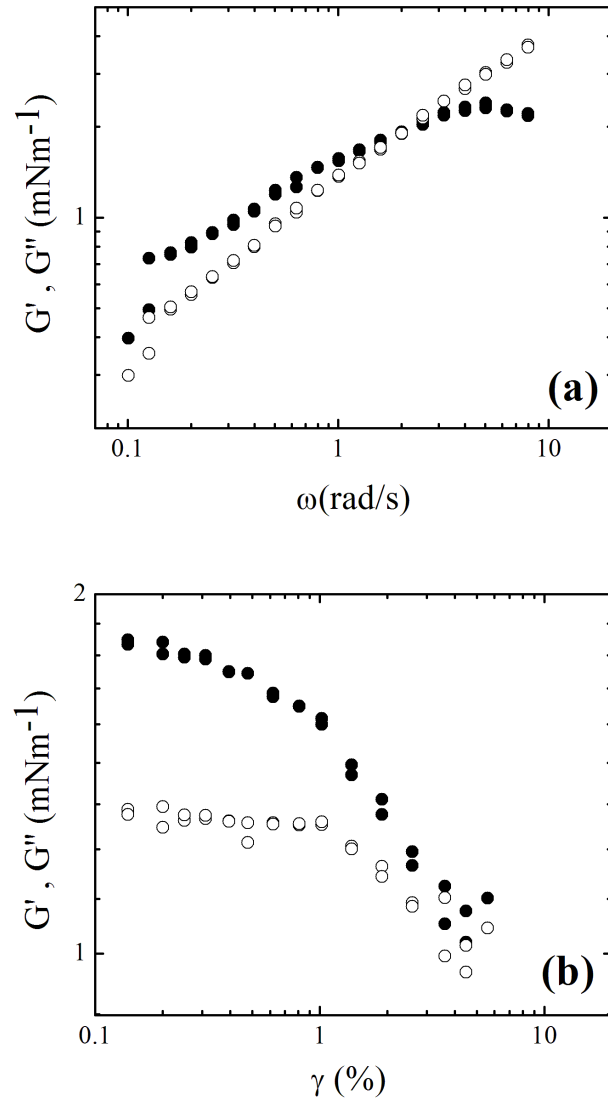


Figure 5.5: Linear and nonlinear rheology of PMMA (270k) using the ISR with channel width 0.9 cm a) dynamic frequency sweep measurement at $\gamma=0.1\%$ and b) dynamic strain sweep at $\omega=0.6$ rad/s. G' (closed symbols) and G'' (open symbols).

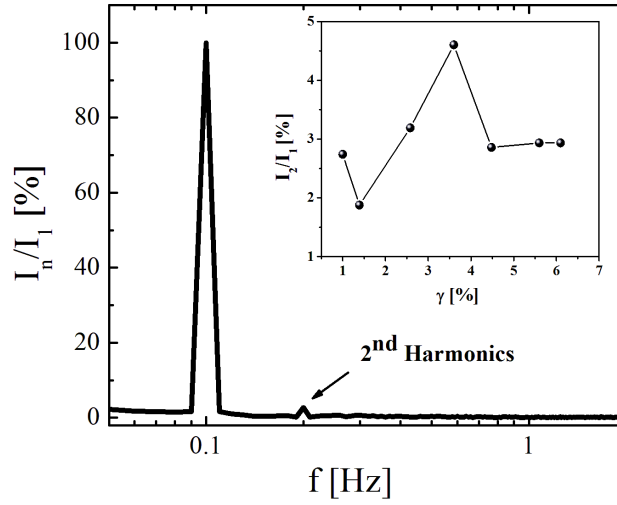


Figure 5.6: FT magnitude spectra of PMMA using the ISR with channel width 0.9 cm at strain amplitude of $\gamma = 1\%$. Inset: Normalized amplitudes of the 2nd harmonics of PMMA as a function of strain amplitude. The excitation frequency was $\omega_1/2\pi = 0.1$ Hz.

an irregular movement at large displacements of the magnetic rod. The water meniscus inside the hydrophilic channel is concave and the magnetic rod lies with its long axis parallel to the channel axis in the minimum of the concave meniscus (due to gravitational forces acting on the rod). During large-amplitude oscillations of the rod the tip approaches the end of the channel where the shape of the water surface is not concave anymore. The magnetic rod may then start to wiggle and move in an irregular fashion, yielding higher harmonics. Another effect is the non-symmetric shape of the magnetic rod used in these experiments. Despite the fact that the needle was approximated as a cylindrical rod in calculations of the dynamic moduli, actually it is ellipsoidal with two different edges, one sharp and one blunt. This asymmetry of the magnetic needle might also affect its movement, especially at large amplitudes, and may even lead to the appearance of even harmonics (Klein *et al.* (2007)).

An alternative technique to analyze nonlinear rheological behaviour in bulk rheology measurements is based on Bowditch-Lissajous plots, where the stress is plotted against the strain. In Figure 5.7-Right panel the function generator (in mV) is plotted as a function of the rod position (in pixel) and it is an analogous plot to the stress vs strain Bowditch-Lissajous plot. Note that interfacial tension could also affect the position of the needle at the interface. Due to the compression, the surface tension increases. This

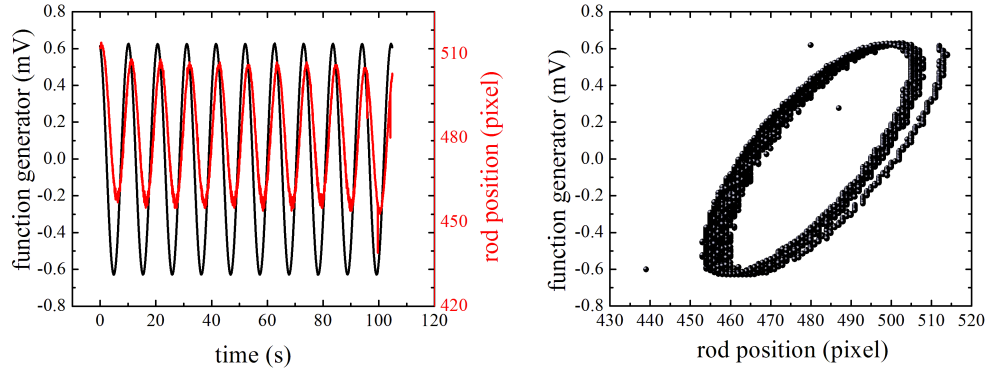


Figure 5.7: Case of PMMA(270k) monolayer using the ISR with channel width 0.9 cm at strain amplitude of $\gamma = 1\%$ and excitation frequency of $\omega_1/2\pi = 0.1$ Hz. Left panel: measurement of the displacement versus time after an applied force. Right panel: Bowditch-Lissajous plot of function generator in mV versus the rod position in pixel.

will decrease the contact angle between the water phase and the needle. As a result, the immersion depth of the needle will increase, and the potential slip between the needle and the monolayer may also increase.

Aspect ratio of channel width to rod diameter $\lambda=14$.

Here we used the same Teflon-coated steel sewing needle that was used in the previous case but with a new channel of width 0.7 cm. The dynamic frequency sweep at $\gamma=0.1\%$ and the dynamic strain sweep at $\omega=0.6$ rad/s results are presented in Figure 5.8, where we observe the presence of an elastic layer. The measurement was performed at surface pressure 14 mNm^{-1} . Also with the ISR we could reach strain amplitudes up to 5%, because after this amplitude the needle escapes from the channel. In order to overcome this amplitude limitation in the future, the channel length should be increased and the shape of the magnetic rod should be more uniform and symmetric.

In Figure 5.9 we notice again the presence of the 2^{nd} harmonics and from the inset of this figure, the intensity of the 2^{nd} harmonics is increasing by increasing strain amplitude. While in Figure 5.10 we can observe the response of the time domain data, the excitation and the response signals at $\gamma = 1\%$ and its Bowditch-Lissajous plot at that strain amplitude. The asymmetry in the Lissajous plot is a signature of the even harmonics and corroborates the FT spectrum shown in Figure 5.9. Comparing the normalized amplitude of second harmonics for the two channels (see insets of Figures 5.6 and 5.9) we may note a completely different behaviour as the size of the channel is

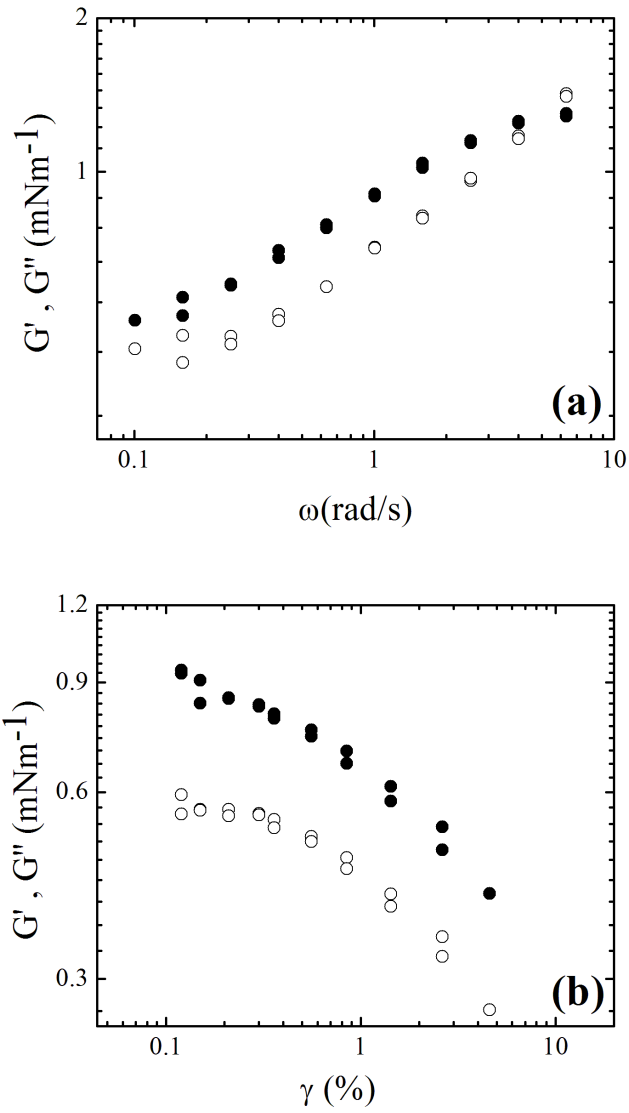


Figure 5.8: Linear and nonlinear rheology of PMMA (270k) using the ISR with channel width 0.7 cm a) dynamic frequency sweep measurement at $\gamma=0.1$ % and b) dynamic strain sweep at $\omega=0.6$ rad/s. G' (closed symbols) and G'' (open symbols).

changed: by employing a smaller channel we obtain a monotonically increasing amplitude of the second harmonics in function of the strain amplitude, while a more irregular dependence is obtained for the larger channel.

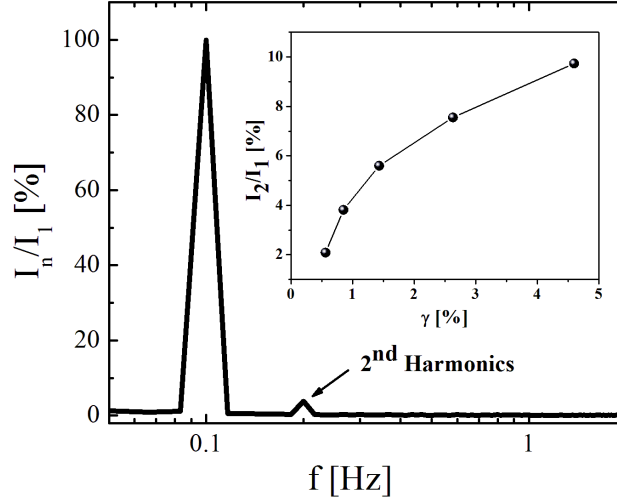


Figure 5.9: FT magnitude spectra of PMMA using the ISR with channel width 0.7 cm at strain amplitude of $\gamma = 1\%$. Inset: Normalized amplitudes of the 2nd harmonics of PMMA as a function of strain amplitude. The excitation frequency was $\omega_1/2\pi = 0.1$ Hz. In Figure D.1 the Log-Linear plot is presented.

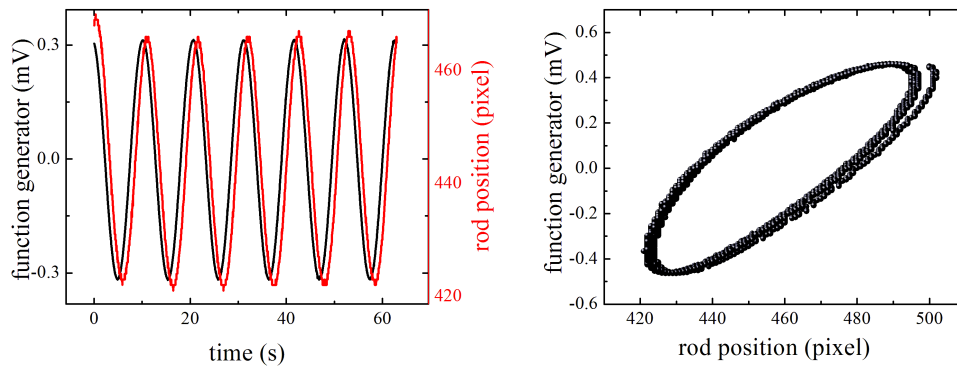


Figure 5.10: Case of PMMA(270k) monolayer using the ISR with channel width 0.7 cm at strain amplitude of $\gamma = 1\%$ and excitation frequency of $\omega_1/2\pi = 0.1$ Hz. Left panel: measurement of the displacement versus time after an applied force. Right panel: Bowditch-Lissajous plot of function generator in mV versus the rod position in pixel.

5.2.4 Magnetic rod interfacial stress rheometer using a PMMA-grafted glassy needle

Using the magnetic rod interfacial stress rheometer, as magnetic probe we used a capillary glass needle that contained a magnetized material in the middle. The length of the glassy needle was 41 mm and its diameter $400\ \mu\text{m}$. In order to optimize the interaction between the surface of this glassy needle and the PMMA interface, the needle was grafted with PMMA (Fig. 5.11).

Before grafting, the needle had to be cleaned: first it was stored in a 2% v/v Helmanex solution for 3 hours, afterwards further cleaning steps included rinsing with water and ethanol, followed by drying in a nitrogen atmosphere. The adsorbed air was then removed from the surface under vacuum. The needle was then incubated overnight in a 4-benzoylphenoxypropyl-(triethoxy)silane ethanol solution, followed by further cleaning with ethanol and N_2 to remove the unreacted silane. PMMA was introduced by dipping the needle in a 2% w/w PMMA THF-solution. The needle containing the PMMA was dried for about 12 hours and then irradiated with UV light for about 30 minutes to graft the polymer on the silane layer at the surface of the needle. Afterwards, the free polymer was washed away with a THF solution.

Figure 5.12 shows the linear and nonlinear rheology of PMMA using the grafted needle. The measurement was performed at surface pressure $10\ \text{mNm}^{-1}$. The inter-

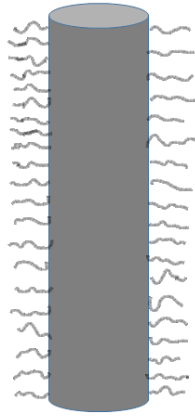


Figure 5.11: A cartoon of PMMA-grafted glassy needle.

facial moduli have lower values comparing to the previous measurements and this can be attributed to the presence of a not very well homogenized monolayer. Figure 5.13 depicts the FT- magnitude spectra after the FT analysis. From the inset of this graph we see that the 2nd harmonics become significant and reach a magnitude that exceeds the 10% of the first harmonic ($I_2/I_1 > 10\%$), and also in this case we saw the existence of third harmonics. Looking at the inset we observe that after strain amplitude of $\gamma=2\%$ the higher harmonics are suppressed and do not grow more. This is expected because of the fact that after this strain amplitude the rheological behaviour of the layer has become a viscous-liquid.

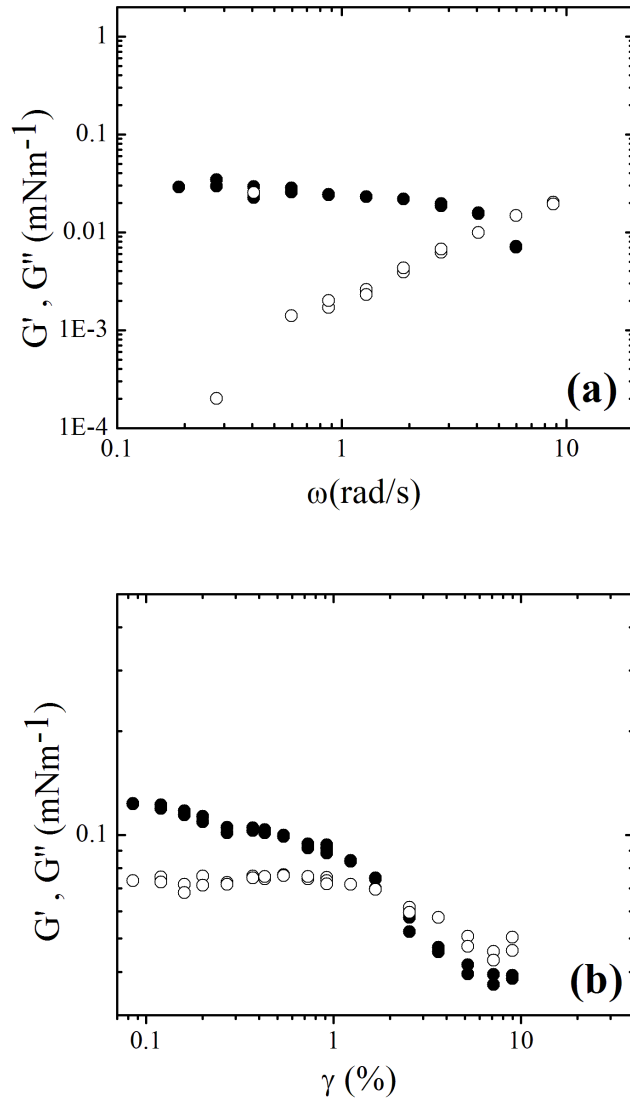


Figure 5.12: Linear and nonlinear rheology of PMMA (270k) using the ISR with a PMMA-grafted glassy needle a) dynamic frequency sweep measurement at $\gamma=0.1\%$ and b) dynamic strain sweep at $\omega=0.6 \text{ rad/s}$. G' (closed symbols) and G'' (open symbols).

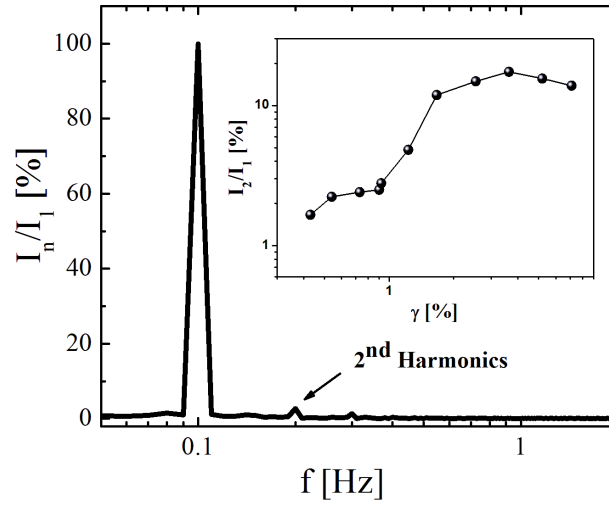


Figure 5.13: FT magnitude spectra of PMMA using the ISR with a PMMA-grafted glassy needle at strain amplitude of $\gamma=1\%$. Inset: Normalized amplitudes of the 2nd harmonics of PMMA as a function of strain amplitude. The excitation frequency was $\omega_1/2\pi = 0.1$ Hz. In Figure D.2 the Log-Linear plot is presented.

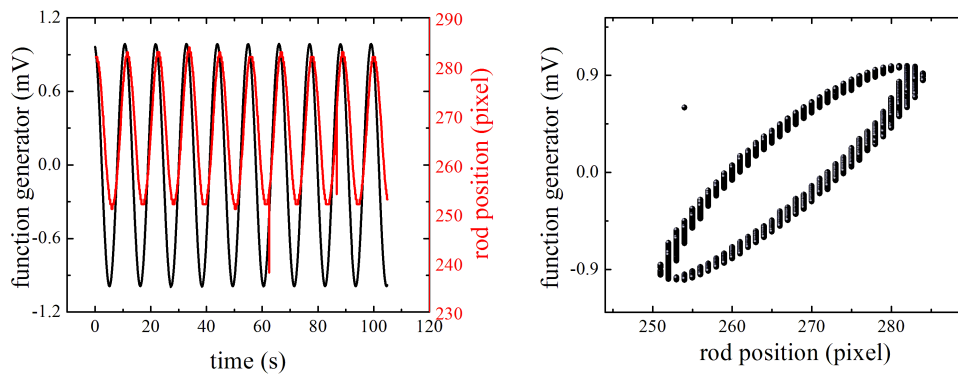


Figure 5.14: Case of PMMA(270k) monolayer using the ISR with a PMMA-grafted glassy needle at strain amplitude of $\gamma=1\%$ and excitation frequency of $\omega_1/2\pi = 0.1$ Hz. Left panel: measurement of the displacement versus time after an applied force. Right panel: Bowditch-Lissajous plot of function generator in mV versus the rod position in pixel.

5.2.5 Magnetic rod interfacial stress rheometer using a PMMA-grafted channel

We continued the investigation of the 2nd harmonics using the magnetic rod interfacial stress rheometer. Here we used as a probe the same Teflon-coated steel sewing needle with a PMMA-coated channel (see Fig. 5.15) in order to improve the contact between the PMMA layer and the walls of the channel. The channel that was made by Polyoxymethylene (POM) polymer was immersed into a concentrated solution of PMMA (270k) and then it was left to dry. The rheological measurements of this system were performed as surface pressure of 12 mNm⁻¹. The linear and nonlinear response of those measurements are presented in Figure 5.16. The dynamic frequency sweep test was at $\gamma=0.1$ % and the dynamic strain sweep at $\omega=0.6$ rad/s. The data of both measurements show that the layer is not well homogenized, showing interfacial moduli lower than the expected values and relatively scattered. We continued with the investigation of the strain sweep data performing the Fourier transform analysis.

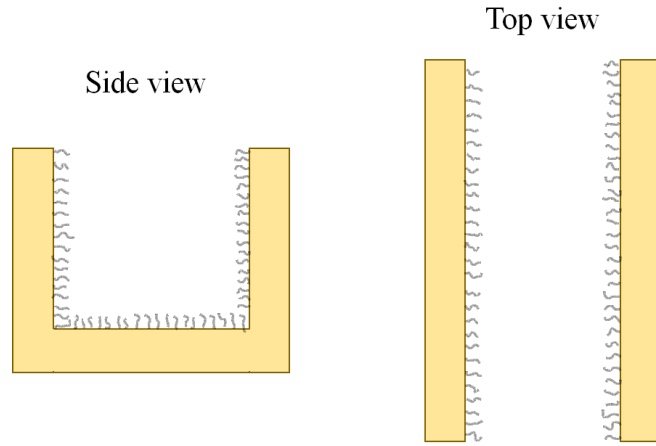


Figure 5.15: A cartoon of PMMA-grafted channel.

The FT analysis proved that also in this case using a grafted PMMA channel we observe 2nd even harmonics with average intensity of $I_2/I_1 \sim 10\%$ in all the amplitude strain range that was studied. It is worth to notice that compared to all the previous cases, here we notice that the intensity of the 2nd harmonic is relatively higher, even at small strain amplitudes. Also the third harmonics are present in this case. Concluding, the PMMA-grafted channel did not lead to any improvement of the elimination of the even harmonics. The time domain data of the excitation and response signal at $\gamma=2\%$

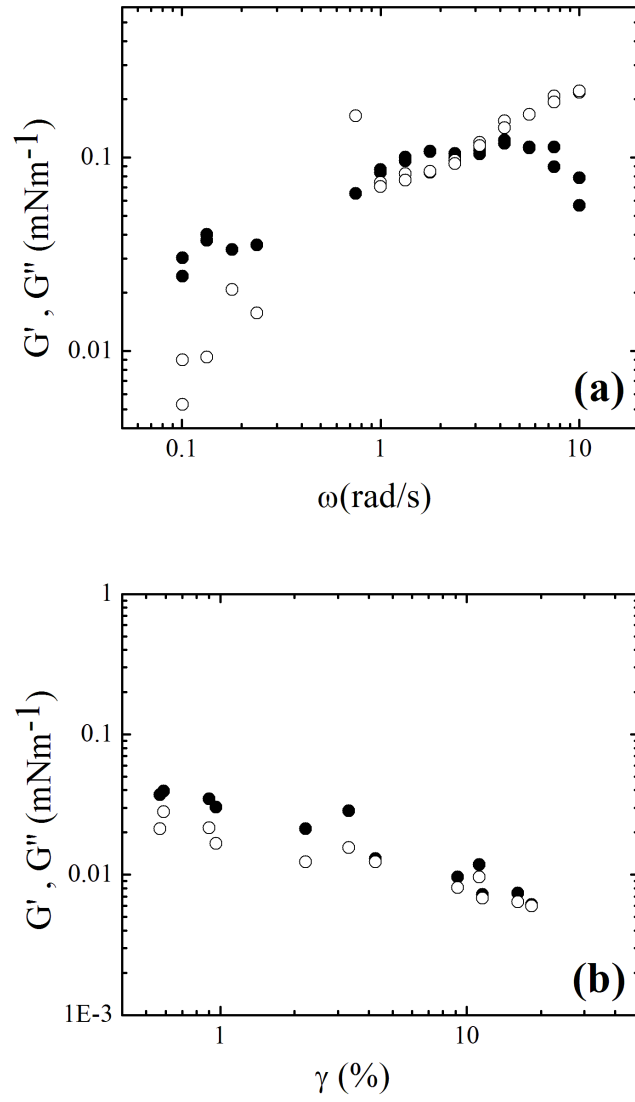


Figure 5.16: Linear and nonlinear rheology of PMMA (270k) using the ISR with a PMMA-grafted channel a) dynamic frequency sweep measurement at $\gamma=0.1\%$ and b) dynamic strain sweep at $\omega=0.6$ rad/s. G' (closed symbols) and G'' (open symbols).

are shown in Figure 5.18 with their corresponding Bowditch-Lissajous plots. From Figure 5.18-Left panel we note that the amplitude of the response signal is increased with the time showing that there is not steady state during this measurement. Correspondingly, the Bowditch-Lissajous plots (Figure 5.18-Right panel) show a continuous shift upon the time passes.

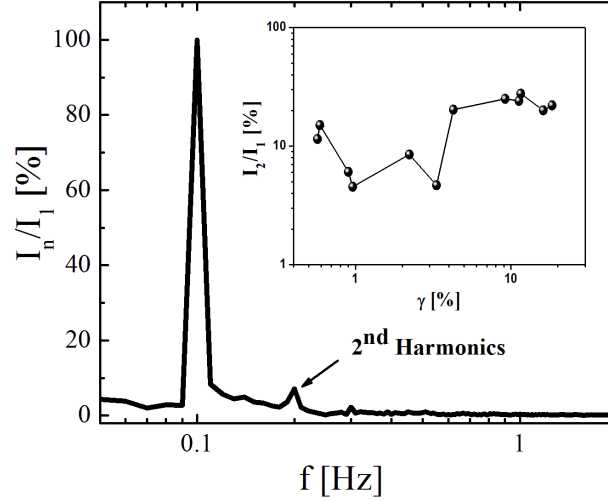


Figure 5.17: FT magnitude spectra of PMMA using the ISR with a PMMA-grafted channel at strain amplitude of $\gamma = 2\%$. Inset: Normalized amplitudes of the 2nd harmonics of PMMA as a function of strain amplitude. The excitation frequency was $\omega_1/2\pi = 0.1$ Hz.

In Figure 5.19 the phases of the 2nd harmonics (Φ_2) are presented as a function of the strain amplitude for all the investigated cases using the magnetic rod ISR. Using the channel with $W=0.7$ cm (black symbols) the phase of the 2nd harmonics is constant, indicating a strong and reproducible signal. With the PMMA-grafted needle (green symbols) an increase of the 2nd harmonic phase is detected, whose value can ideally reach 90° at higher strain amplitude. It is worth to mention here that the phases discontinuously jump from 0 to 360° and vice versa due to the phase periodicity. For this reason few data points have been corrected by adding 360° . According to literature, we have plotted the data in the phase range between 0 - 720° . Looking at the case with $W=0.9$ cm (red data) the signal starts to be stable for strain amplitudes higher than 5% . Interestingly, a rapid fall is observed for the case of the PMMA-grafted channel (blue data) that we attribute to the low and unstable amplitude. Hence, an anomalous behaviour is observed for the PMMA-grafted channel: the intensities and the phases of the 2nd harmonic are strain-dependent and less reliable, while the other methods

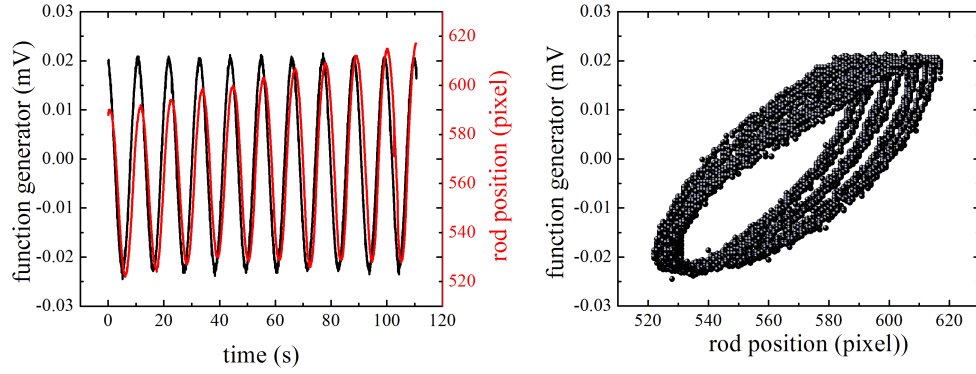


Figure 5.18: Case of PMMA(270k) monolayer using the ISR with a PMMA-grafted channel at strain amplitude of $\gamma = 2\%$ and excitation frequency of $\omega_1/2\pi = 0.1$ Hz. Left panel: measurement of the displacement versus time after an applied force. Right panel: Bowditch-Lissajous plot of function generator in mV versus the rod position in pixel.

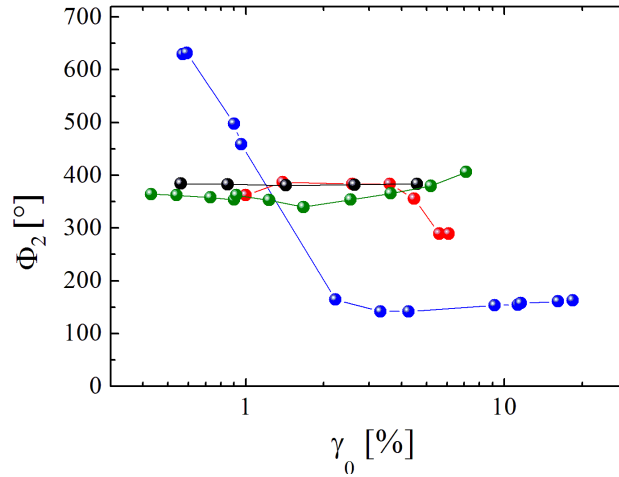


Figure 5.19: Phases of the 2nd harmonics versus strain amplitude for PMMA monolayer measured using different techniques: channel with $W=0.9$ cm (red colour), channel with $W=0.7$ cm (black colour), grafted needle (green colour) and grafted channel (blue colour).

give strain-independent values. This anomaly reported for the grafted channel could be attributed to a possible non-uniform grafted coating.

Comparing all the previous approaches we must conclude that upon changing the size of the needle and the surface chemistry of both the needles and the channels we do not suppress even harmonics, hence we cannot attribute the existence of such non-linear behaviour to these features and other mechanisms must be invoked. We propose that other instrumental artifacts give rise to such effects, some of them related to the tools of the set-up (e.g asymmetric shape or misalignment of the magnetic needle), others to the real 3D-nature of the system (e.g. subphase contribution).

5.2.6 Bi-conical fixture

In order to make conclusive results about the presence of 2^{nd} harmonics in interfacial rheology we performed dynamic strain sweep measurements using the biconal device in a rheometer (Anton Paar) and the data are presented in Figure 5.20 for two different concentrations, 146.27 mg/m^2 and 73.14 mg/m^2 . We have to mention here that the drawback of this set up is that it cannot control the surface pressure. Comparing the interfacial moduli measured by using the bi-conical device and the ISR, we note a huge difference (\sim two order of magnitude) for both G' and G'' . This is not surprising given that the two measurements were performed at different initial concentrations (ISR: 0.47 mg/m^2 . Bi-conal fixture: 73.14 mg/m^2 and 146.27 mg/m^2).

Figure 5.22-Left panel displays the time-domain signal of the PMMA layer, for both the excitation and response and the Bowditch-Lissajous plot for $\gamma = 1\%$. The related magnitude spectrum of the Fourier transform of the excitation signal is shown in Figure 5.21. This signal has a typical signal-to-noise (S/N) ratio of 1000:1 for the first harmonic. Interestingly, in all the investigated range of amplitude strains no even harmonics are presented. In comparison with the ISR, the bi-conical device is more accurate with respect to the resolution of the torque and the deformation, with no defects and asymmetries in the set up and the interfacial tool. This could be the reason of the missing even harmonics.

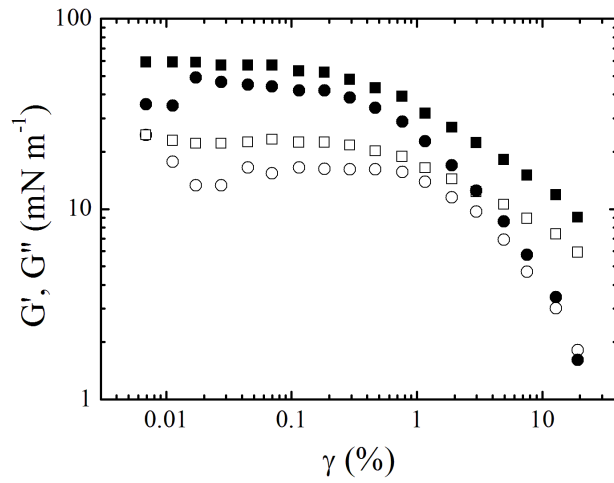


Figure 5.20: Nonlinear rheology of PMMA (270k) using the bi-conal fixture. Dynamic strain sweeps at $\omega=0.6$ rad/s. Concentration 146.27 mg/m^2 (square symbols) and 73.14 mg/m^2 (circle symbols). G' (closed symbols) and G'' (open symbols). [The author kindly acknowledge Patrick Ruehs for having performed the DSS experiment in ETH in the group of P. Fisher.]

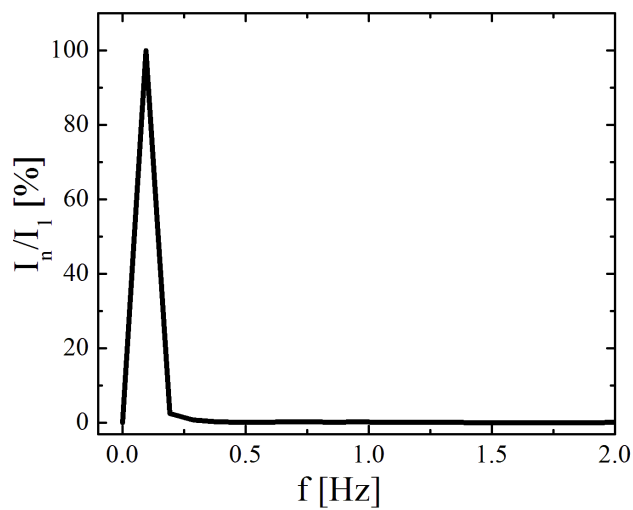


Figure 5.21: FT magnitude spectra of PMMA using the biconal fixture at strain amplitude of $\gamma = 1\%$. The excitation frequency was $\omega_1/2\pi = 0.1$ Hz.

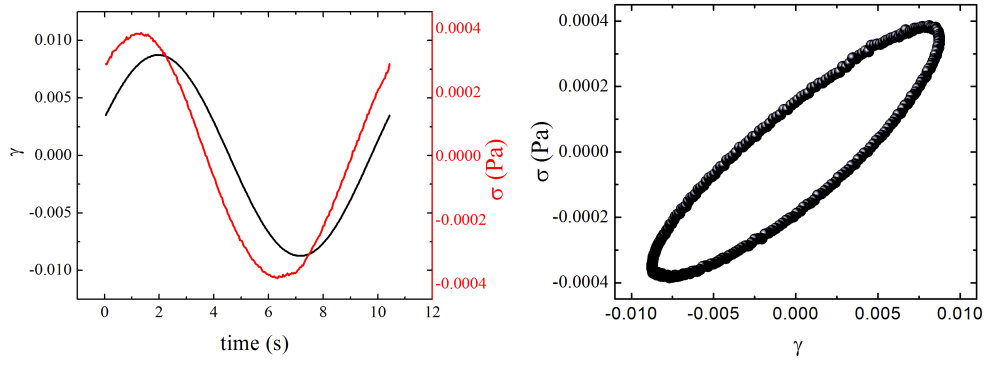


Figure 5.22: Case of PMMA(270k) monolayer using the bi-conical fixture at strain amplitude of $\gamma = 1\%$ and excitation frequency of $\omega_1/2\pi = 0.1$ Hz. Left panel: measurement of the stress versus time after an applied deformation. Right panel: Bowditch-Lissajous plot of the LAOS data.

5.2.7 Double wall ring fixture

As a last method to investigate the presence of even harmonics we used the double wall ring fixture in a DHR-3 rheometer. The layer was created in a Langmuir trough where the control of the surface pressure was feasible using a Wilhelmy plate made by paper. The dynamic frequency and strain sweeps are shown in Figure 5.23 showing a predominant elastic response in all strain and frequencies that were investigated.

Using the double wall ring fixture we obtained similar results with the bi-conical device with no even harmonics for all the investigated range of amplitude strains. The good resolution and accuracy of the DWR fixture could be responsible for the absence of the even harmonics, given that there are not asymmetries in this set up that are related with the measuring tools (i.e the ring).

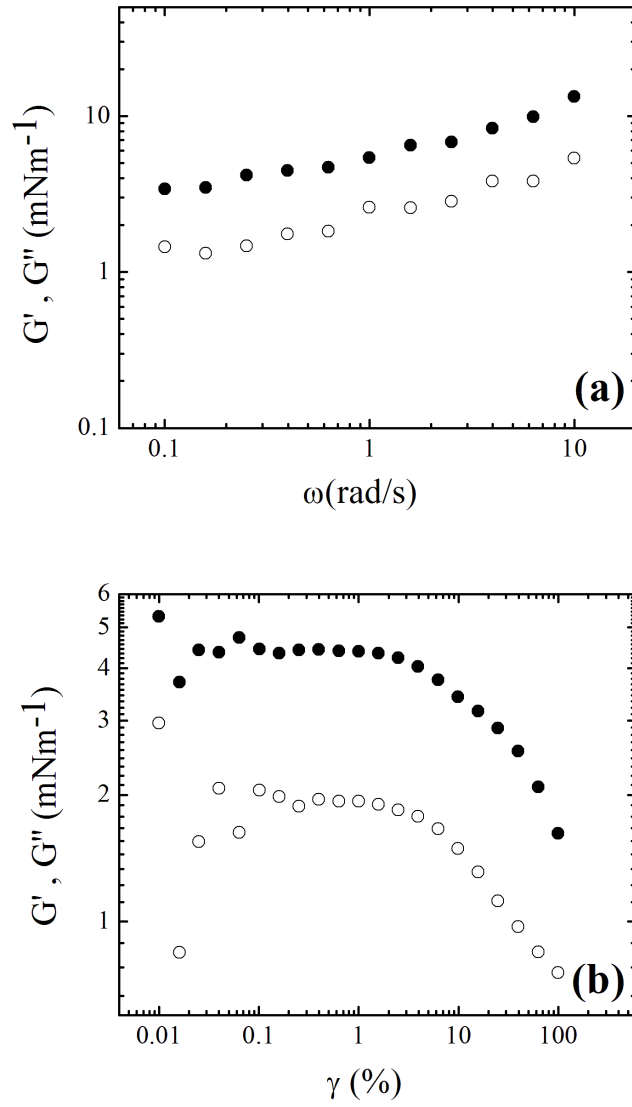


Figure 5.23: Linear and nonlinear rheology of PMMA (270k) using the double wall ring fixture a) dynamic frequency sweep measurement at $\gamma=0.1\%$ and b) dynamic strain sweep at $\omega=0.6$ rad/s . G' (closed symbols) and G'' (open symbols).

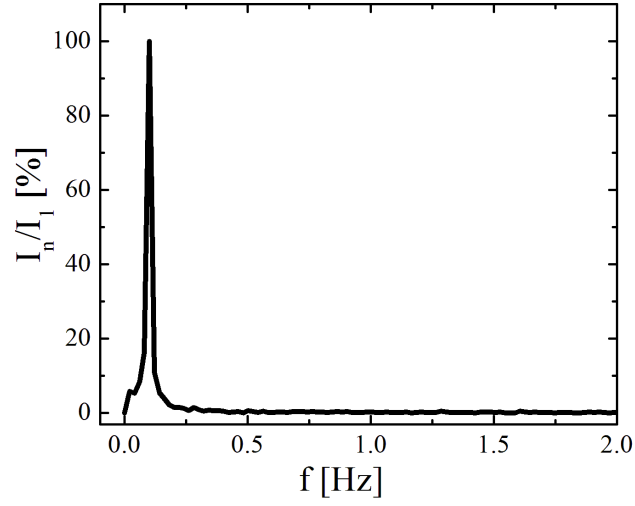


Figure 5.24: FT magnitude spectra of PMMA using the double wall ring fixture at strain amplitude of $\gamma = 1\%$. The excitation frequency was $\omega_1/2\pi = 0.1$ Hz.

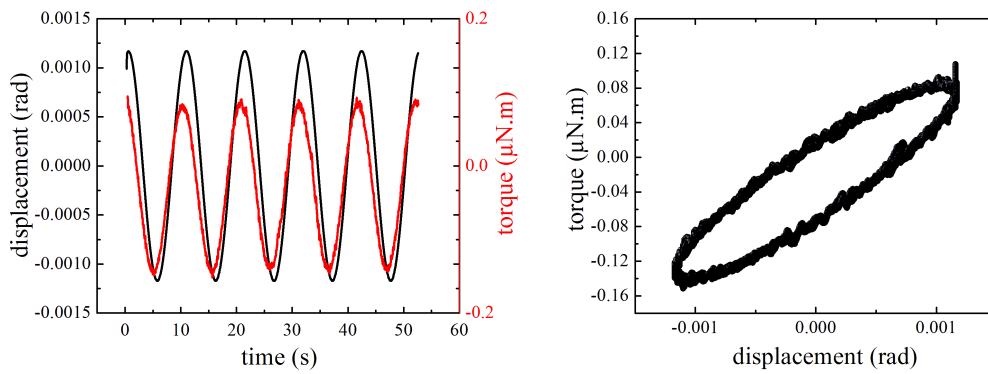


Figure 5.25: Case of PMMA(270k) monolayer using the double wall ring fixture at strain amplitude of $\gamma = 1\%$ and excitation frequency of $\omega_1/2\pi = 0.1$ Hz. Left panel: measurement of the torque versus time. Right panel: Bowditch-Lissajous plot of the LAOS data, plotting the torque versus the displacement.

5.3 Concluding remarks

In this chapter, we investigated the rheological response of linear PMMA at the air-water interface by means of large amplitude oscillatory shear (LAOS) and Fourier transform rheology (FT-rheology). Mainly, we focused on the presence of even harmonics in PMMA monolayers using a variety of different set ups and methods with main goal to find the reason of the existence of the higher harmonics and possibly reduce them or eliminate them. As a main technique we used the magnetic rod ISR where the adaptation of the measurement and control of the software allows performing non-linear FT rheological measurements at the air-water interface, including a user-defined oversampling mode to improve the signal-to-noise ratio. Starting from the magnetic rod ISR we saw that, by changing the size of the needle and the surface chemistry of both the needles and the channels, we do not suppress even harmonics, and by increasing the strain amplitudes an increase of the 2^{nd} harmonics intensity was detected for most of the cases. However, from the rheological measurements we saw that the PMMA layers exhibit a dominant elastic behaviour, and this result makes this sample an interesting candidate for the rheological analysis performed with the 2D-FT-rheology. Interestingly, no higher harmonics were observed using the bi-conal and the double wall ring fixture.

We could attribute the presence of even harmonics mostly to artifacts originating from the non-ideal shape of the magnetic rod and from the inhomogeneous surface geometry around the ends of the channel, where the magnetic rod resides. Based on the experimental results presented above our analysis allow to make general considerations about the limitations and potential improvements of the magnetic rod ISR technique. We can separate the asymmetric parameters into three major categories: (a) rheology-specific parameters, (b) instrument-specific parameters, and (c) sample-specific parameters. In particular these could be: (a) A camera with higher resolution to increase simultaneously the magnification and the field of view (providing access to a broader range of strain amplitudes), and with higher acquisition rate to reduce digitization artifacts and allowing a larger frequency range to be measured. (b) An improvement of the rheological probe with fully symmetric shape (to reduce even harmonics) and a surface coating that allows better adhesion of the sample to the probe (to prevent stick-slip). (c) Proper alignment of the magnetic needle. (d) Analysis of the subphase contribution (e)

Reduce the effect of the subphase contribution by increasing the bulk viscosity of the subphase (e.g. by using water-glycerol mixtures as polar subphases).

We note that the field of LAOS in bulk systems is rapidly evolving with approaches alternative to FT-rheology, which can offer various advantages and which would be of interest to be applied also to 2D systems at the air-water interface. When comparing the PMMA monolayer with the typical rheological behaviour of bulk polymers a stronger shear thinning effect can be found. This might be due to the interfacial arrangement of the polymer, which hints to a possible break-up of the surface layer into sheets that then can slide along each other. In 3D the nonlinear mechanical response of many simple bulk systems, such as linear homopolymer melts, is characterized by only a few harmonics in FTR analysis, usually only the 3rd, sometimes an additional 5th harmonic (Hyun *et al.* (2011)). In contrast, for other more complex bulk systems, such as emulsions, dispersions and gels, many higher harmonics (up to 151th) can be detected. As it is known from the literature, the even harmonics dominate when there is breakage of the symmetry of the stress response under oscillatory shear and such responses are attributed to the asymmetric parameters of the system (i.e. not perfectly straight needle). We conclude this chapter proposing that the best method to probe the interfacial rheology avoiding even harmonics that come from instrumental issues is the bi-conical device and the double wall ring fixture.

CHAPTER 6

BLOCK COPOLYMERS AT THE WATER-AIR INTERFACE

6.1 State of the art

At the air-water interface polymers can adopt different conformations such as brushes, mushroom-like or pancake-like morphologies. When polymers are grafted on a surface and the grafting density is high enough, polymer brushes are formed. The polymer brushes can mostly find applications in the stabilization of colloidal particles and micromechanics (Bumbu *et al.* (2004)). Moreover, films of copolymers can be used as model two-dimensional systems and as model membranes in the separation process (Anderson *et al.* (1991)). However, it has been noticed that it is not possible to form very dense polymer brushes because of the excluded volume interaction between the neighboring chains (Chen *et al.* (2015)). One important constraint concerning the formation of polymer brushes is given by their thickness: indeed only layers several nanometers thick can be formed because no disordered brush-like structure can exist on the length scale of few monomers (few angstrom). Diblocks and triblocks copolymers can form polymer layers at the air-water interface because of the twofold nature of their structure, built with both hydrophilic and hydrophobic groups.

Barentin *et al.* (1998) studied polymer brushes with telechelic polymers (PEO-C12 and C16) at the air-water interface investigating the relaxation mechanics and the desorption kinetics of the grafted chains, finding that the layer is stable ($\Pi \sim \text{constant}$) for low surface pressures, while for high compressions is unstable (observed decay of Π vs waiting time). They also studied the effect of the compression speed on the dynamics of the layers: the faster the compression the higher the density of the layers, the latter being less affected by polymer desorption. According to several theoretical studies (Johner and Joanny (1990)) and Ligoure and Leibler (1990)) concerning the adsorption kinetics, it has been shown that adsorption is slow and its characteristic time is increasing exponentially with the chemical potential of the brush. On the other hand

it has been shown that the characteristic time of the desorption mechanism is increasing exponentially with the grafting density (Wittmer *et al.* (1994) and Zajac and Chakrabarti (1994)).

For the polymer brushes at the air-water interface there are two regimes that can be distinguished according to the density of the layer: 1) the mushroom regime, which is the regime where the polymer coils do not overlap; 2) the brush regime where the polymers overlap and, while they are compressed, the chains stretch in order to avoid each other. The thickness of polymer brushes has been investigated in the literature using the neutron reflectivity technique (Penfold *et al.* (1990) and Bowers *et al.* (2001)). For diblock copolymers of PB-PEO with $M_W=60.000 \text{ g mol}^{-1}$ and $\sim 50 \text{ mol\%}$ PEO, it was found that, below the overlap concentration ($\Pi=0$) a two layer model describes well the molecular structure along the direction orthogonal to the air-water interface: the model has shown good agreement with the experimental data using only as fitting parameters the thickness of PB (d_{PB}) and PEO (d_{PEO}) layers giving $d_{PB}=3-7 \text{ \AA}$ and $d_{PEO}=6-11 \text{ \AA}$. In addition to that, as the pressure is increased, both the thicknesses increase, as expected for compressible layers, bringing for $\Pi=9 \text{ mNm}^{-1}$ the total thickness of the layer to 100 \AA . Also neutron reflectivity has been used to study the adsorption of spread polymers on polymer solutions and linear diblock copolymers at the air-water interface (Kent *et al.* (1992), Richards *et al.* (1994) and Dewhurst *et al.* (1998)).

Two other techniques that can characterize the diblock copolymer layers at the air-water interface are the X-ray specular reflectivity (XR) and the grazing incidence X-ray diffraction (GIXD). In a study of Hodges *et al.* (2006), monolayers of poly(oxyethylene)-poly(oxybutylene) were investigated with these techniques, showing a rapid thickening of the copolymer film at surface pressures above 7 mNm^{-1} . Complementary studies of the same system (PEO-PBO) have been performed by Hodges *et al.* (2008) using Brewster angle microscopy and scanning force microscopy (SFM): any localized ordering was detected consistently with the previous studies of X-ray.

The most commonly used hydrophilic head group for the formation of the polymeric layers in the literature is poly(ethylene oxide) that is a surface active material that can form monolayers at the air-water interface, despite the fact that it is a water soluble material (Shuler and Zisman (1970) and Kawaguchi *et al.* (1984)). Nowadays, PEO is used widely in pharmaceuticals because it is electro-statically neutral and biodegrad-

able. Some of the most popular hydrophobic tails include perfluoropolyether (Goedel *et al.* (1993)), polydimethylsiloxane (Elman *et al.* (1995)), polyisoprene (Stocco *et al.* (2011)) and polybutadiene (Bowers *et al.* (2001)). As it was shown from Kumaki (1986, 1988), the hydrophobic polymer must have low glass transition temperature in order to avoid the creation of hard particles at the air-water interface (e.g. polystyrene is not a good candidate for that purpose).

Polydimethylsiloxane (PDMS) is a water insoluble material, stable behaving as a liquid at the water surface. The surface pressure/area isotherms and the interfacial rheology of PDMS layers at the air-water interface have been investigated by (Fox *et al.* (1947); Hard and Neuman (1987); Garrett and Zisman (1970)). Mann and Langevin (1991) showed that pure PDMS at the air-water interface forms islands at low concentrations and that a homogeneous thin layer above a critical concentration is formed. Moreover, after a second critical concentration a thicker layer was detected. Lee *et al.* (1991) studied monolayers of PDMS at the air-water interface by means of neutron reflectivity showing that PDMS forms stable interfaces. Bernardini *et al.* (2010) used a theoretical approach via molecularly detailed self-consistent field (SCF) model and they found that PDMS at the air-water interface undergoes a layering transition (that was also observed experimentally). This phase transition from thin to thick layers is caused by long-range interaction forces between the surface and the polymer segments.

The monolayers of block copolymers can be formed at the air-water interface by dissolving firstly the polymer in a volatile organic solvent and subsequently by spreading the solution at the air-water interface. Using the compression-expansion barriers of a Langmuir trough the concentration of the polymer monolayer can be varied. The interfacial viscoelasticity of polymer layers is also a topic currently under investigation: we could expect that both elastic and viscous response are present for long enough chains and that, in absence of entanglements (low molecular weight), only a Newtonian-like response can be detected. Actually a power law dependence of the zero shear viscosity on the chain length has not been reported in the literature like for bulk systems. Nevertheless, the phenomenon of vitrification has been characterized for poly(butylstyrene) and (PS-PEO) layers at the air-water interface by Goedel *et al.* (1999) and Glagola *et al.* (2012) respectively.

In this chapter we study the polymeric layers of diblock and triblock copolymers

of PEO-PDMS at the air-water interface on a Langmuir trough by means of surface pressure/area isotherms and interfacial rheology using the magnetic rod ISR and the bi-conical device. The motivation of this study was to explore the effect of molecular composition and architecture of amphiphilic block copolymers (PEO-PDMS diblocks and triblocks) at the air-water interface on the thermodynamics of the layers. The structural information of these systems has been presented in Table 2.2. We emphasize here that our aim concerned the formation of functional and stable interfaces using these copolymers, knowing however that their rheological response is marginal because of their low molecular weight ($M_w=1600-7200 \text{ g mol}^{-1}$). This chapter includes three sections: the first describes the surface pressure/area measurements and the corresponding data analysis; in the second we present the interfacial rheology data; finally, in the last section, we summarize our results.

6.2 Surface Pressure Area Isotherms

The diblock and triblock copolymers that were used in this chapter are presented in Table 2.2. We dissolved an amount of 1 mg of copolymer in 1 ml of 2,2,4-Trimethylpentane ($\geq 99\%$) to create solutions of concentration of 1 mg/ml. Using a microliter syringe we spread dropwise the solution at the air-water interface of a Langmuir trough and we performed the surface pressure isotherms. In Figure 6.1 we present the compression-expansion cycles of all the series of PEO-PDMS copolymers as they were measured at the air-water interface of different molecular weights. In all cases we start the measurement by spreading an amount of solution $20-30 \mu\text{l}$, a relatively small amount in order to start the isotherm from the gas phase. As it is shown in the same figure, we increased the amount of spreading solution subsequently in order to reach high surface pressures, by creating a new monolayer each time. In Figure 6.1 the spreading volume of each isotherm is shown with the same colour. Interestingly, looking at each graph we observe that all the isotherms overlap in a very reproducible way and we obtain the full isotherms. Qualitatively, the behaviour of the isotherms is the same. All the surface pressure/area isotherms exhibit a fully reversible and stable layer deformation under compression- expansion cycles, where the copolymers remain at the air-water interface. However, in most cases it is not clear to distinguish the expansion isotherms because of their perfectly reversible behaviour.

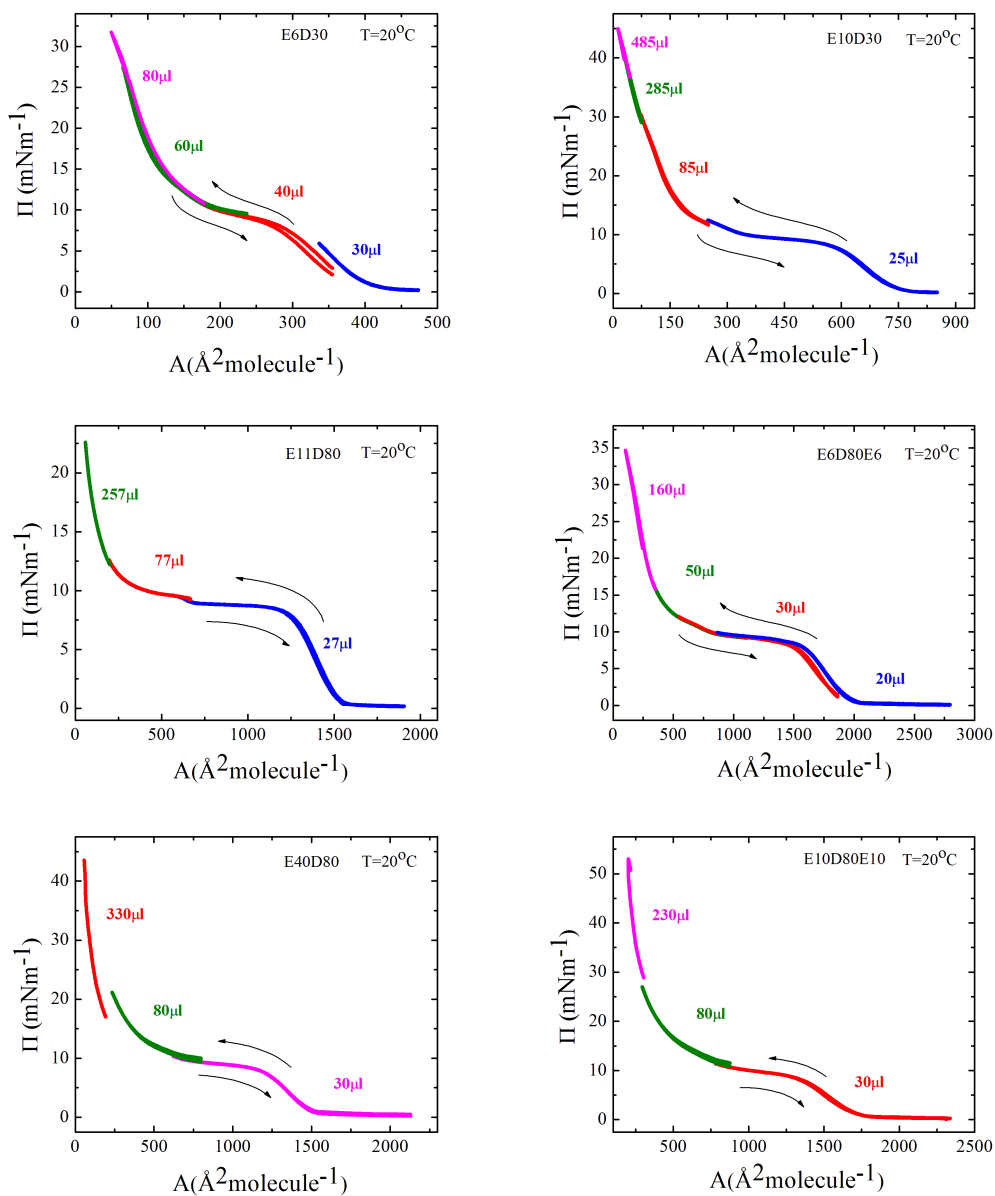


Figure 6.1: Surface pressure/area isotherms and compression-expansion cycles at 20°C for a) E6D30 ($M_w=1600 \text{ gmol}^{-1}$), b) E10D30 ($M_w=2400 \text{ gmol}^{-1}$), c) E11D80 ($M_w=5800 \text{ gmol}^{-1}$), d) E6D80E6 ($M_w=6300 \text{ gmol}^{-1}$), e) E40D80 ($M_w=7200 \text{ gmol}^{-1}$) and f) E10D80E10 ($M_w=7900 \text{ gmol}^{-1}$). These data are taken thanks to the collaboration with Mor Armon (University of Negev, Beer-Sheva, Israel).

In Figure 6.2 all the isotherms are replotted in the same graph for comparison reasons. Here we found that all isotherms reach a plateau at surface pressure of $\Pi=10$ mNm^{-1} . This plateau is characteristic for polydimethylsiloxane (PDMS) tail groups as it has been found by Lenk *et al.* (1994). After this plateau the isotherms show low compressibility (which is possibly linked to the transition at surface pressure $\Pi=10$ mNm^{-1}). The pressure increases rapidly by compressing more the monolayer and the polymer chains stretch with the direction perpendicular to the water. Here, a grafted polymer layer at the air-water interface is formed. According to Hahn *et al.* (1997), in the plateau region of the isotherm at $\Pi=9\sim10$ mNm^{-1} there is the coexistence of two different phases but it was not possible to discriminate between a layering transition or the formation of horizontal helices. According to a more recent study by Kim *et al.* (2008) random conformations of PDMS coils exist in the low concentration regime. Up to now, it is not clear what is the consistence of the plateau regime.

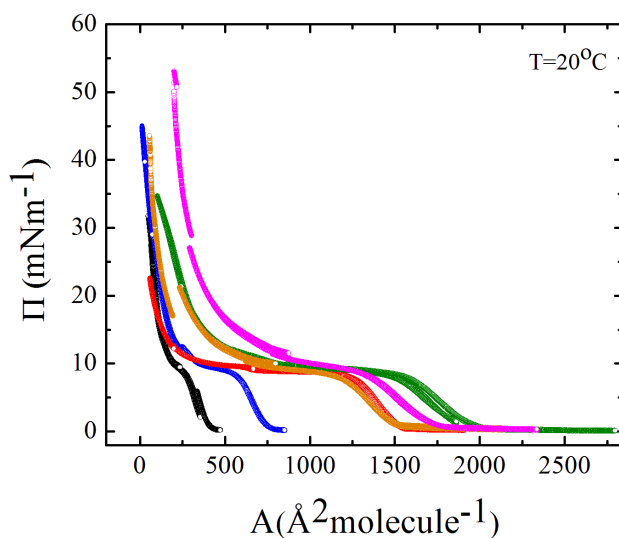


Figure 6.2: All the surface pressure/area isotherms at 20°C of E6D30 (black), E10D30 (blue), E11D80 (red), E6D80E6 (green), E40D80 (orange) and E10D80E10 (magenta).

Figure 6.3 depicts the surface pressure as a function of the fractional area (ϕ) occupied by PDMS. All the isotherms have been rescaled by the size of their structural unit A_0 , where $A_0=\pi R_F^2$. In the inset of Figure 6.3 we can see how A_0 is estimated, as it is the area at which we observe the increase of surface pressure. As it is shown, all the curves collapse on the same master curve. With this representation we can distinguish three regimes, the dilute regime (below $\Pi=1$ mNm^{-1}), the semidilute regime (up to the

plateau at $\Pi=10 \text{ mNm}^{-1}$) and the concentrated regime (beyond the plateau at $\Pi=10 \text{ mNm}^{-1}$).

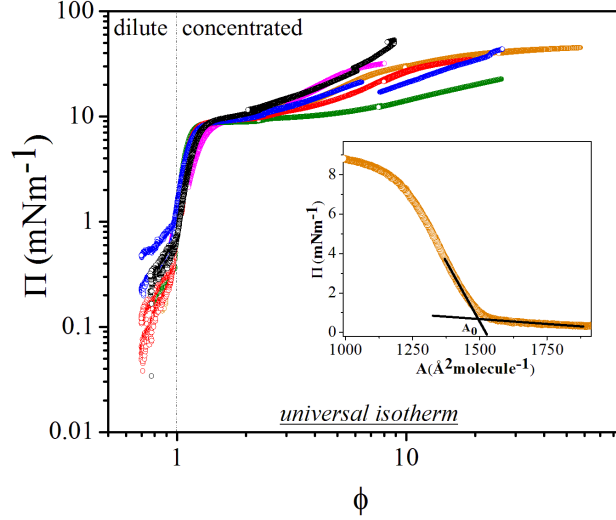


Figure 6.3: Surface pressure/area isotherms of Figure 6.2 replotted in terms of the fractional area occupied by the PDMS ($\phi=A_0/A$). The inset of this figure shows how A_0 is estimated.

In Figure 6.4 we describe the power law dependence of the Flory radii (R_F) as a function of the repeated units of the copolymer (N). The radius was estimated from the overlapping area that is shown in Figure 6.3, as $A_0=\pi R_F^2$. From the experimental data we found that the system scales as $R_F \sim N^\nu$, with $\nu=0.56 \pm 0.01$, that is characteristic for Langmuir films in poor solvent conditions. The same power law dependence has been found for layers of poly(methyl methacrylate) at the air-water interface (Maestro *et al.* (2009)).

Finally, we have calculated the theoretical values of the radius of gyration (R_g) of PDMS for number of PDMS repeated units $N_D=30$ and $N_D=80$. The R_g was calculated as $R_g^2=1/6(b^2N_D)$, where b is the statistical segment length of PDMS ($b=13\text{\AA}$). Given the limited number of molecular weight available, the scaling law is extracted only from two points, as it is shown from the left panel of Figure 6.5 and the radius of gyration scales as $R_g \sim N_D^{0.5}$. In order to compare, in the right panel of the Figure 6.5 we have plotted the experimental values of Flory radii of the diblocks as a function of the repeated units of the PDMS.

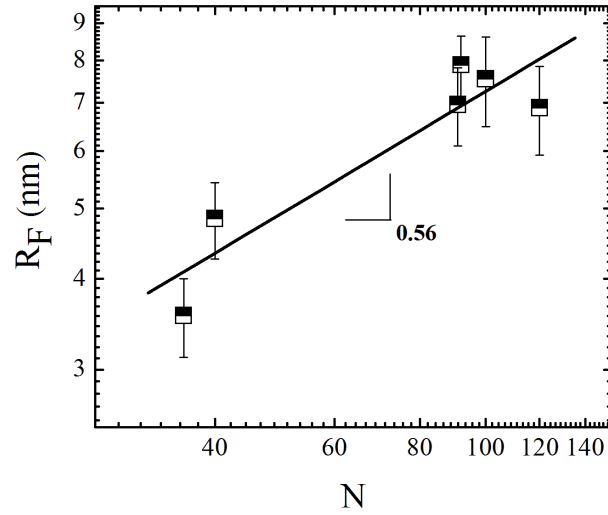


Figure 6.4: Flory radii versus total number of repeated units (N) describing by a scaling law.

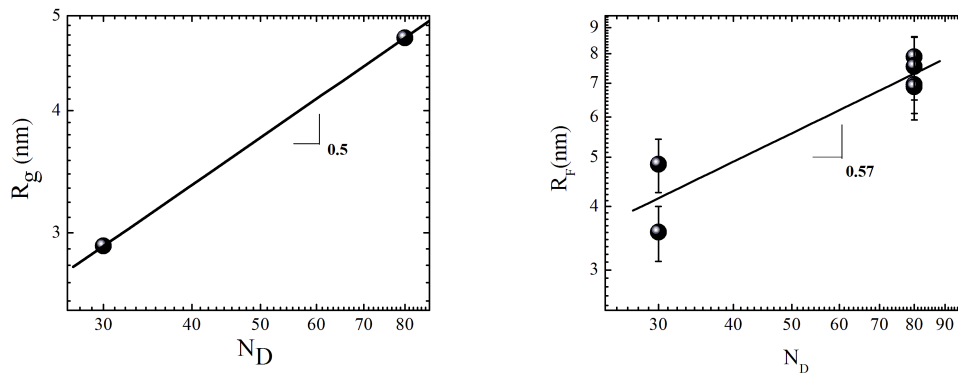


Figure 6.5: Left panel: Theoretical values of radii of gyration as a function of the PDMS repeated units (N_D). Right panel: Experimental Flory radii versus N_D of the diblock copolymers.

6.3 Interfacial Rheology

The interfacial rheology of the diblock and triblock copolymer layers was firstly investigated at the air-water interface using the magnetic rod ISR. The rod displacement measured for these layers was close to the resolution limit of the instrument, supporting the viscous-like nature of the layers. However, we used the bi-conical fixture in a rheometer in order to perform tests at different torques and to have a better insight into the viscoelastic response of the block copolymers. In Figure 6.6 we show the torque as a function of time for different shear rates for the diblock E6D30. In this graph we indicate with the horizontal black line the torque limit of the instrument. For most of the shear rates investigated the displacement lays below the resolution limit of the instrument making the data not reliable.

In Figure 6.7 we show a dynamic time sweep measurement of E6D30 performed at shear rate 2s^{-1} , $\omega=0.1\text{Hz}$ and $\gamma=0.1\%$, where the displacement lays above the resolution limit of the instrument. The values of the dynamic moduli, being scattered, do not indicate any particular trend and the elastic and/or the viscous behaviour of the monolayer could not be discerned. In all the rheological measurements performed by using the bi-conical device we used an initial area/molecule, quantifying the molecular packing at the interface, that was 40 times lower than that employed in the Langmuir trough experiments. Despite the high concentration, we could not obtain reliable data with the diblock copolymers.

Given our results, it is reasonable to increase the size of the hydrophobic chains of the diblock copolymers of PEO-PDMS to bring the response of the layer within the measurable range of torques. More specifically, good candidates would be PEO-PDMS copolymers with molecular weights $M_W > 40.000 \text{ g mol}^{-1}$.

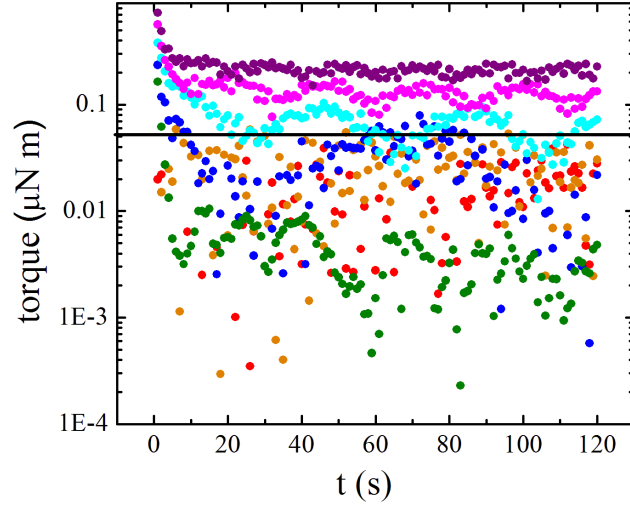


Figure 6.6: Interfacial rheology measurements of E6D30. Left panel: torque versus time for different shear rates. 0.05s^{-1} (red), 0.1s^{-1} (orange), 0.5s^{-1} (blue), 1s^{-1} (cyan), 1.5s^{-1} (magenta), 2s^{-1} (purple) and 2.5s^{-1} (green).

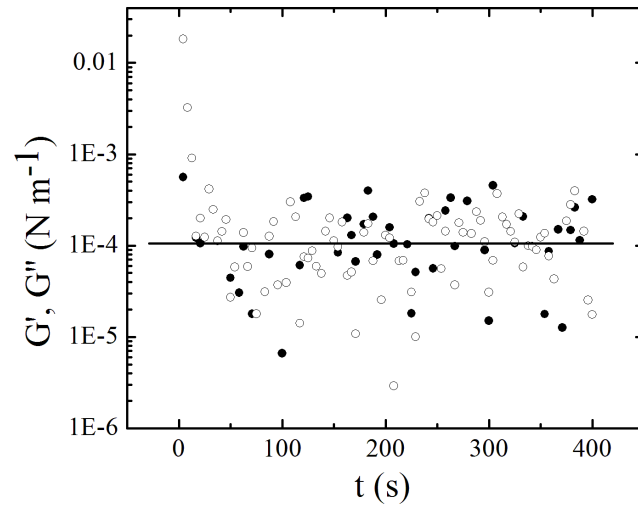


Figure 6.7: Interfacial time sweep data of E6E30 at $\omega=0.1\text{Hz}$ and $\gamma=0.1\%$. G' (closed symbols) G'' (open symbols).

6.4 Concluding remarks

In this chapter we investigated the formation of Langmuir monolayers from block copolymers of poly(ethyleneoxy) and poly(dimethylsiloxane) with molecular weights of 1600-7900 g mol^{-1} . For all the different molecular weights we observed the characteristic PDMS transition at $\Pi=10 \text{ mNm}^{-1}$. The molecular configurations related to this transition still remain a debate in the literature. Interestingly, these transitions do not depend on the molecular weight of the copolymer and are related to the area per monomer of the PDMS. PDMS is an end-functional group of the copolymer that is a very interesting and unique material in the studies of Langmuir monolayers because it can interact with the aqueous phase. Upon compressing the monolayers beyond the transition, the PDMS remains in the helical configuration during all the compression. In all of the investigated cases no collapse was detected.

According to previous studies (Fox *et al.* (1947)), in the gas-phase where the surface pressure is zero, the molecules of PDMS are lying flat because of the interaction of the oxygen atoms of the backbone with the aqueous phase. Subsequently, when the surface pressure starts to escape from zero and increase, according to Noll *et al.* (1971) a planar zigzag structure is formed. The surface pressure plateau at $\Pi=10 \text{ mNm}^{-1}$ represents the coexistence of two phases mainly constituted by molecules in the helical conformation. Interestingly, we observed that by increasing the molecular weight of the copolymer the plateau increases. Finally, for the last region (beyond the plateau), Fox *et al.* (1947) suggested that the layer becomes solid at surface pressures higher than 10 mNm^{-1} .

In this chapter it is shown that PEO-PDMS copolymers form extremely reversible and stable monolayers at the air-water interface showing no hysteresis. As a result, we do not lose any material during compression-expansion isotherms. We also obtained a power law behaviour of the Flory radii as a function of the number of repeated units and we found that the system scales as $R_F \sim N^\nu$, with $\nu=0.56 \pm 0.01$, that is characteristic for Langmuir films in poor solvent conditions.

Regarding the rheological behaviour of the block copolymers of PEO-PDMS, in the bulk PDMS is a highly viscous material. From interfacial rheology measurements using the magnetic rod interfacial stress rheometer and the bi-conical device in a rheometer we obtained extremely weak signal showing that we were close to the resolu-

tion limit of the instrument. However, we increased the concentration of the spreading solution, moving beyond the highest surface pressure that was shown from the surface pressure/area isotherms and still we saw a very weak response of the multilayer.

CHAPTER 7

CONCLUSIONS AND PERSPECTIVES

We have investigated the structural and rheological properties of molecular systems at the air-water interface, exploring the tunability of film properties, promising for specific technological and biological applications. We used a series of semifluorinated alkane molecules, linear, branched and azobenzene containing systems. All systems investigated revealed the importance of the microstructural details of the film components driving the rheological response of the layers and the interplay between structure and mechanical response. Furthermore, we chose as model systems PMMA homopolymers, that form elastic monolayers at the air-water interface in order to study the LAOS rheology. Finally, block copolymers of PEO-PDMS were studied at the air-water interface. PMMA and PEO-PDMS block copolymers are different than semifluorinated alkanes because they bound to the aqueous subphase.

Exploring the behaviour of semifluorinated alkanes we found a rich tunability in terms of structure and viscoelasticity at the air-water interface. Starting from a reference linear and symmetric molecule, F12H12, we observed the formation of 30 nm micelles that showed a fully reversible layer formation at the air-water interface. The micelles, interestingly, form monolayers that show a ductile-like behaviour, that becomes more and more important as the surface pressure increases. Keeping the same length of the fluorinated and alkane parts of F12H12, small groups of phenyls (F12-phenyl-H12) and two oxygens (F12-O-phenyl-O-H12) were inserted in between the chains. The monolayers of F12-O-phenyl-O-H12 exhibit fully reversible layers deformations with "lying flat" structures while the F12-phenyl-H12 layers show an irreversible layer deformation. In these two cases, where there is a chemical group between the fluorocarbon and the hydrocarbon chains, the rheological response was similar to a Newtonian fluid.

Branched architectures of semifluorinated alkanes led to the formation of stiff and brittle-like monolayers. Two branched systems were used, bis(F11H1-core-H12) and 2F12-core-2H12, both exhibited an irreversible layer deformation, with a hysteresis. Neutron reflectivity analysis revealed the structure of the layers: the molecule

backbone is perpendicular to the interfacial plane with the fluorocarbon head pointing towards the air. The maximum linear viscoelastic regime that was measured for these layers was up to 0.1 %. However, comparing the two systems at low surface pressure, bis(F11H1-core-H12) layers exhibit (one order of magnitude) smaller interfacial modulus than 2F12-core-2H12 layers. The higher stiffness of 2F12-core-2H12 is attributed to the absence of oxygen molecules, that enhance the fluidicity of the systems. As a last case, we examined the layers of a hydrogenated analogue, 2H-core-2H12 that showed viscous-like response at the air-water interface, a fully reversible layer deformation with a structural model where the aromatic core is in contact with the aqueous phase and their alkane chains are pointing towards the air.

The effect of the external stimulus of light to semifluorinated azobenzene derivatives was also studied in this thesis. A fluorinated (F8-azo-H8) and a hydrogenated analogue (H8-azo-H8) which undergo trans-cis isomerization upon irradiation were examined at the air-water interface. The layers of F8-azo-H8 showed an interesting transition from ordered to disorder structure after the UV irradiation. When the molecules are in the trans conformation they occupy a molecular area 3 times smaller than their analogue in cis conformation. For both cases, under UV light the surface pressure increases and this phenomenon is followed by a large drop (one order of magnitude) of the interfacial storage modulus. The layers showed reversible deformations under compression-expansion cycles with very small hysteresis for trans conformation, for cis conformations and for mixtures of the cis and trans (under visible light).

The non-linear rheology (LAOS) of PMMA monolayers was studied with Fourier transform analysis. PMMA layers exhibit a dominant elastic behaviour, and this finding makes them nice candidates for the rheological analysis with the 2D-FT-rheology. We investigated the presence of even harmonics using different methodologies with the magnetic rod ISR, the bi-conical fixture and the double wall ring fixture. Using the magnetic rod ISR we measured the non-linear rheology of PMMA with channels of different sizes (aspect ratio of channel width to rod diameter $\lambda=18$ and $\lambda=14$). In order to homogenize the contact of the needle with the water we built PMMA-grafted glassy needles and finally we modified the channel by grafting it with PMMA as well. In all the previous cases the results indicated the presence of even harmonics whose amplitude increase with the strain amplitude. Interestingly, no higher harmonics were observed using the bi-conal and the double wall ring fixture. We attribute the presence

of even harmonics to artifacts originating from the non-ideal shape of the magnetic rod and the not perfectly straight needle at the interface and to the inhomogeneous surface coating of the channel and the needle. Finally, we can attribute the presence of even harmonics to a strong subphase contribution. In order to reduce the effect of the subphase contribution we should increase the bulk viscosity of the subphase, for example by using mixtures of water-glycerol as a subphase.

In addition to that, block copolymers of poly(ethyleneoxy) and poly(dimethylsiloxane) with molecular weights of 1600-7900 g mol^{-1} were studied at the air-water interface. A key finding of this work was the reproducible characteristic PDMS transition at $\Pi=10 \text{ mNm}^{-1}$ for all the different molecular weights that were examined. We show that the pressure plateau corresponding to the two-phase coexistence region increases by increasing the molecular weight of the copolymers. PEO-PDMS copolymers are good candidates for technological applications because they form extremely reversible and stable monolayers showing no hysteresis during compression-expansion surface pressure isotherms. Finally, we obtained a power law behaviour of the Flory radii as a function of the number of repeated units and we found that the system scales as $R_F \sim N^\nu$, with $\nu=0.56 \pm 0.01$, that is characteristic for Langmuir films in poor solvent conditions. The interfacial rheology of these systems showed very weak viscous response, close to the resolution limit of the instrument.

All our results have evidenced the molecular guidelines to tailor the linear and nonlinear viscoelastic properties of molecular and polymeric layers. We showed that: 1) the insertion (removal) of aromatic rings in the SFA structures radically alter the dynamics of the films; 2) that passing from linear to branched molecules sharing the same chemistry, the elastic modulus increases while the nonlinear response becomes less ductile-like; 3) comparing fluorinated and hydrogenated molecules sharing the same structure/topology, the fluorine atoms have a strong reinforcement effect on the layers, making solid-like the film response in some cases; 4) the modern and most popular interfacial rheology techniques have severe limitations in terms of torque resolutions and dynamic modulus range that can be investigated. On the other hand much work must be done still to eliminate the presence of even harmonics in ISR.

A challenge for future work includes the improvement of the current mini trough to measure surface pressure/area isotherms and interfacial rheology at oil/water inter-

faces. Moreover, in order to complete our research activity of PEO-PDMS copolymers, we have to examine block copolymers with higher molecular weights, possibly $M_W > 40.000 \text{ g mol}^{-1}$. In addition to that, neutron reflectivity measurements must be performed to better define the structure of the block copolymers at the air-water interface.

Due to complexity and limitations of the magnetic rod interfacial stress rheometer, still controversial questions remain that have to be clarified and improvements to be done. Given to the relatively high values of Boussinesq number and the high sensitivity of the magnetic rod interfacial stress rheometer, it can be used to measure mainly weak interfaces (low interfacial moduli limit of 10^{-3} mNm^{-1}). The highest resolution limit of the magnetic rod ISR in this thesis was observed for interfacial moduli of almost 50 mNm^{-1} . For stiffer samples ($G' > 50 \text{ mNm}^{-1}$) the current force of the magnetic field is not enough to set in movement the magnetic rod, consequently a stronger magnetic field could resolve this problem. Future direction of our improvements include the construction of magnetic rods with higher sensitivity. It is worth to mention that the construction of a perfect cylindric rod could reduce errors related to the subphase contribution during the measurement. Further improvement of the current set up includes the construction of channel geometry that will allow measurements of higher strain amplitude range. Finally, a potential modification of the camera resolution and the image acquisition speed should be taken into consideration to improve the optical detection system.

APPENDIX A

NEEDLE CHARACTERIZATION

In this appendix we present the characterization of the needles that were used in the magnetic rod interfacial stress rheometer. Chapter 2 describes the exact calibration method that was performed in order to characterize the needles. In Figure A.2 we demonstrate the characterization of the metallic needles and in Figure A.3 the characterization of the glassy needles. For each needle we present the following characteristics:

- The name,
- the mass (m) in mg,
- the length (L) in mm,
- the radius (α) in μm ,
- the density (ρ) in kgm^{-3} ,
- the calibration constant (k) in NAmp^{-1} ,
- the amplitude ratio (AR) in mmN^{-1} , described in equation 2.3 and
- the Bond number (Bd).

The Bond number, Bd, represents the ratio of buoyancy forces over surface forces and it is calculated as it is shown in equation A.1:

$$Bd = \frac{g(\rho_{rod} - \rho_{subphase})\pi\alpha^2}{2\gamma} \quad (\text{A.1})$$

where γ refers to the interfacial tension of the water ($\gamma=72\text{mNm}^{-1}$).

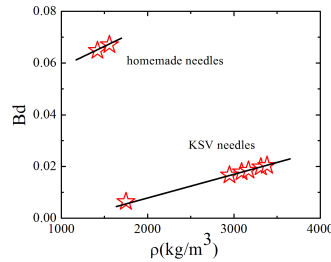


Figure A.1: Comparison between the performance of homemade glassy needles and glassy needles bought from KSV.

METALLIC NEEDLES

Name	Mass (mg)	Length (mm)	α (μm)	ρ (kg/m ³)	k(N/Amp)	AR (m/mN)	Bond Number
Tarja	40.5		50	250	4125.42	3.40E-04	6.52
Floor	99.5		38	350	6804.03	1.31E-04	97.9
Simone	68.4		55	250	6333.97	2.94E-03	5.57
Sharon	51.6		51	250	5153.03	1.90E-03	1.91
Charlotte	65.5		51	250	6541.15	1.08E-04	75.5
Epica	40.2		50	250	4094.86	8.84E-05	40.99
Kamelot	41.9		50	200	6668.79	9.87E-05	99.2
Anneke	53.3		33	300	5712.6	2.64E-04	50.98
Doro	67.5		55	250	6250.63	5.83E-03	1.54
Cristina	40.1		50	200	6382.3	1.46E-04	120.19
Liv	21.5		22	200	7777.12	1.75E-04	20.03

Figure A.2: Characterization of metallic needles.

GLASSY NEEDLES

Name	Mass (mg)	Length (mm)	α (μm)	ρ (kg/m ³)	k (N/Amp)	AR (m/mN)	Bond Number
KSVB	16.6	39.9	200	3310.839569	4.52E-04	8.55	0.019782
KSVC	16.5	42.52	200	3088.116195	5.47E-04	9.37	0.017876
KSVD	17.3	40.7	200	3382.631108	1.40E-03	0.83	0.020397
KSVF	16.5	41.45	200	3167.833549	8.88E-04	1.74	0.018558
KSVG	13.6	36.7	200	2949.0069	5.36E-04	3.83	0.016685
RVS	10	45.5	200	1749.007001	noisy signal	-	0.006412
C-SH-MIN	204.6	63.5	850	1419.570575	4.81E-04	8.81	0.064876
C-MIN	178.9	65	750	1557.533488	1.99E-04	2.94	0.067118

Figure A.3: Characterization of glassy needles.

APPENDIX B

MINI TROUGH:WATER-OIL INTERFACE

The challenge of this study was to build a Langmuir trough set up to measure surface pressure/area isotherms at oil-water interfaces. Having already a commercial Langmuir trough to measure water-air interfaces a similar mini trough set up was built that is depicted in Figure B.1. The new mini trough is 17 times smaller than the commercial trough with higher walls comparing with the commercial trough. The mini trough and the barriers are made by Polyoxymethylene (POM). The barriers are mounted on the base of the commercial trough and a Wilhelmy plate made by platinum is used to measure the surface pressure. The Wilhelmy plate is positioned 90 °rotated in respect to its position in the commercial trough in order to fit into the new trough. In Figure B.2 we have reproduced palmitic acid surface pressure isotherms at the water-air interface using the commercial trough and the mini trough.

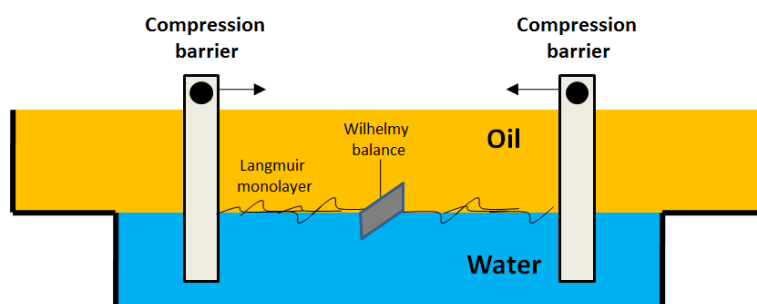


Figure B.1: Mini Langmuir trough to measure oil-water interfaces.

The challenges during the operation/testing of the mini trough were the following:

- The right positioning of the barriers in order to exhibit a homogeneous compression.
- Reproducibility of surface-pressure isotherms at the water-air interface (consistency between the commercial trough and the mini trough).
- Optimization of the conditions in order to measure oil/water interfaces (right positioning of the Wilhelmy plate merged into the oil phase).

The triblock copolymer of PEO-PDMS, E10D80E10, was tried to be measured at the isooctane-water interface using the mini trough. As it is shown in Figure B.3,

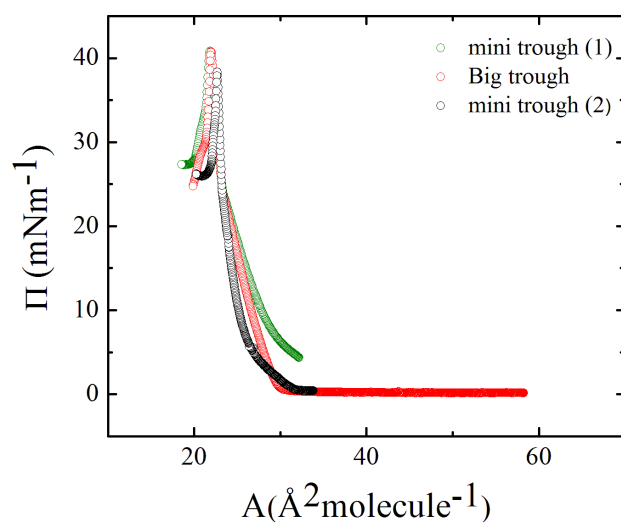


Figure B.2: Surface pressure/area isotherms of palmitic acid at the water-air interface at 20°C using the big Langmuir trough and the new mini trough.

by spreading different amounts of material we were not able to detect an increase of the surface pressure during compression. This can be attributed possibly to the loss of the molecules in the oily phase. Subsequently, polystyrene particles of diameter 200 nm were spread at the air-water and isooctane-water interface. The preliminary results are presented in Figure B.4, showing an increase of the surface pressure during compression.

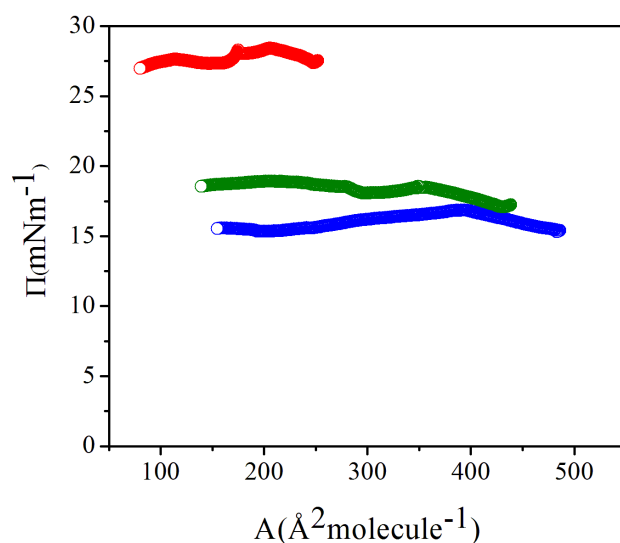


Figure B.3: Surface pressure/area isotherms of E10D80E10 at the isooctane-water interface at 20°C using the mini Langmuir trough. Spreading volume 9 μl (blue data), 10 μl (green data) and 18 μl (red data).

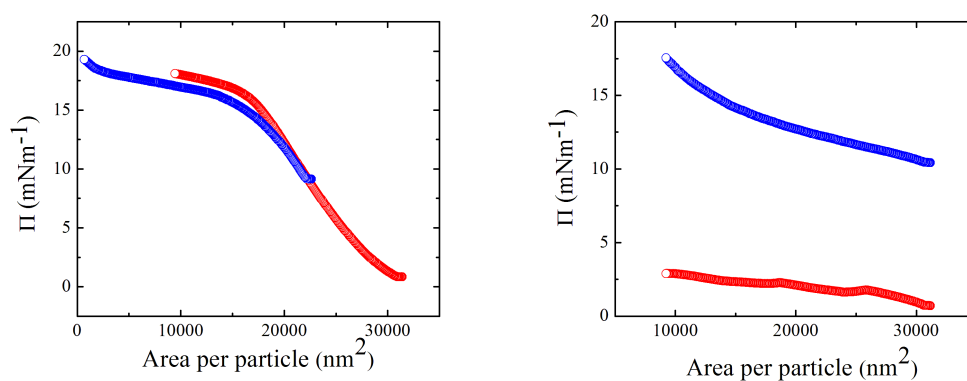


Figure B.4: Surface pressure/area isotherms of PS particles. Left panel: at the water-air interface and Right panel: at the isooctane-water interface at 20°C using the mini Langmuir trough. Spreading volume 5 μl (blue data) and 3 μl (red data).

APPENDIX C

NON-CONVERGENT MODELS IN NEUTRON REFLECTIVITY

Different possible packing models were considered by variation of the structural parameters (number of layers, and for each layer, layer thickness, scattering length density and surface roughness) and the scattering density profile was calculated as it is described in equation 3.1 and 3.2. The procedure of fitting can be described as follows: For each fit, three cases of layers are tried (1 layer, 2 layers and 3 layers). The scattering length density of each layer is calculated using the NIST's scattering length density calculator assuming the density of the layer to be the bulk density of each material. For each case, we fix the following parameters: number of layers, the scattering length density, thickness and roughness according to the orientation of the molecules. In a second step in case of non-convergence we leave the parameters of thickness and roughness free for minimization. In this appendix we present the fits of models where the fluorocarbons are pointing towards the air (CF-UP) in a perpendicular orientation. The semifluorinated alkane systems that showed non-convergence with the CF-UP models were F12-phenyl-H12, F12-O-phenyl-O-H12 and the azobenzene containing semifluorinated alkane systems.

In Figure C.1a the CF-UP fit of F12-phenyl-H12 at surface pressure 2 mNm^{-1} is presented. The structural model is depicted in the inset of the figure. Three layers were taken into account, the first (on contact with the aqueous phase) consists of the alkane chain (abbreviated as H12) with thickness of 17 \AA , the second layer consists of the phenyl ring with thickness 5 \AA and the third includes the fluorocarbon chains (F12) with thickness of 17 \AA . The same structural model has been considered for F12-O-phenyl-O-H12 at surface pressure of 2 mNm^{-1} and its non-convergent fit is presented in Figure C.1b. Finally, the F8-azo-H8 in the dark also at surface pressure 2 mNm^{-1} exhibits non-convergence with the CF-UP model as it can be seen in Figure C.1c.

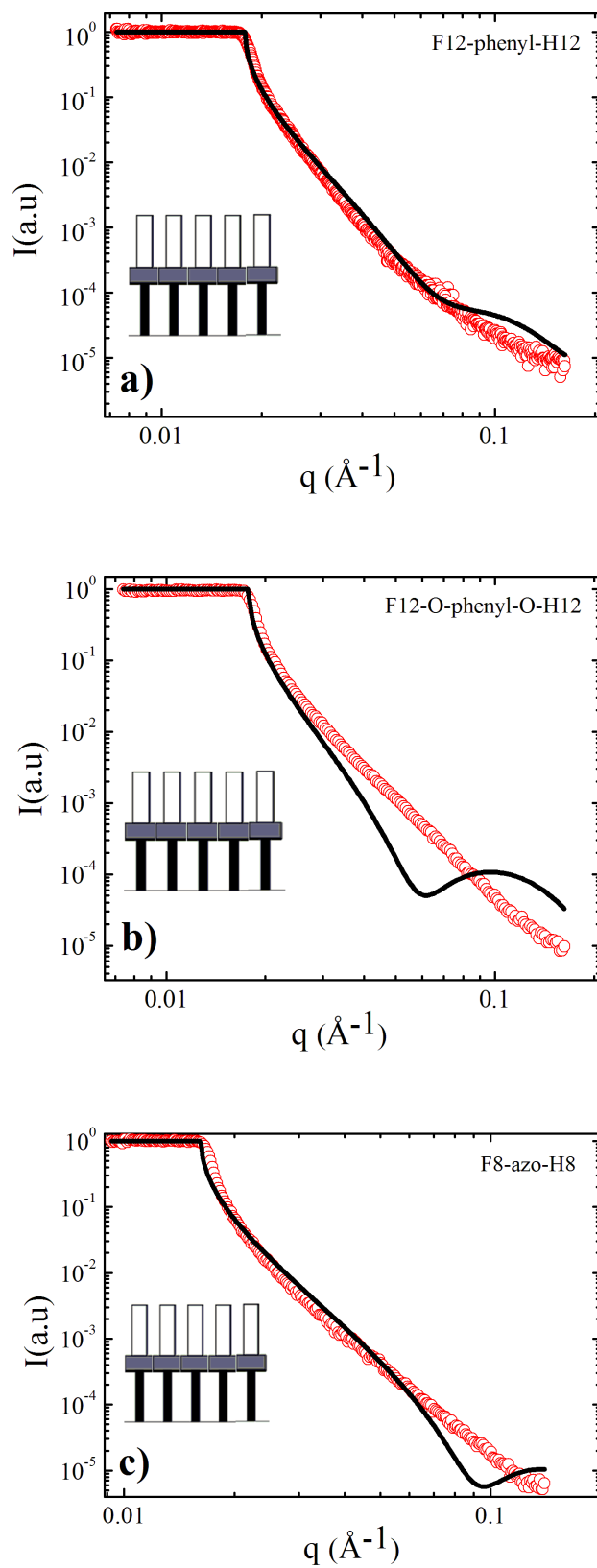


Figure C.1: Extra neutron reflectivity data (red symbols) and fits (black lines) where CF-UP model structures have been considered for a) F12-phenyl-H12, b) F12-O-phenyl-O-H12 and c) F8-azo-H8 under dark. In the inset a schematic representation of the model is presented with the alkane parts to be drawn as black segments and the fluorocarbon parts as white segments.

APPENDIX D

Fourier Transform magnitude spectra

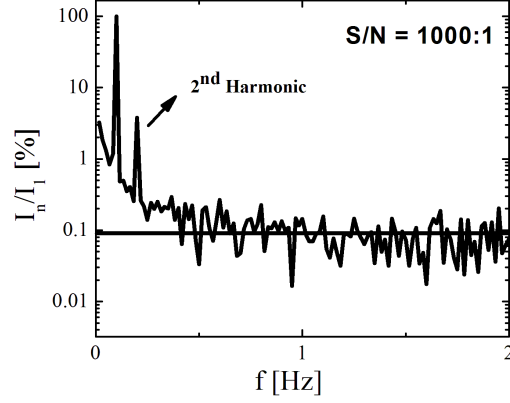


Figure D.1: Log-Linear plot of FT magnitude spectra of PMMA using the ISR with channel width 0.7 cm at strain amplitude of $\gamma = 1\%$. The excitation frequency was $\omega_1/2\pi = 0.1$ Hz.

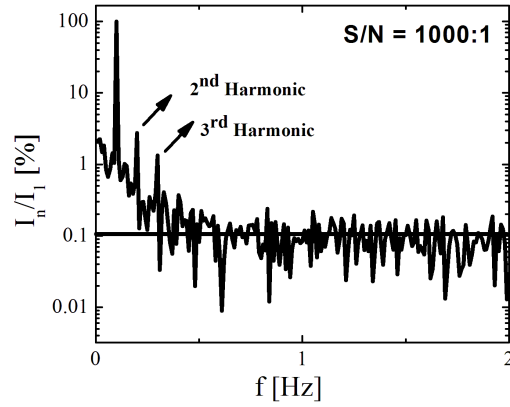


Figure D.2: Log-Linear plot of FT magnitude spectra of PMMA using the ISR with a PMMA-grafted glassy needle at strain amplitude of $\gamma = 1\%$. The excitation frequency was $\omega_1/2\pi = 0.1$ Hz.

REFERENCES

1. **Anderson, M. R., B. R. Mattes, H. Reiss, and R. B. Kaner** (1991). Conjugated polymer-films for gas separations. *Science*, **252**(5011), 1412–1415.
2. **Bardin, L., M. C. Faure, E. J. M. Filipe, P. Fontaine, and M. Goldmann** (2010). Highly organized crystalline monolayer of a semi-fluorinated alkane on a solid substrate obtained by spin-coating. *Thin Solid Films*, **519**(1), 414–416.
3. **Bardin, L., M. C. Faure, D. Lirnagne, C. Chevallard, O. Konovalov, E. J. M. Filipe, G. Waton, M. P. Krafft, M. Goldmann, and P. Fontaine** (2011). Long-range nanometer-scale organization of semifluorinated alkane monolayers at the air/water interface. *Langmuir*, **27**(22), 13497–13505.
4. **Barentin, C., P. Muller, and J. F. Joanny** (1998). Polymer brushes formed by end-capped poly(ethylene oxide) (peo) at the air-water interface. *Macromolecules*, **31**(7), 2198–2211.
5. **Bernardini, C., S. D. Stoyanov, M. A. C. Stuart, L. N. Arnaudov, and F. A. M. Leermakers** (2010). Polymers at the water/air interface, surface pressure isotherms, and molecularly detailed modeling. *Langmuir*, **26**(14), 11850–11861.
6. **Bhaskar, A. ()**. The effective poisson ratio of random cellular matter having bending dominated architecture. *Europhysics Letters*, **87**, 18004 p1–18004 p6.
7. **Blodgett, K.** (1939). Use of interface to extinguish reflection of light from glass. *Physical Review*, **55**, 391.
8. **Bowers, J., A. Zarbakhsh, J. R. P. Webster, L. R. Hutchings, and R. W. Richards** (2001). Structure of a spread film of a polybutadiene-poly(ethylene oxide) linear diblock copolymer at the air-water interface as determined by neutron reflectometry. *Langmuir*, **17**(1), 131–139.
9. **Broniatowski, M. and P. Dynarowicz-Latka** (2008). Semifluorinated alkanes - primitive surfactants of fascinating properties. *Advances in Colloid and Interface Science*, **138**(2), 63–83.
10. **Brooks, C. F., G. G. Fuller, C. W. Frank, and C. R. Robertson** (1999). An interfacial stress rheometer to study rheological transitions in monolayers at the air-water interface. *Langmuir*, **15**(7), 2450–2459.
11. **Bumbu, G. G., G. Kircher, M. Wolkenhauer, R. Berger, and J. S. Gutmann** (2004). Synthesis and characterization of polymer brushes on micromechanical cantilevers. *Macromolecular Chemistry and Physics*, **205**(13), 1713–1720.
12. **Caldwell, W. B., D. J. Campbell, K. M. Chen, B. R. Herr, C. A. Mirkin, A. Malik, M. K. Durbin, P. Dutta, and K. G. Huang** (1995). A highly ordered self-assembled monolayer film of an azobenzenealkanethiol on au(111) - electrochemical properties and structural characterization by synchrotron in-plane x-ray-diffraction, atomic-force

- microscopy, and surface-enhanced raman-spectroscopy. *Journal of the American Chemical Society*, **117**(22), 6071–6082.
13. **Capan, I., R. Capan, T. Tanrisever, and S. Can** (2005). Poly(methyl methacrylate) monolayers at the air-water interface. *Materials Letters*, **59**(19-20), 2468–2471.
 14. **Carotenuto, C., M. Grosso, and P. L. Maffettone** (2008). Fourier transform rheology of dilute immiscible polymer blends: A novel procedure to probe blend morphology. *Macromolecules*, **41**(12), 4492–4500.
 15. **Chen, C., P. Tang, F. Qiu, and A.-C. Shi** (2015). Excluded volume effects in compressed polymer brushes: A density functional theory. *Journal of Chemical Physics*, **142**(12), 124904 1–124904 10.
 16. **Chevallier, E., A. Mamane, H. A. Stone, C. Tribet, F. Lequeux, and C. Monteux** (2011). Pumping-out photo-surfactants from an air-water interface using light. *Soft Matter*, **7**(17), 7866–7874.
 17. **Chevallier, E., C. Monteux, F. Lequeux, and C. Tribet** (2012). Photofoams: Remote control of foam destabilization by exposure to light using an azobenzene surfactant. *Langmuir*, **28**(5), 2308–2312.
 18. **Cicciarelli, B. A., J. A. Elia, T. A. Hatton, and K. A. Smith** (2007a). Temperature dependence of aggregation and dynamic surface tension in a photoresponsive surfactant system. *Langmuir*, **23**(16), 8323–8330.
 19. **Cicciarelli, B. A., T. A. Hatton, and K. A. Smith** (2007b). Dynamic surface tension behavior in a photoresponsive surfactant system. *Langmuir*, **23**(9), 4753–4764.
 20. **Clark, C. G., G. A. Floudas, Y. J. Lee, R. Graf, H. W. Spiess, and K. Mullen** (2009). Molecularly tethered amphiphiles as 3-d supramolecular assembly platforms: Unlocking a trapped conformation. *Journal of the American Chemical Society*, **131**(24), 8537–8547.
 21. **Clemens, D., P. Gross, P. Keller, N. Schlumpf, and M. Konnecke** (2000). Amor - the versatile reflectometer at sinq. *Physica B*, **276**, 140–141.
 22. **Clements, J. A. and M. E. Avery** (1998). Lung surfactant and neonatal respiratory distress syndrome. *American Journal of Respiratory and Critical Care Medicine*, **157**(4), S59–S66.
 23. **Danov, K. D., G. M. Radulova, P. A. Kralchevsky, K. Golemanov, and S. D. Stoyanov** (2012). Surface shear rheology of hydrophobin adsorption layers: laws of viscoelastic behaviour with applications to long-term foam stability. *Faraday Discussions*, **158**, 195–221.
 24. **de Viguerie, L., R. Keller, U. Jonas, R. Berger, C. G. , C. O. Klein, T. Geue, K. Mullen, H. J. Butt, and D. Vlassopoulos** (2011). Effect of the molecular structure on the hierarchical self-assembly of semifluorinated alkanes at the air/water interface. *Langmuir*, **27**(14), 8776–8786.
 25. **Dewhurst, P. F., M. R. Lovell, J. L. Jones, R. W. Richards, and J. R. P. Webster** (1998). Organization of dispersions of a linear diblock copolymer of polystyrene and poly(ethylene oxide) at the air-water interface. *Macromolecules*, **31**(22), 7851–7864.

26. **Dickinson, E., J. A. Hunt, and D. G. Dalgleish** (1991). Competitive adsorption of phosvitin with milk proteins in oil-in-water emulsions. *Food Hydrocolloids*, **4**(5), 403–414.
27. **Duarte, P., M. Silva, D. Rodrigues, P. Morgado, L. F. G. Martins, and E. J. M. Filipe** (2013). Liquid mixtures involving hydrogenated and fluorinated chains: (p, ρ , t, x) surface of (ethanol plus 2,2,2-trifluoroethanol), experimental and simulation. *Journal of Physical Chemistry B*, **117**(33), 9709–9717.
28. **Eftaiha, A. F. and M. F. Paige** (2012). Phase-separation of mixed surfactant monolayers: A comparison of film morphology at the solid-air and liquid-air interfaces. *Journal of Colloid and Interface Science*, **380**, 105–112.
29. **Elman, J. F., D. H. T. Lee, J. T. Koberstein, and P. M. Thompson** (1995). Time-of-flight secondary-ion mass-spectrometric measurements of molecular-weight distributions for functionally terminated oligomers and transferred langmuir-blodgett-kuhn monolayers. *Langmuir*, **11**(7), 2761–2767.
30. **Erni, P., P. Fischer, E. Windhab, J. Kusnezov, H. Stettin, and J. Lauger** (2003). Stress- and strain-controlled measurements of interfacial shear viscosity and viscoelasticity at liquid/liquid and gas/liquid interfaces. *Rev. Sci. Instrum.*, **74**, 4916–4924.
31. **Erni, P., H. A. Jerri, K. Wong, and A. Parker** (2012). Interfacial viscoelasticity controls buckling, wrinkling and arrest in emulsion drops undergoing mass transfer. *Soft Matter*, **8**(26), 6958–6967.
32. **Erni, P. and A. Parker** (2012). Nonlinear viscoelasticity and shear localization at complex fluid interfaces. *Langmuir*, **28**(20), 7757–7767.
33. **Espinosa, G., I. Lopez-Montero, F. Monroy, and D. Langevin** (2011). Shear rheology of lipid monolayers and insights on membrane fluidity. *Proceedings of the National Academy of Sciences of the United States of America*, **108**(15), 6008–6013.
34. **Evans, S. D., S. R. Johnson, H. Ringsdorf, L. M. Williams, and H. Wolf** (1998). Photoswitching of azobenzene derivatives formed on planar and colloidal gold surfaces. *Langmuir*, **14**(22), 6436–6440.
35. **Ewoldt, R. H., A. E. Hosoi, and G. H. McKinley** (2008). New measures for characterizing nonlinear viscoelasticity in large amplitude oscillatory shear. *Journal of Rheology*, **52**(6), 1427–1458.
36. **Feringa, B. L., W. F. Jager, and B. Delange** (1993). Organic materials for reversible optical-data storage. *Tetrahedron*, **49**(37), 8267–8310.
37. **Feringa, B. L., R. A. van Delden, N. Koumura, and E. M. Geertsema** (2000). Chiroptical molecular switches. *Chemical Reviews*, **100**(5), 1789–1816.
38. **Filipe, S., M. T. Cidade, M. Wilhelm, and J. M. Maia** (2004). Evolution of morphological and rheological properties along the extruder length for blends of a commercial liquid crystalline polymer and polypropylene. *Polymer*, **45**(7), 2367–2380.
39. **Fleury, G., G. Schlatter, and R. Muller** (2004). Non linear rheology for long chain branching characterization, comparison of two methodologies: Fourier transform rheology and relaxation. *Rheologica Acta*, **44**(2), 174–187.

40. **Fox, H. W., P. W. Taylor, and W. A. Zisman** (1947). Polyorganosiloxanes surface active properties. *Industrial and Engineering Chemistry*, **39**(11), 1401–1409.
41. **Gaines, G. L.** (1966). Insoluble monolayers at liquid-gas interfaces. *John Wiley and Sons, Inc.*
42. **Gaines, G. L.** (1991). Surface-activity of semifluorinated alkanes - $f(cf_2)_m(ch_2)_nH$. *Langmuir*, **7**(12), 3054–3056.
43. **Gamboa, A. L. S., E. J. M. Filipe, and P. Brogueira** (2002). Nanoscale pattern formation in langmuir-blodgett films of a semifluorinated alkane and a polystyrene-poly(ethylene oxide) diblock copolymer. *Nano Letters*, **2**(10), 1083–1086.
44. **Garrett, W. D. and W. A. Zisman** (1970). Damping of capillary waves on water by monomolecular films of linear polyorganosiloxanes. *Journal of Physical Chemistry*, **74**(8), 1796.
45. **Gavranovic, G. T., J. M. Deutsch, and G. G. Fuller** (2005). Two-dimensional melts: Polymer chains at the air-water interface. *Macromolecules*, **38**(15), 6672–6679.
46. **Georgieva, D., A. Cagna, and D. Langevin** (2009). Link between surface elasticity and foam stability. *Soft Matter*, **5**(10), 2063–2071.
47. **Giacomin, A. J., R. S. Jeyaseelan, T. Samurkas, and J. M. Dealy** (1993). Validity of separable bkz model for large-amplitude oscillatory shear. *Journal of Rheology*, **37**(5), 811–826.
48. **Giacomin, A. J. and J. G. Oakley** (1992). Structural network models for molten plastics evaluated in large-amplitude oscillatory shear. *Journal of Rheology*, **36**(8), 1529–1546.
49. **Glagola, C. P., L. M. Miceli, M. A. Milchak, E. H. Halle, and J. L. Logan** (2012). Polystyrene-poly(ethylene oxide) diblock copolymer: The effect of polystyrene and spreading concentration at the air/water interface. *Langmuir*, **28**(11), 5048–5058.
50. **Goedel, W. A., C. Peyratout, L. Ouali, and V. Schadler** (1999). Vittrification of monolayers of a polymer brush. *Advanced Materials*, **11**(3), 213–216.
51. **Goedel, W. A., C. B. Xu, and C. W. Frank** (1993). Perfluoropolyethers tethered to the air-water-interface. *Langmuir*, **9**(5), 1184–1186.
52. **Gottwald, A., D. Pospiech, D. Jehnichen, L. Haussler, P. Friedel, J. Pionteck, M. Stamm, and G. Floudas** (2002). Self-assembly and viscoelastic properties of semi-fluorinated polyesters. *Macromolecular Chemistry and Physics*, **203**(5-6), 854–861.
53. **Grimard, R., P. Tancrede, and C. Gicquaud** (1993). Interaction of actin with positively charged phospholipids - a monolayer study. *Biochemical and Biophysical Research Communications*, **190**(3), 1017–1022.
54. **Gupta, M., T. Gutberlet, J. Stahn, P. Keller, and D. Clemens** (2004). Amor - the time-of-flight neutron reflectometer at sinq/psi. *Pramana-Journal of Physics*, **63**(1), 57–63.

55. **Hahn, T. D., S. L. Hsu, and H. D. Stidham** (1997). Reflectance infrared spectroscopic analysis of polymers at the air-water interface .4. microstructure of poly(dimethylsiloxane). *Macromolecules*, **30**(1), 87–92.
56. **Hard, S. and R. D. Neuman** (1987). Viscoelasticity of monomolecular films - a laser light-scattering study. *Journal of Colloid and Interface Science*, **120**(1), 15–29.
57. **Harris, J.** (1965). Response of time dependent materials to oscillatory motion. *Nature*, **207**(4998), 744.
58. **Hermans, E. and J. Vermant** (2014). Interfacial shear rheology of dppc under physiologically relevant conditions. *Soft Matter*, **10**(1), 175–186.
59. **Hilles, H., F. Monroy, L. J. Bonales, F. Ortega, and R. G. Rubio** (2006). Fourier-transform rheology of polymer langmuir monolayers: Analysis of the non-linear and plastic behaviors. *Advances in Colloid and Interface Science*, **122**(1-3), 67–77.
60. **Hodges, C. S., R. B. Hammond, and D. Gidalevitz** (2008). Behavior of thin films of poly(oxyethylene)-poly(oxybutylene) copolymers studied by brewster angle microscopy and atomic force microscopy. *Langmuir*, **24**(23), 13470–13476.
61. **Hodges, C. S., F. Neville, O. Konovalov, R. B. Hammond, D. Gidalevitz, and I. W. Hamley** (2006). Structural analysis of peo-pbo copolymer monolayers at the air-water interface. *Langmuir*, **22**(21), 8821–8825.
62. **Hsu, W. P., Y. L. Lee, and S. H. Liou** (2006). Monolayer characteristics of stereoregular pmma at the air/water interface. *Applied Surface Science*, **252**(12), 4312–4320.
63. **Hyun, K., M. Wilhelm, C. O. , K. S. Cho, J. G. Nam, K. H. Ahn, S. J. Lee, R. H. Ewoldt, and G. H. McKinley** (2011). A review of nonlinear oscillatory shear tests: Analysis and application of large amplitude oscillatory shear (laos). *Progress in Polymer Science*, **36**(12), 1697–1753.
64. **Ikeda, T., O. Tsutsumi, and Y. L. Wu** (2000). Optical switching and image storage by means of photochromic liquid crystals. *Molecular Crystals and Liquid Crystals*, **347**, 245–257.
65. **Jaishankar, A., V. Sharma, and G. H. McKinley** (2011). Interfacial viscoelasticity, yielding and creep ringing of globular protein-surfactant mixtures. *Soft Matter*, **7**(17), 7623–7634.
66. **Jasiuk, I., J. Chen, and M. F. Thorpe** (1994). Elastic moduli of two dimensional materials with polygonal and elliptical holes. *Applied Mechanics Reviews*, **47**, S18–S28.
67. **Johner, A. and J. F. Joanny** (1990). Block copolymer adsorption in a selective solvent - a kinetic-study. *Macromolecules*, **23**(26), 5299–5311.
68. **Kaganer, V., M. H., and D. P.** (1999). Structure and phase transitions in langmuir monolayers. *Reviews of Modern Physics*, **71**, 779–819.
69. **Kawaguchi, M., S. Komatsu, M. Matsuzumi, and A. Takahashi** (1984). Concentration-dependence of surface pressure of polyether monolayers at the air water interface. *Journal of Colloid and Interface Science*, **102**(2), 356–360.

70. **Kent, M. S., L. T. Lee, B. Farnoux, and F. Rondelez** (1992). Characterization of diblock copolymer monolayers at the liquid air interface by neutron reflectivity and surface-tension measurements. *Macromolecules*, **25**(23), 6240–6247.
71. **Kim, C., M. C. Gurau, P. S. Cremer, and H. Yu** (2008). Chain conformation of poly(dimethyl siloxane) at the air/water interface by sum frequency generation. *Langmuir*, **24**(18), 10155–10160.
72. **Kissa, E.** (New York, 2001). Fluorinated surfactants and repellents. *Surfactant science*, **97**, Second edition.
73. **Klein, C., P. Venema, L. Sagis, and E. van der Linden** (2008). Rheological discrimination and characterization of carrageenans and starches by fourier transform-rheology in the non-linear viscous regime. *Journal of Non-Newtonian Fluid Mechanics*, **151**(1-3), 145–150.
74. **Klein, C. O., L. de Viguerie, C. Christopoulou, U. Jonas, C. G. , K. Mullen, and D. Vlassopoulos** (2011). Viscoelasticity of semifluorinated alkanes at the air/water interface. *Soft Matter*, **7**(17), 7737–7746.
75. **Klein, C. O., H. W. Spiess, A. Calin, C. Balan, and M. Wilhelm** (2007). Separation of the nonlinear oscillatory response into a superposition of linear, strain hardening, strain softening, and wall slip response. *Macromolecules*, **40**(12), 4250–4259.
76. **Kocer, A., M. Walko, W. Meijberg, and B. L. Feringa** (2005). A light-actuated nanovalve derived from a channel protein. *Science*, **309**(5735), 755–758.
77. **Krafft, M. P.** (2001). Fluorocarbons and fluorinated amphiphiles in drug delivery and biomedical research. *Adv. Drug. Deliv. Rev.*, **47**, 209–228.
78. **Krafft, M. P.** (2012a). Large organized surface domains self-assembled from nonpolar amphiphiles. *Accounts of Chemical Research*, **45**(4), 514–524.
79. **Krafft, M. P.** (2012b). Strasbourg's sofft team-soft functional systems self-assembled from perfluoroalkylated molecular components. *Journal of Fluorine Chemistry*, **134**, 90–102.
80. **Krafft, M. P. and J. G. Riess** (2009). Chemistry, physical chemistry, and uses of molecular fluorocarbon-hydrocarbon diblocks, triblocks, and related compounds-unique "ap-blar" components for self-assembled colloid and interface engineering. *Chemical Reviews*, **109**(5), 1714–1792.
81. **Kralchevsky, P. A. and K. Nagayama** (1994). Capillary forces between colloidal particles. *Langmuir*, **10**(1), 23–36.
82. **Krishnaswamy, R., S. Majumdar, and A. K. Sood** (2007). Nonlinear viscoelasticity of sorbitan tristearate monolayers at liquid gas interface. *Langmuir*, **23**(26), 12951–12958.
83. **Kumaki, J.** (1986). Polystyrene monomolecular particles obtained by spreading dilute-solutions on the water-surface. *Macromolecules*, **19**(8), 2258–2263.
84. **Kumaki, J.** (1988). Monolayer of polystyrene monomolecular particles on a water-surface studied by langmuir-type film balance and transmission electron-microscopy. *Macromolecules*, **21**(3), 749–755.

85. **Kumar, B. and K. A. Suresh** (2009). Kinetics of trans-cis isomerization in azobenzene dimers at an air-water interface. *Physical Review E*, **80**(2).
86. **Kumar, G. S. and D. C. Neckers** (1989). Photochemistry of azobenzene-containing polymers. *Chemical Reviews*, **89**(8), 1915–1925.
87. **Langmuir, I.** (1917). The constitution and fundamental properties of solids and liquids .ll. liquids. *Journal of the American Chemical Society*, **39**, 1848–1906.
88. **Langmuir, I.** (1920). The mechanism of the surface phenomena of flotation. *Trans. Faraday Soc.*, **15**, 62–74.
89. **Laufer, L.** (2013). *Amphiphilic Block Copolymers at Oil-Water Interface*. Ph.D. thesis, Senate of Ben-Gurion University of the Negev, Israel.
90. **Lee, L. T., E. K. Mann, D. Langevin, and B. Farnoux** (1991). Neutron reflectivity and ellipsometry studies of a polymer molecular layer spread on the water-surface. *Langmuir*, **7**(12), 3076–3080.
91. **Lee, Y. J., C. G. Clark, R. Graf, M. Wagner, K. Mullen, and H. W. Spiess** (2009). Solid-state organization of semifluorinated alkanes probed by f-19 mas nmr spectroscopy. *J Phys Chem B*, **113**, 1360–1366.
92. **Lenk, T. J., D. H. T. Lee, and J. T. Koberstein** (1994). End group effects on monolayers of functionally-terminated poly(dimethylsiloxanes) at the air-water-interface. *Langmuir*, **10**(6), 1857–1864.
93. **Ligoure, C. and L. Leibler** (1990). Thermodynamics and kinetics of grafting end-functionalized polymers to an interface. *Journal De Physique*, **51**(12), 1313–1328.
94. **Liu, Z. F., K. Hashimoto, and A. Fujishima** (1990). Photoelectrochemical information-storage using an azobenzene derivative. *Nature*, **347**(6294), 658–660.
95. **Liu, Z. F., K. Morigaki, T. Enomoto, K. Hashimoto, and A. Fujishima** (1992). Kinetic-studies on the thermal cis trans isomerization of an azo compound in the assembled monolayer film. *Journal of Physical Chemistry*, **96**(4), 1875–1880.
96. **Lux, C. D., B. Donnio, B. Heinrich, and M. P. Krafft** (2013). Thermal behavior and high- and low-temperature phase structures of gemini fluorocarbon/hydrocarbon diblocks. *Langmuir*, **29**(17), 5325–5336.
97. **Maaloum, M., P. Muller, and M. P. Krafft** (2002). Monodisperse surface micelles of nonpolar amphiphiles in langmuir monolayers. *Angewandte Chemie-International Edition*, **41**(22), 4331–4334.
98. **Maestro, A., F. Ortega, F. Monroy, J. Kraegel, and R. Miller** (2009). Molecular weight dependence of the shear rheology of poly (methyl methacrylate) langmuir films: A comparison between two different rheometry techniques. *Langmuir*, **25**(13), 7393–7400.
99. **Mann, E. K. and D. Langevin** (1991). Poly(dimethylsiloxane) molecular layers at the surface of water and of aqueous surfactant solutions. *Langmuir*, **7**(6), 1112–1117.

100. **Matsumoto, T., Y. Segawa, Y. Warashina, and S. Onogi** (1973). Nonlinear behavior of viscoelastic materials. ii: The method of analysis and temperature dependence of nonlinear viscoelastic functions. *Trans Soc Rheol*, **17**, 47–62.
101. **Meinert, H. and A. Knoblich** (1993). The use of semifluorinated alkanes in blood substitutes. *Biomater. Artif. Cells Immobil. Biotechnol.*, **21**, 583–595.
102. **Miller, R., J. K. Ferri, A. Javadi, J. Kragel, N. Mucic, and R. Wustneck** (2010). Rheology of interfacial layers. *Colloid and Polymer Science*, **288**(9), 937–950.
103. **Miller, R., Z. Policova, R. Sedev, and A. W. Neumann** (1993). Relaxation behavior of human albumin adsorbed at the solution air interface. *Colloids and Surfaces a-Physicochemical and Engineering Aspects*, **76**, 179–185.
104. **Mita, I., K. Horie, and K. Hirao** (1989). Photochemistry in polymer solids .9. photoisomerization of azobenzene in a polycarbonate film. *Macromolecules*, **22**(2), 558–563.
105. **Morgado, P., J. Ben Lewis, C. M. C. Laginhas, L. F. G. Martins, C. McCabe, F. J. Blas, and E. J. M. Filipe** (2011a). Systems involving hydrogenated and fluorinated chains: Volumetric properties of perfluoroalkanes and perfluoroalkylalkane surfactants. *Journal of Physical Chemistry B*, **115**(50), 15013–15023.
106. **Morgado, P., C. M. C. Laginhas, J. Ben Lewis, C. McCabe, L. F. G. Martins, and E. J. M. Filipe** (2011b). Viscosity of liquid perfluoroalkanes and perfluoroalkylalkane surfactants. *Journal of Physical Chemistry B*, **115**(29), 9130–9139.
107. **Morgado, P., R. Tomas, H. Zhao, A. C. dos Ramos, F. J. Blas, C. McCabe, and E. J. M. Filipe** (2007a). Solution behavior of perfluoroalkanes and perfluoroalkylalkane surfactants in n-octane. *Journal of Physical Chemistry C*, **111**(43), 15962–15968.
108. **Morgado, P., H. G. Zhao, F. J. Blas, C. McCabe, L. P. N. Rebelo, and E. J. M. Filipe** (2007b). Liquid phase behavior of perfluoroalkylalkane surfactants. *Journal of Physical Chemistry B*, **111**(11), 2856–2863.
109. **Muzikante, I., L. Gerca, E. Fonavs, M. Rutkis, D. Gustina, E. Markava, B. Stiller, L. Brehmer, and G. Knochenhauer** (2002). Self-assembled monolayers of azobenzene functionalized 1,3,5-triazine-4,6-dithiols. *Materials Science and Engineering C-Biomimetic and Supramolecular Systems*, **22**(2), 339–343.
110. **Neidhofer, T., S. Sioula, N. Hadjichristidis, and M. Wilhelm** (2004). Distinguishing linear from star-branched polystyrene solutions with fourier-transform rheology. *Macromolecular Rapid Communications*, **25**(22), 1921–1926.
111. **Neidhofer, T., M. Wilhelm, and B. Debbaut** (2003). Fourier-transform rheology experiments and finite-element simulations on linear polystyrene solutions. *Journal of Rheology*, **47**(6), 1351–1371.
112. **Noll, W., Steinbac.H, and C. Sucker** (1971). Monolayers of polyorganosiloxanes on water. *Journal of Polymer Science Part C-Polymer Symposium*, (34), 123–139.
113. **Nunez, E., C. G. Clark, W. Cheng, A. Best, G. Floudas, A. N. Semenov, G. Fytas, and K. Mullen** (2008). Thermodynamic, structural, and nanomechanical properties of a fluorous biphasic material. *Journal of Physical Chemistry B*, **112**(21), 6542–6549.

114. **Onogi, S. M. T. and T. Matsumoto** (1970). Nonlinear behavior of viscoelastic materials. i: Disperse systems of polystyrene solution and carbon black. *Trans Soc Rheol*, **14**, 275–294.
115. **Parratt, L. G.** (1954). Surface studies of solids by total reflection of x-rays. *Physical Review*, **95**(2), 359–369.
116. **Payne, A.** (1962). The dynamic properties of carbon black-loaded natural rubber vulcanizates. *Part I. J. Appl. Polym. Sci.*, **6**, 57–63.
117. **Penfold, J., R. K. Thomas, E. Simister, E. Lee, and A. Rennie** (1990). The structure of mixed surfactant monolayers at the air-liquid interface, as studied by specular neutron reflection. *Journal of Physics-Condensed Matter*, **2**, SA411–SA416.
118. **Philippoff, W.** (1966). Vibrational measurements with large amplitudes. *Trans Soc Rheol*, **10**, 317–334.
119. **Rabolt, J., T. P. Russell, and R. J. Twieg** (1984). Structural studies of semifluorinated n-alkanes. 1. synthesis and characterization of $\text{f}(\text{cf}_2)_n(\text{ch}_2)_m\text{h}$ in the solid state. *Macromolecules*, **17**, 2786–2794.
120. **Richards, R. W., B. R. Rochford, and J. R. P. Webster** (1994). Organization of an amphiphilic linear diblock copolymer at the air/water interface studied by neutron reflectometry. *Faraday Discussions*, **98**, 263–281.
121. **Riess, J. G.** (2002). Fluorous micro-and nanophases with a biomedical perspective. *Tetrahedron*, **58**, 4113–4131.
122. **Riess, J. G.** (2009). Highly fluorinated amphiphilic molecules and self-assemblies with biomedical potential. *Current Opinion in Colloid and Interface Science*, **14**(5), 294–304.
123. **Schlatter, G., G. Fleury, and R. Muller** (2005). Fourier transform rheology of branched polyethylene: Experiments and models for assessing the macromolecular architecture. *Macromolecules*, **38**(15), 6492–6503.
124. **Schwarzl, F. R.** (1969). The numerical calculation of storage and loss compliance from creep data for linear viscoelastic materials. *Rheol Acta*, **8**(1), 6–17.
125. **Seki, T., M. Sakuragi, Y. Kawanishi, Y. Suzuki, T. Tamaki, R. Fukuda, and K. Ichimura** (1993). Command surfaces of langmuir-blodgett-films - photoregulations of liquid-crystal alignment by molecularly tailored surface azobenzene layers. *Langmuir*, **9**(1), 211–218.
126. **Semenov, A. N., A. Gonzalez-Perez, M. P. Krafft, and J. F. Legrand** (2006). Theory of surface micelles of semifluorinated alkanes. *Langmuir*, **22**(21), 8703–8717.
127. **Shang, T. G., K. A. Smith, and T. A. Hatton** (2003). Photoresponsive surfactants exhibiting unusually large, reversible surface tension changes under varying illumination conditions. *Langmuir*, **19**(26), 10764–10773.
128. **Shuler, R. L. and W. A. Zisman** (1970). A study of behavior of polyoxyethylene at air-water interface by wave damping and other methods. *Journal of Physical Chemistry*, **74**(7), 1523–1534.

129. **Srivastava, S., D. Leiske, J. K. Basu, and G. G. Fuller** (2011). Interfacial shear rheology of highly confined glassy polymers. *Soft Matter*, **7**(5), 1994–2000.
130. **Stangenberg, R.** (2013). *Oberflächenstrukturierte amphiphile Polyphenylendendrimere zur Imitation natürlicher Transportproteine*. Ph.D. thesis, Promotionsgebiet Makromolekulare Chemie am Fachbereich Chemie, Pharmazie und Geowissenschaften der Johannes Gutenberg-Universität Mainz, Germany.
131. **Stangenberg, R., C. Grigoriadis, J. Butt, H. K. Mullen, and G. Floudas** (2014). Switchable dielectric permittivity with temperature and dc-bias in a semifluorinated azobenzene derivative. *Colloid Polym. Sci.*, **292**, 1939–1948.
132. **Stangenberg, R., C. Grigoriadis, D. Schneider, H. J. Butt, G. Fytas, K. Mullen, and G. Floudas** (2013). Self-assembly beyond semifluorinated alkanes in a semifluorinated benzene derivative. *Soft Matter*, **9**(47), 11334–11345.
133. **Stocco, A., K. Tauer, S. Pispas, and R. Sigel** (2011). Dynamics of amphiphilic diblock copolymers at the air-water interface. *Journal of Colloid and Interface Science*, **355**(1), 172–178.
134. **Sugimoto, M., Y. Suzuki, K. Hyun, K. H. Ahn, T. Ushioda, A. Nishioka, T. Taniguchi, and K. Koyama** (2006). Melt rheology of long-chain-branched polypropylenes. *Rheologica Acta*, **46**(1), 33–44.
135. **Swalen, J. D., D. L. Allara, J. D. Andrade, E. A. Chandross, S. Garoff, J. Israelachvili, T. J. McCarthy, R. Murray, R. F. Pease, and et al.** (1987). Molecular monolayers and films. a panel report for the materials sciences division of the department of energy. *Langmuir*, **3**(6), 932–950.
136. **Tee, T. and J. Dealy** (1975). Nonlinear viscoelasticity of polymer melts. *J Rheol*, **19**, 595–615.
137. **Torcello-Gomez, A., J. Maldonado-Valderrama, M. J. Galvez-Ruiz, A. Martin-Rodriguez, M. A. Cabrerizo-Vilchez, and J. de Vicente** (2011). Surface rheology of sorbitan tristearate and beta-lactoglobulin: Shear and dilatational behavior. *Journal of Non-Newtonian Fluid Mechanics*, **166**(12-13), 713–722.
138. **Tretiakov, K. V. and K. W. Wojciechowski** (2007). Poisson’s ratio of simple planar ‘isotropic’ solids in two dimensions. *physica status solidi*, **244**(3), 1038–1046.
139. **van Dusschoten, D. and M. Wilhelm** (2001). Increased torque transducer sensitivity via oversampling. *Rheologica Acta*, **40**(4), 395–399.
140. **Vandebril, S., A. Franck, G. G. Fuller, P. Moldenaers, and J. Vermant** (2010). A double wall-ring geometry for interfacial shear rheometry. *Rheologica Acta*, **49**(2), 131–144.
141. **Velema, W. A., W. Szymanski, and B. L. Feringa** (2014). Photopharmacology: Beyond proof of principle. *Journal of the American Chemical Society*, **136**(6), 2178–2191.
142. **Verwijlen, T., P. Moldenaers, H. Stone, and J. Vermant** (2011). Study of the flow field in the magnetic rod interfacial stress rheometer. *Langmuir*, **27**, 945.

143. **Vogel, N., L. de Viguerie, U. Jonas, C. K. Weiss, and K. Landfester** (2011). Wafer-scale fabrication of ordered binary colloidal monolayers with adjustable stoichiometries. *Advanced Functional Materials*, **21**(16), 3064–3073.
144. **Wilhelm, M., D. Maring, and H. W. Spiess** (1998). Fourier-transform rheology. *Rheologica Acta*, **37**(4), 399–405.
145. **Wilhelm, M., P. Reinheimer, and M. Ortseifer** (1999). High sensitivity fourier-transform rheology. *Rheologica Acta*, **38**(4), 349–356.
146. **Wilhelm, M., P. Reinheimer, M. Ortseifer, T. Neidhofer, and H. W. Spiess** (2000). The crossover between linear and non-linear mechanical behaviour in polymer solutions as detected by fourier-transform rheology. *Rheologica Acta*, **39**(3), 241–246.
147. **Wittmer, J., A. Johner, J. F. Joanny, and K. Binder** (1994). Chain desorption from a semidilute polymer brush - a monte-carlo simulation. *Journal of Chemical Physics*, **101**(5), 4379–4390.
148. **Wulff-Perez, M., A. Torcello-Gomez, A. Martin-Rodriguez, M. J. Galvez-Ruiz, and J. de Vicente** (2011). Bulk and interfacial viscoelasticity in concentrated emulsions: The role of the surfactant. *Food Hydrocolloids*, **25**(4), 677–686.
149. **Wustneck, R., V. B. Fainerman, and V. Zauls** (1999). Characterization and modeling of cis-trans photoisomerization of a trifluoromethoxy-substituted metacrylate copolymer monolayer at a fluid interface. *Journal of Physical Chemistry B*, **103**(18), 3587–3592.
150. **www.ncnr.nist.gov** (). <http://www.ncnr.nist.gov/resources/sldcalc.html>, national institute of standards and technology center for neutron research. scattering length density calculator;.
151. **Xie, S., A. Natansohn, and P. Rochon** (1993). Recent developments in aromatic azo polymers research. *Chemistry of Materials*, **5**(4), 403–411.
152. **Yaroshchuk, O. V., A. D. Kiselev, Y. Zakrevskyy, T. Bidna, L. C. Kelly, J. and Chien, and J. Lindau** (2003). Photoinduced three-dimensional orientational order in side chain liquid crystalline azopolymers. *Physical Review E*, **68**(1).
153. **Yim, K. S. and G. G. Fuller** (2003). Influence of phase transition and photoisomerization on interfacial rheology. *Physical Review E*, **67**(4).
154. **Zajac, R. and A. Chakrabarti** (1994). Kinetics and thermodynamics of end-functionalized polymer adsorption and desorption processes. *Physical Review E*, **49**(4), 3069–3078.
155. **Zasadzinski, J. A., J. Ding, H. E. Warriner, F. Bringezu, and A. J. Waring** (2001). The physics and physiology of lung surfactants. *Current Opinion in Colloid and Interface Science*, **6**(5-6), 506–513.
156. **Zhang, G. F., P. Marie, M. Maalourn, P. Muller, N. Benoit, and M. P. Krafft** (2005). Occurrence, shape, and dimensions of large surface hemimicelles made of semifluorinated alkanes. elongated versus circular hemimicelles. pit- and tip-centered hemimicelles. *Journal of the American Chemical Society*, **127**(29), 10412–10419.
157. **Zhang, J. and X. Li** (2012). Stimuli-triggered structural engineering of synthetic and biological polymeric assemblies. *Progress in Polymer Science*, **37**(8), 1130–1176.

LIST OF PAPERS BASED ON THESIS

1. A. Theodoratou, U. Jonas, B. Loppinet, T. Geue, R. Stangenberg, D. Vlassopoulos, Photoswitching the Mechanical Properties in Langmuir Layers of Semi-fluorinated Alkyl-Azobenzenes at the Air-Water Interface. *Physical Chemistry Chemical Physics* (In press).
2. A. Theodoratou, U. Jonas, B. Loppinet, T. Geue, R. Stangenberg, R. Keller, D. Li, C. Clark, R. Berger, K. Müllen, HJ. Butt, J. Vermant, D. Vlassopoulos, Semi-fluorinated Alkanes at the Air-Water Interface: effects of molecular architecture on structure and rheology. *Langmuir* (submitted).
3. C. Klein, A. Theodoratou, L. De Viguerie, M. Retsch, U. Jonas, B. Loppinet, M. Wilhelm, D. Vlassopoulos, Interfacial Fourier Transform Rheology of Complex Fluid Interfaces using the magnetic rod stress rheometer. *Soft matter* (in preparation).